UNIVERSIDADE DE LISBOA
FACULDADE DE CIÊNCIAS
DEPARTAMENTO DE FÍSICA

Integration of Multi-shell Diffusion Imaging derived Metrics in Tractography Reconstructions of Clinical Data

Joana Rita Simões Guido

Mestrado Integrado em Engenharia Biomédica e Biofísica
Perfil em Engenharia Clínica e Instrumentação Médica

Dissertação orientada por:
Prof. Dr. Christopher Clark
Prof. Dr. Alexandre Andrade

2019

“Travel isn't always pretty. It isn't always comfortable.
Sometimes it hurts, it even breaks your heart. But that's okay.
The journey changes you; it should change you.
It leaves marks on your memory, on your consciousness,
on your heart, and on your body. You take something with you.
Hopefully, you leave something good behind.”

Anthony Bourdain

Acknowledgements

First of all, I have to refer that I am extremely grateful to have been on Institute of Child Health (University College London) with amazing people from whom I learned so much.

Thank you first to Professor Chris Clark for hosting me in this project in the Developmental Imaging & Biophysics Section (DIBS) and for all his attention, concern and support. It was a privilege to work here.

I am also very thankful to Dr Luis Lacerda for giving me the opportunity to work with him. I am grateful for all the advice, patience, time and energy that he focused on my work. I am thankful for the excellent example he is, his enthusiasm was contagious and very motivational for me. I will never forget this experience.

I also would like to express my thanks to the staff of DIBS for providing me with the conditions to learn more and for all their sympathy and encouragement during my stay. A special thanks to Dr Fábio Nery, Dr Sara Lorio, Dr Sonja Soskic, Miss Ramneek Kaur Jouhal and Mr Leevi Kerkelä for all your support and interesting discussions. I also have to say that I am extremely thankful to Dr Donald Tournier from Department of Perinatal Imaging and Health (King's College London) for the help provided during this work, for all the suggestions and tips.

I would like to express my deepest gratitude to Professor Alexandre Andrade. As my supervisor, his regular and prompt feedback, support and optimism were crucial in this work. I hope to sustain his example in my future pursuits.

As well, I would like to thank to Professor Hugo Ferreira, as the coordinator of the Masters in Biophysics and Biomedical Engineering, and to all Professors of the Institute of Biophysics and Biomedical Engineering (Faculty of Sciences, University of Lisbon) for all the time, sympathy, encouragement and knowledge during the last five years.

The funding received from the Erasmus Programme was essential for this project. For that, I would like to thank to University of Lisbon for the funding.

To my friends, for all the support, and encouragement words when I most needed them. A special thank you to my two colleagues and friends Mariana Silva and Inês Domingos for sharing this amazing opportunity with me and for making this experience an unforgettable one. And of course, thank you Rita Silva, Sara Costa, Rita Tomás, Sara Guerreiro and Inês Bagulho. Without you these last years would have passed by, but it would not have been the same. It was a pleasure to have shared five years of my life learning alongside all of you.

Last, but definitely not least, my parents José and Cristina and my brother João. A big and warm thank you to them who provided me this great experience, being always by my side. Thank you for the support, patience, affection, attention and for all that you did. Without you, all of this would not be possible. I hope I have the opportunity to always be there as you have for me.

Abstract

Diffusion-weighted magnetic resonance imaging (dMRI) is a non-invasive imaging method which has been successfully applied to study white matter (WM) in order to determine physiological information and infer tissue microstructure. The human body is filled with barriers affecting the mobility of molecules and preventing it from being constant in different directions (anisotropic diffusion). In the brain, the sources for this anisotropy arise from dense packing axons and from the myelin sheath that surrounds them. Diffusion Tensor Imaging (DTI) is widely used to extract fibre directions from diffusion data, but it fails in regions containing multiple fibre orientations. The constrained spherical deconvolution technique had been proposed to address this limitation. It provides an estimate of the fibre orientation distribution that is robust to noise whilst preserving angular resolution. As a non-invasive technique that generates a three-dimensional reconstruction of neuronal fibres, tractography is able to map *in vivo* the human WM based on the reconstruct of the fibre orientations from the diffusion profile. Most of the tractography studies use a "tract-averaged" approach to analysis, however it is well known that there is a prominent variation in diffusion metrics within WM tracts. In this study we address the challenge of defining a microstructural signature taking into account the potentially rich anatomical variation in diffusion metrics along the tracts. Therefore, a workflow to conduct along-tract analysis of WM tracts (namely, arcuate fasciculus, corticospinal and corpus callosum) and integrate not only DTI derived measures, but also more advanced parameters from Mean Apparent Propagator-Magnetic Resonance Imaging (MAP-MRI) and Neurite Orientation Dispersion and Density Imaging (NODDI) model, was developed across healthy controls and patients with Temporal Lobe Epilepsy (TLE). Beyond the true biological variation in diffusion properties along tracts, this technique was applied to show that it allows a more detailed analysis of small regions-of-interest extracted from the tract in order to avoid fibres from WM pathways in the neighbourhood, which might lead to equivocal biological interpretations of the microstructural parameters. Consequently, the along-tract streamline distribution from the centrum semiovale, which is known to be a complex fibre geometry with multiple fibres populations from arcuate fasciculus, corticospinal and corpus callosum, was investigated. Finally, to validate our approach and highlight the strength of this extensible framework, two other methods were implemented in order to support the conclusions derived from the along-tract analysis computed between-groups. Firstly, a tract-based spatial statistics (TBSS) analysis was performed to study the WM change patterns across the whole brain in patients with TLE, and explore the alteration of multiple diffusion metrics. This voxel-based technique provides a powerful and objective method to perform multi-subject comparison, based on voxel-wise statistics of diffusion metrics but simultaneous aiming to minimize the effects of misalignment using a conventional voxel-based analysis method. With this in mind, the results showed increased diffusivity and reduced diffusion anisotropy, suggesting a loss of structural organization and expansion of the extracellular space in the presence of neuropathological condition as TLE. Secondly, the fixel-based analysis (FBA) was performed allowing a comprehensive statistical analysis of WM quantitative measures in order to have access to changes that may result within WM tracts in the presence of TLE. The microstructural/macrostructural changes in WM tracts of TLE patients were observed in temporal and extratemporal regions of both hemispheres, which agrees with the concept that epilepsy is a network disorder.

Keywords: Diffusion-weighted magnetic resonance imaging (dMRI); Tractography; Along-Tract Analysis; Tract-Based Spatial Statistics (TBSS); Fixel-Based Analysis (FBA).

Resumo

Nos últimos anos, com o rápido avanço das técnicas imagiológicas, a oportunidade de mapear o cérebro humano *in vivo* com uma resolução sem precedentes tornou-se realidade, permanecendo ainda hoje como uma das áreas de maior interesse da neurociência.

Sabendo que o movimento natural das moléculas de água nos tecidos biológicos é altamente influenciado pelo ambiente microestrutural envolvente, e que a anisotropia que este processo aleatório assume na matéria branca pode ser explorada com o intuito de inferir características importantes associadas ao tecido neuronal, a ressonância magnética ponderada por difusão (dMRI, do inglês "Diffusion-Weighted Magnetic Resonance Imaging") afirmou-se como a técnica de imagem mais amplamente utilizada para a investigação *in vivo* e não invasiva da conectividade cerebral.

A primeira técnica padrão de dMRI foi a imagiologia por tensor de difusão (DTI, do inglês "Diffusion Tensor Imaging"). Implementada com a capacidade de fornecer sensibilidade à microestrutura do tecido, esta técnica permite extrair informação acerca da tridimensionalidade da distribuição da difusão de moléculas de água através da aplicação de seis gradientes de difusão não colineares entre si. Além da difusividade média (MD, do inglês "Mean Diffusivity"), é também possível extrair outros índices microestruturais, como a anisotropia fraccional (FA, do inglês "Fractional Anisotropy"), que fornece informação acerca da percentagem de difusão anisotrópica num determinado voxel. Ambas as métricas são amplamente utilizadas como medidas de alterações microestruturais, todavia, apesar da sua sensibilidade, estes marcadores não são específicos quanto às características individuais da microestrutura tecidual. Regiões com reduzida FA podem camuflar regiões de conformação de cruzamento de fibras, ou fibras muito anguladas, que a DTI não consegue resolver. A razão para esta limitação reside no número reduzido de diferentes direções de difusão que são exploradas, assim como no pressuposto de que a distribuição das moléculas de água é gaussiana, o que não é necessariamente verdade.

De forma alternativa e com o intuito de tais limitações serem ultrapassadas, é possível implementar uma representação matemática do sinal adquirido de forma a explorar o propagador de difusão, da qual a imagiologia por ressonância magnética do propagador aparente médio (MAP-MRI, do inglês “Mean Apparent Propagator Magnetic Resonance Imaging”) é exemplo. Esta técnica analítica caracteriza-se pelo cálculo da função de densidade de probabilidade associada ao deslocamento de spin, o que permite descrever o caráter não-gaussiano do processo de difusão tridimensional e quantificar índices escalares inerentes ao processo de difusão, os quais sublinham as características complexas intrínsecas à microestrutura do tecido. Estes parâmetros incluem o deslocamento médio quadrático (MSD, em inglês “mean square displacement”), a probabilidade de retorno à origem (RTOP, do inglês “return-to-the origin probability”) e suas variantes de difusão em uma e duas dimensões - a probabilidade de retorno ao plano (RTPP, do inglês “return-to-the plane probability”) e a probabilidade de retorno ao eixo (RTAP, do inglês “return-to-the axis probability”), respetivamente.

Em resposta às limitações da DTI associadas à falta de especificidade para distinguir características microestruturais dos tecidos, surgiu ainda o modelo de Dispersão de Orientação de Neurite e Imagem de Densidade (NODDI, do inglês “Neurite Orientation Dispersion and Density Imaging”), o qual utiliza o processo de difusão para estimar a morfologia das neurites. Tendo como premissa subjacente que o sinal de difusão pode ser definido pela soma da contribuição dos sinais de diferentes compartimentos, este modelo biofísico diferencia o espaço intra- e extracelular o que, por sua vez, permite quantificar a dispersão e densidade das neurites. Deste modo, dois parâmetros intrínsecos à microestrutura envolvente podem ser calculados: a densidade neurítica e o índice de dispersão da orientação das neurites. No entanto, de forma a garantir a viabilidade clínica do modelo, este pode ser aplicado por meio do método AMICO (do inglês “Accelerated Microstructure Imaging via Convex

Optimization") através do seu ajuste linear, o que permite o cálculo do índice de dispersão da orientação das neurites (ODI, do inglês "Orientation Dispersion Index"), da fração de volume intracelular (ICVF do inglês, "Intracellular Volume Fraction"), e da fração de volume isotrópico (ISOVF, do inglês "Isotropic Volume Fraction").

O estudo da configuração arquitetural das estruturas cerebrais *in vivo*, por meio da dMRI associada aos métodos de tractografia, permitiu a reconstrução não invasiva das fibras neuronais e a exploração da informação direcional inerente às mesmas, sendo que o seu estudo tem revelado uma enorme expansão por meio do estabelecimento de marcadores biológicos perante a presença de diversas condições patológicas.

O objetivo principal desta dissertação prende-se com existência de uma variação proeminente nas métricas de difusão ao longo dos tratos de matéria branca no cérebro humano. Atualmente, a maioria dos estudos de tractografia tem por base uma abordagem que se resume à análise do valor escalar médio da métrica de difusão para a estrutura cerebral em estudo, pelo que se tem verificado um crescente interesse na utilização de métodos que considerem a extensão da variabilidade nas métricas de difusão ao longo dos tratos de modo a providenciarem um maior nível de detalhe ao nível do processo de difusão, evitando interpretações erróneas dos parâmetros microestruturais. Desta forma, em primeiro lugar, foi desenvolvido uma análise ao longo dos tratos de matéria branca, tendo por base a variação dos valores assumidos pelos parâmetros microestruturais acima mencionados.

No presente estudo foi possível demonstrar a eficácia de tal abordagem ao longo de três tratos de matéria de branca (fascículo arqueado, trato corticoespinhal, e corpo caloso), para além de permitir, através da variância assumida pelos diversos parâmetros microestruturais, o estudo detalhado de regiões anatómicas que assumem uma distribuição complexa de múltiplos conjuntos populacionais de fibras, como é o caso do centro semioval, o qual constitui uma região de cruzamento de fibras provenientes dos três tratos de matéria branca em estudo.

De seguida, esta técnica foi utilizada com sucesso na identificação de diferenças microestruturais por meio do estudo dos diversos parâmetros de difusão em pacientes com diagnóstico prévio de epilepsia no lobo temporal (TLE, do inglês "Temporal Lobe Epilepsy"), com foco epilético localizado no hemisfério esquerdo, e controlos. O estudo do ambiente microestrutural por meio dos múltiplos mapas escalares permitiu averiguar a alteração do processo de difusão e/ou anisotropia, associadas ao efeito fisiopatológico da TLE na organização da matéria branca. Os resultados revelaram diferenças localizadas, as quais se traduziram num aumento da difusividade e redução da anisotropia do processo de difusão ao longo dos tratos em estudo dos pacientes com TLE, sugerindo deste modo uma perda na organização das diversas estruturas anatómicas e a expansão do espaço extracelular face aos controlos. Verificou-se ainda que pacientes com esta condição neurológica sofrem de alterações microestruturais que afetam redes cerebrais em grande escala, envolvendo regiões temporais e extratemporais de ambos os hemisférios.

Adicionalmente, aplicada como técnica capaz de investigar padrões de mudança na matéria branca, procedeu-se à realização de um estudo assente na estatística espacial baseada no trato (TBSS, do inglês "Tract-Based Spatial Statistics"). Após a exploração das diversas métricas de difusão, os pacientes com TLE (com lateralização à esquerda) demonstraram alterações no processo de difusão, ilustradas pelos diversos padrões de mudança microestrutural de cada métrica em estudo, concordantes com os resultados anteriormente aferidos pela análise ao longo do trato.

Por fim, uma análise baseada em fixel (FBA, do inglês "Fixel-Based Analysis") foi realizada, a qual permitiu uma análise estatística abrangente de medidas quantitativas da matéria branca, com o intuito de detetar alterações no volume intra-axonal por variação na densidade intra-voxel e/ou reorganização da morfologia macroscópica. Para identificar tais diferenças entre pacientes e controlos, três parâmetros foram considerados: densidade das fibras (FD, do inglês "Fibre Density"), seção transversal do feixe de fibras (FC, do inglês "Fibre-bundle Cross-section"), e densidade de fibras e seção

transversal (FDC, do inglês “Fibre Density and Cross-section). Reduções na FD, FC e FDC foram identificadas em pacientes com TLE (com lateralização à esquerda) em comparação com os controlos, o que está de acordo com as mudanças microestruturais que resultam do processo de degeneração que afeta as estruturas de matéria branca com a perda de axónios na presença de uma condição neuropatológica como a TLE.

Apesar do resultado final positivo, tendo em conta a meta previamente estabelecida, está aberto o caminho para o seu aperfeiçoamento, tendo em vista as direções futuras que emergem naturalmente desta dissertação. Como exemplo disso, poder-se-á recorrer ao estudo pormenorizado das metodologias técnicas associadas à abordagem apresentada que tem por base a análise das métricas de difusão ao longo dos tratos de matéria branca, uma vez que o desvio padrão associado a cada valor atribuído pelas diversas métricas foi significativo, o que de alguma forma poderá ter influenciado os resultados e, consequentemente, as conclusões deles extraídas, tendo em vista a sua viabilidade enquanto aplicação clínica.

Como nota final, gostaria apenas de salientar que a imagiologia por difusão e, em particular, a tractografia têm ainda muito espaço para progredir. A veracidade desta afirmação traduz-se pela existência de uma grande variedade de modelos e algoritmos implementados, bem como de técnicas e metodologias de análise à informação microestrutural retida tendo por base o perfil de difusão que carateriza cada trato em estudo, sem que no entanto, exista consenso na comunidade científica acerca da melhor abordagem a seguir.

Palavras-chave: Ressonância magnética ponderada por difusão; Tractografia; Análise ao longo dos trato**s**; Estatística espacial baseada no trato (TBSS); Análise baseada em fixel (FBA).

Contents

List of Figures

List of Tables

List of Abbreviations

Abbreviation	*Explanation*
2D	Two-Dimensional
3D	Three-Dimensional
4D	Fourth-Dimensional
5TT	Five-Tissue-Type
ACT	Anatomically-Constrained Tractography
ADC	Apparent Diffusion Coefficient
AF	Arcuate Fasciculus
AFD	Apparent Fibre Density
AMICO	Accelerated Microstructure Imaging via Convex Optimization
BET	Brain Extraction Tool
CC	Corpus Callosum
CFE	Connectivity-based Fixel Enhancement
CNS	Central Nervous System
CSD	Constrained Spherical Deconvolution
CSF	Cerebrospinal Fluid
CST	Corticospinal Tract
DIPY	Diffusion Imaging In Python
dMRI	Diffusion-Weighted Magnetic Resonance Imaging
DT	Diffusion Tensor
DTI	Diffusion Tensor Imaging
EAP	Ensemble Average Propagator
EPI	Echo-planar Imaging
FA	Fractional Anisotropy
FBA	Fixel-Based Analysis
FC	Fibre Cross-section
FD	Fibre Density
FDC	Fibre Density and Cross-section
FID	Free Induction Decay
FLASH	Fast Low Angle Shot
FOD	Fibre Orientation Distribution
FOV	Field Of View
FSL	FMRIB Software Library

FT	Fourier transform
GE	Gradient-Echo
GM	Grey Matter
GRAPPA	GeneRalized Autocalibrating Partial Parallel Acquisition
HARDI	High Angular Resolution Diffusion-weighted Imaging
ICVF	Intracellular Volume Fraction
ISOVF	Isotropic Volume Fraction
MAP-MRI	Mean Apparent Propagator – Magnetic Resonance Imaging
MD	Mean Diffusivity
MR	Magnetic Resonance
MRI	Magnetic Resonance Imaging
MSD	Mean Squared Displacement
NDI	Neurite Density Index
NODDI	Neurite Orientation Dispersion and Density Imaging
OD	Orientation Dispersion
ODF	Orientation Density Function
ODI	Orientation Dispersion Index
PDF	Probability Density Function
PE	Phase-Encoding
PGSE	Pulsed Gradient Spin Echo
RF	Radio-Frequency
ROI	Region Of Interest
RTAP	Return to Axis Probability
RTOP	Return to Origin Probability
RTPP	Return to Plane Probability
SE	Spin-Echo
SD	Standard Deviation
SHORE	Simple Harmonic Oscillator based Reconstruction and Estimation
SIFT	Spherical Deconvolution-Informed Filtering of Tractograms
SLF	Superior Longitudinal Fasciculus
SVD	Single Value Decomposition
TE	Echo Time
TFCE	Threshold-Free Cluster Enhancement
TLE	Temporal Lobe Epilepsy
TR	Repetition Time

1 Introduction

It is commonly acknowledged that the human brain is the most complex system in nature. The presence of pathological conditions in its intricate structure may lead to a wide variety of neurological disorders, such as epilepsy. Epilepsy is a chronic neurological condition that is characterized by recurrent seizures, which are brief episodes of a sudden surge of electrical activity in the brain that result in a temporary disturbance of motor, sensory, or mental functions and may affect a part of the body (partial or focal seizures) or the entire body (generalized seizures). [1, 2]

According to Epilepsy Society of the United Kingdom, this neurological disorder affects over 500,000 people in this country, 160,000 of which require continuing hospital-based medical treatment. [3] Most patients respond completely to antiepileptic drugs and become seizure free. However, in 30% of patients with focal epilepsy, seizures are refractory to medication and surgery is potentially curative if an epileptic focus is localized, with up to 70% being rendered seizure free. The most common form of focal or location related epilepsy is temporal lobe epilepsy (TLE), accounting for approximately 60% of all people living with epilepsy. [4, 5]

In recent years, with the fast advance of imaging techniques, the opportunity of mapping the human brain pathways *in vivo* at unprecedented resolution became a reality, remaining today one of the most challenging tasks in neuroscience. In addition, pathophysiological models of brain disorders have shifted from an emphasis on understanding pathology in specific brain regions to characterizing disturbances of interconnected neural systems. Specifically, of importance for clinicians and researchers managing patients with epilepsy, new methods of brain imaging in search of the seizure-producing abnormalities have been implemented, looking also in detail to the information provided by the microstructure about the diffusion profile, derived from diffusion Magnetic Resonance Imaging (MRI), along specific white matter (WM) pathways that could be potentially affected by this neurological condition.

With this in mind, the main goal of this project was the integration of microstructural information derived from multi-shell diffusion imaging (which involves acquiring a large number of gradient directions for the two or more spherical shells (i.e. several *b-values*)) with tractography, through the definition of a microstructural signature based on an along-tract analysis of each cerebral pathway in study, namely the arcuate fasciculus, the corticospinal tract and the corpus callosum.

Additionally, in order to be able to distinguish each WM pathway within a complex region with multiple fibre populations (as the centrum semiovale), along-tract analysis considering the variation of different microstructural scalar maps along each tract was performed in a carefully delineated region. This analysis was repeated for a complex region and results compared with individual tract signatures. The same reasoning was applied to compare each WM tract of interest between a clinical population with TLE and a healthy control group.

Two additional group level analyses were performed as well in order to support the conclusions derived from the along-tract analysis, namely the traditional voxel based tract-based spatial statistics (TBSS) and the more recent fixel-based analysis (FBA).

This thesis is organized in twelve chapters described below, with the present Chapter 1 introducing the context, motivation and general organization of the work.

Chapter 2 introduces a comprehensive explanation of the relevant theoretical underpinnings of this work. This chapter is subdivided into six sections where the Neuroanatomy, Magnetic Resonance Imaging (MRI), Diffusion-Weighted Magnetic Resonance Imaging (dMRI), Diffusion Tensor Imaging (DTI), High angular resolution diffusion-weighted imaging (HARDI) and Tractography are introduced. The first section introduces a brief description of neuroanatomy, looking in detail to the arcuate fasciculus, corticospinal tract, corpus callosum and centrum semiovale. The second section describes

the MRI basic principles, followed by a description of the imaging principles and MR sequences. The third section explains the diffusion principles and the Pulsed Gradient Spin Echo (PGSE) sequence is introduced. Followed by the fourth section, where DTI is described as well as its limitations. In the fifth section, an overview of HARDI methodologies is given, on which the Simple Harmonic Oscillator based Reconstruction and Estimation (SHORE) and Mean Apparent Propagator (MAP) – MRI are presented, and the spherical deconvolution and Neurite orientation dispersion and density imaging (NODDI) explained, as well as the Accelerated Microstructure Imaging via Convex Optimization (AMICO) framework. Finally, in the last section, a brief introduction to tractography will be addressed with a focus on its achievements and associated limitations.

In Chapter 3, subjects' information, dMRI acquisition and processing methodology will be addressed.

In Chapter 4, the methodology used for tractography reconstructions of each WM tract of interest will be described. It is also given a detailed description about how the different microstructural parameters in study were obtained.

In Chapter 5, Chapter 6 and Chapter 7, the different analyses that were performed in order to evaluate the microstructural parameters will be introduced: Along-tract analysis, TBSS and FBA, respectively; with each one containing the results obtained from the associated methodologies previously explained. Each Chapter will also comprise a detailed discussion of the results from each analysis performed.

Finally, in Chapter 8, the conclusion of the entire dissertation is presented, followed by the future perspectives of this work in Chapter 9.

Additionally, the references used along this dissertation are enumerated in Chapter 10, and the most relevant scripts that were developed during this research project can be found in Chapter 11, as well as some complementary information important to the analyses carried out.

Finally, in Chapter 12 it is shown an example of the abstracts submitted for the VII AEICBAS Biomedical Congress, which will take place in Porto (Portugal), and for the 2019 Annual Meeting of the Organization for Human Brain Mapping (OHBM), which will take place in Rome (Italy).

2 Background Theory

2.1 Neuroanatomy

In this first section, a brief description of human neuroanatomy is introduced and the basis of brain microstructural organization explained. Posteriorly, the neural connectivity of the arcuate fasciculus, corticospinal tract and corpus callosum, as well as the centrum semiovale, where there are crossing fibres from these three WM pathways, will be also described.

2.1.1 A brief description of neuroanatomy

The central nervous system (CNS) is responsible for controlling processes ranging from sensory perception to advanced cognitive functions. The functional unit of CNS is the neuron, which is responsible for the propagation of the electric activity and flux of information in the nervous system. A neuron can present a variety of shapes and sizes, all displaying, however a common structure made up of: the cellular body which contains the nucleus, dendrites responsible for receiving the stimulus, and axons, which transport the action potential and connect to other neurons via the synapses to transmit the electric impulse. Our nervous system is organized in such fashion that axons tend to run alongside each other, while cellular bodies and dendrites group together. [6, 7]

At a larger scale, we can define grey matter (GM) as being composed of the cellular bodies of neurons and also unmyelinated axons. GM covers the surface of the cerebral hemispheres and builds up the cortex, displaying a pinkish-grey colour due to an abundant blood supply. [6]

On the other hand, WM is the compartment of the nervous system comprised of axons, which are organized into fibre bundles, with long WM fibre bundles being called fasciculi or tracts. WM is mainly studied as the brain compartment of crossing paths that connect different functional regions. Long distance fibres, generally gathered into bundles, can be classified according to their connection patterns. Commissural fibres connect the two cerebral hemispheres; projection fibres are bidirectional fibres between the sub-cortical structures and the cortex, such as the thalamus, brainstem and spinal cord; and, associative fibres regroup cortico-cortical fibres between intra-hemispheric regions and fibres of the limbic system. [8, 9]

Concurrently and subsequently to the organization of WM networks, fibre connections become progressively mature and functionally efficient through the myelination process (elaboration of myelin surrounding neuronal axons) that favours the conduction of the nervous impulse. [9]

Interwoven between deep GM structures and the cortex there are cavities in the brain named ventricles, containing a plasma-like liquid named Cerebrospinal Fluid (CSF). The CSF is responsible for establishing the exchange of nutrients between the blood and nervous tissue, additionally acting as a cushion for impacts on the brain. [6]

2.1.1.1 Neural connectivity of the arcuate fasciculus

The arcuate fasciculus is a lateral associative bundle part of the superior longitudinal fasciculus (SLF) and composed of long and short fibres connecting the perisylvian cortex of the frontal, parietal, and temporal lobes. This frontotemporal fibre bundle consists of a longer, direct segment connecting Wernicke's area to Broca's area, and two indirect segments: an anterior part linking Broca's area with the inferior parietal lobule and a posterior part linking inferior parietal lobule with the superior-temporal gyrus and sulcus (Wernicke's area); whose separate functions correlate with traditional models of conductive and transcortical motor or sensory aphasia, respectively (see **Figure 2.1**). [10, 11, 12]

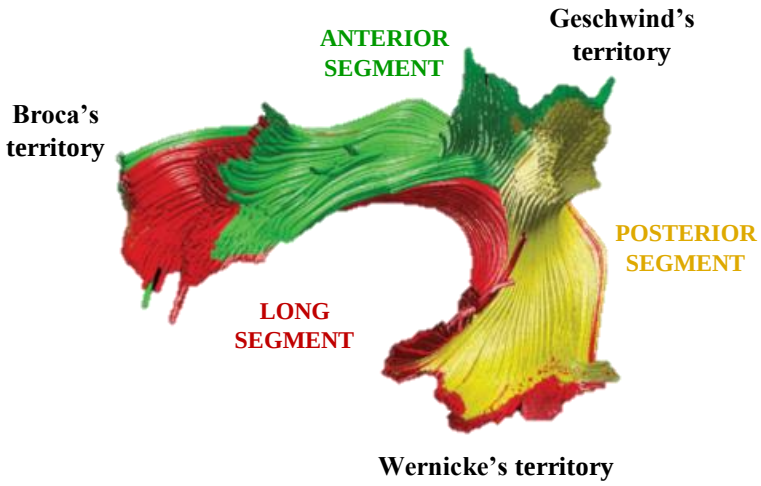

Figure 2.1 | Tractography reconstruction of the arcuate fasciculus. Broca's and Wernicke' territories are connected through direct and indirect pathways in the average brain. The direct pathway (long segment shown in red) runs medially and corresponds to classical descriptions of the arcuate fasciculus. The indirect pathway runs laterally and is composed of an anterior segment (green) connecting the inferior parietal cortex and Broca's territory, and a posterior segment (yellow) connecting Geschwind's and Wernicke's territories. Adapted from [12].

The arcuate fasciculus is considered a major WM tract traditionally implicated in language, and studies of healthy adults have demonstrated a relationship between its symmetry and performance on a word list recall task. [13] Like language function itself, the arcuate fasciculus is believed to be left-lateralized in the majority of adults [14] and children [15]. The relationship between structural lateralisation of this WM pathway and functional lateralisation of language is not always transparent. [16, 17] However, it is evident that its structural properties are correlated with behavioural measures of language function, such as word learning [18], verbal recall [14] and the development of phonological awareness and reading [19].

Previous studies also suggest that the arcuate fasciculus of the left hemisphere is involved in language [20] and praxis [21], while the arcuate fasciculus of the right hemisphere is involved in visuospatial processing [22] and some aspects of language such as prosody and semantic [14, 20].

Arcuate fasciculus abnormalities have been documented in paediatric populations that exhibit language impairments of varying severity, as part of a more globally affected profile including cognitive involvement, and in developmental populations with a primary or specific language impairment. [10]

2.1.1.2 Neural connectivity of the corticospinal tract

In humans the motor development is achieved by functional use of trunk and limb muscles. In detail, this motor development is generally divided into two different types of motor skills, gross motor skills, which mainly require the use of proximal and axial muscles for postural control and locomotion; and fine motor skills, responsible by precise movements. These motor functions are related to the descending motor pathways classified as the corticospinal tract (pyramidal tract) and the non-corticospinal tract (extra-pyramidal tract). [23, 24]

However, in this section, the focus will be the corticospinal tract, which reveals to be primarily involved in fine motor skills, playing a major role in cortical control of spinal cord activity.

The corticospinal tract, which starts at the cortex and terminates on motor neurons in the spinal cord (see **Figure 2.2**), is a complex system with multiple functions that share one characteristic, namely cortical control of spinal cord activity. These functions include the control of afferent inputs, spinal reflexes, and motor neuron activity. So, the corticospinal tract plays an important role in the motor system, as it mediates voluntary distal movements. Most corticospinal tract axons cross the anatomical

midline at the junction between the brainstem and spinal cord, forming the pyramidal decussation. This is of critical importance for corticospinal tract functions, as it means the right side of the brain controls the left side of the body, and vice-versa. [25, 26]

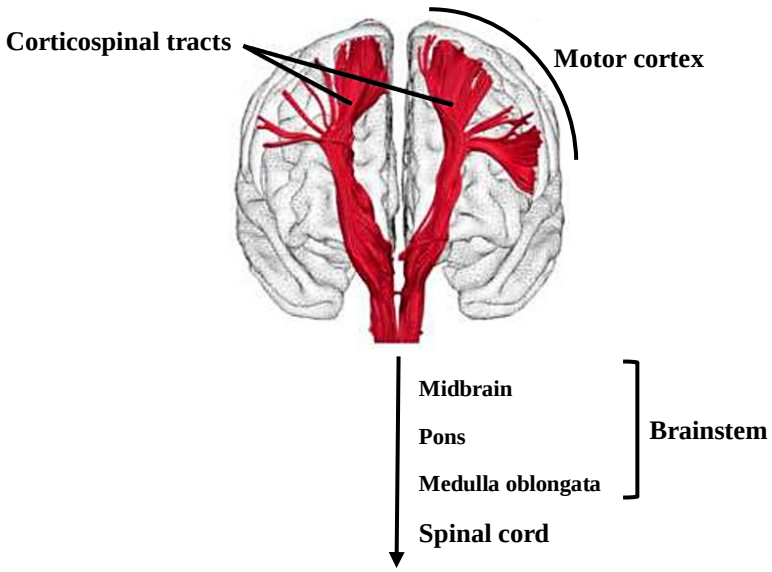

Figure 2.2 | Virtual dissection of the corticospinal tract in the human brain. The corticospinal tract contains descending fibres projecting from the motor cortex to spinal cord, passing through the posterior limb of the internal capsule, the ventral midbrain, continuing through the pons, and passing through the medulla oblongata, where corticospinal fibres collect into a discrete bundle forming the pyramid. Adapted from [26].

This WM pathway is closely linked to the development of skilled voluntary movements through evolution. In maturity, motor skills depend on the corticospinal tract, as well as brainstem motor pathways. The motor output from the cortex descends into the brainstem and to the spinal cord to control the musculature through motor neurons. Descending signals to motor neurons and interneurons, in order to mediate the voluntary control, can be distinguished from muscle and joint sensory signals that provide feedback for movement control. While genetic mechanisms initially establish motor system connections, neural activity and associated processes refine these connections to enable motor skills to develop. [24,27]

2.1.1.3 Neural connectivity of the corpus callosum

The corpus callosum, which is the most important fibre pathway linking both hemispheres, plays a key role in information access, as well as the functional coordination and reorganization between hemispheres, ensuring the communication between sensory, motor, and higher-order brain regions. Consisting of over 190 million axons, the corpus callosum is the largest WM structure in the brain and the major commissural pathway connecting the hemispheres of the human brain, and it is involved in several motor, perceptual and cognitive functions. [28, 29]

Based on previous histological findings [13, 30, 31, 32], from anterior to posterior, the corpus callosum could be anatomically divided into four parts: the rostrum, genu, body, and splenium, each responsible for connecting distinct areas of the cortex (see **Figure 2.3**). The connection of the orbital regions on the frontal lobes is mediated by the rostral fibres. The genu fibres are crossing over to contribute to the forceps minor (anterior forceps), connecting the homologous lateral and medial regions of the frontal cortices, whereas by following a posterior course the fibres of the splenium contribute to the forceps major (posterior forceps), providing a connection between the occipital lobes. Following a

traversal direction towards to cerebral cortex, body fibres form the corona radiata along with other major WM pathways.

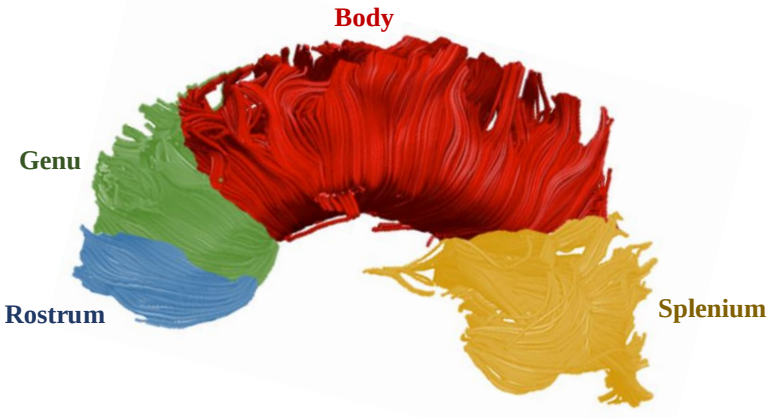

Figure 2.3 | Left lateral view of the tractography reconstruction of the corpus callosum segmented in four different parts: rostrum (blue), genu (green), body (red), and splenium (yellow). Adapted from [31] and [32].

The importance of corpus callosum has grown beyond interhemispheric communication, and recently several studies [33, 34] have determined changes in corpus callosum volumes associated with neurodegenerative or inflammatory diseases such as Alzheimer's [35] and multiple sclerosis [36]. However, some neuroimaging studies have also revealed that the structure of the corpus callosum seem to be affected by a variety of CNS diseases, such as epilepsy [37] and autism [38].

2.1.1.4 Neural connectivity of the centrum semiovale

The centrum semiovale, which has particularly complex crossing-fibre characteristics, is defined as the common central mass of WM with a semi-oval shape, present in each of the cerebral hemispheres, and subjacent to the cerebral cortex just above the level of the lateral ventricles (see **Figure 2.4**). [39, 40, 41]

Previous studies [39, 42, 43] have shown that this is a highly complex region of the WM. Within the centrum semiovale, the arrangement of the fibres reveals three-way intersection consisting of mediolaterally directed commissural fibres of the corpus callosum, vertically oriented projection fibres of the corticospinal tract, and anterior–posterior association fibres comprising part of the arcuate fasciculus.

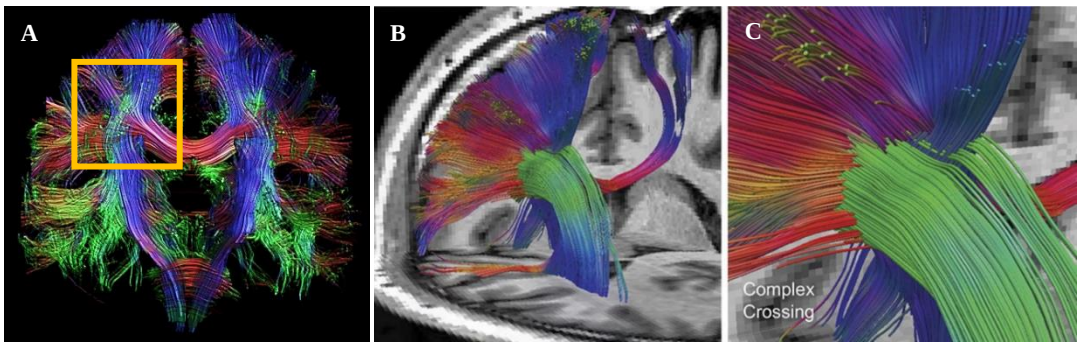

Figure 2.4 | (A) Whole-brain probabilistic fibre-tracking generated using constrained spherical deconvolution (CSD) algorithm from a diffusion dataset. The region that corresponds to centrum semiovale is highlighted by a yellow square. Each track is coloured according to its direction of travel (red: left–right; green: anterior–posterior; blue: inferior–superior). **(B)** High-definition fibre tractography at the level of the centrum semiovale revealing the complex architecture of this region. **(C)** Close-up view of (B) highlighting the complex crossing-fibre characteristics of the centrum semiovale. Adapted from [39] and [41].

2.2 Magnetic Resonance Imaging

In this section, the principal theoretical concepts required in order to understand the main content of the remaining sections of this dissertation are given, starting by an introduction to Magnetic Resonance Imaging (MRI).

MRI is a nuclear medical imaging technique that allows imaging *in vivo* the human morphology, structure and dynamics with a high contrast and resolution at tissue level. This non-invasive 3D technique uses magnetic fields and electromagnetic energy to generate signals from the atomic nuclei, in particular, the hydrogen nuclei (proton of the nuclei), which can be translated into images. Other nuclei may be used in MRI but there is a preference for hydrogen due to its abundance in fat and in water ((Hinshaw & Lent, 1983) [44]; (Pope, 1999) [45]). MRI allows for a great variety of sequences to be obtained when different acquisition parameters are changed, depending on the specific objective of the study. In the followed subsections, the concepts related to MRI will be explained.

2.2.1 Basic Principles

In the absence of an external magnetic field, the protons assume random directions and orientations, and their individual magnetic fields tend to cancel out. Otherwise, in the presence of an external homogenous magnetic field (B_0), the spins preferentially align themselves with the direction of the field. They may align themselves either parallel (spin-up) or anti-parallel (spin-down) to the field, and this constitute two slightly different energy states, which are given by:

$$E = \mu . B_0 = \gamma \hbar I . B_0 \qquad \text{with} \qquad \mu = \gamma J = \gamma \hbar I \tag{2.1}$$

where μ is the magnetic moment, γ the gyromagnetic ratio, J the angular momentum, $\hbar$ the Planck's constant divided by 2π, I the spin angular momentum that can be $\pm\, 1/2$ for protons, and B_0 the external magnetic field. [46]

The spin-up (parallel) state has a slightly lower energy than the spin-down (anti-parallel) state. The energy difference between both levels is the energy needed for a proton to swap between the two states, which is associated with the electromagnetic frequency required. The energy difference is given by:

$$\Delta E = \gamma \hbar . B_0 \tag{2.2}$$

Additionally, instead of a perfectly alignment with the external magnetic field B_0, the spinning protons steadily precess about its direction, developing a precessional movement towards it with an angular frequency ω (rad/s), which is directly proportional to B_0, and mathematically defined as:

$$\omega = \gamma B_0 \tag{2.3}$$

In terms of frequency (Hz) and knowing that $f(Hz) = \frac{\omega}{2\pi}$, an associated expression can be derived

$$f = \frac{\gamma B_0}{2\pi} \tag{2.4}$$

where f is known as the Larmor Frequency. [45, 46]

2.2.1.1 Radio-Frequency Pulses

Due to a predominance of magnetic moments oriented with the magnetic field, a component arises resulting of the vectorial sum of the magnetic moments oriented with the field. This component is called longitudinal magnetization M_0, parallel to the main magnetic field. This, however, cannot be measured since it is parallel to the large externally applied field B_0.

Since we can only measure magnetic field disturbances, to detect the precession of spins it is necessary to divert them from the main orientation of magnetic field and to do so, another magnetic field B_1, namely a radiofrequency (RF) pulse with the Larmor frequency is applied perpendicularly to M_0, in order to resonate with the spin system. In this framework, M_0 will appear stationary, and the application of another magnetic field B_1 tips M_0 into the xy plane, creating a transverse magnetization M_{xy} (perpendicular to their spinning axis), which now precesses around B_1. The extent and intensity of the RF pulse allows one to control the tip/flip angle of the longitudinal magnetization to the xy plane. [46, 47]

The flip-angle (α) depends on the amplitude of B_1 and duration t_p of the RF field and can be calculated by:

$$\alpha = \gamma \int_0^{t_p} B_1(t)\, dt \qquad (2.5)$$

2.2.1.2 Relaxation

When the RF pulse stops, the magnetization gradually returns to equilibrium and, consequently, its evolution over time is dominated by relaxation mechanisms, induced by the loss of energy to the surrounding environment (Spin-Lattice interaction) and the interaction between spins (Spin-Spin interaction) ((Hashemi *et al.*, 2012) [47]; (Plewes & Kucharczyk, 2012) [48]).

The spin-lattice interaction (also known as T_1 relaxation) results in the recovery of the longitudinal magnetization along z axis (M_z) after applying a RF pulse. This mechanism reflects the time necessary to realign the protons with B_0 by transferring protons energy to surrounding molecules. So, T_1 relaxation could be defined as the time taken for 63% of longitudinal magnetization to recover along z axis, after 90°RF pulse application, leading to the passage of the spins from the anti-parallel level to parallel level, with energy devolution to the lattice (see **Figure 2.5**). This change in spins state happens mainly due to an interaction with magnetic fluctuations of the lattice, and the time it takes depends on the mobility of protons in different molecules. Mathematically, T_1 relaxation is explained by an exponential behaviour according to:

$$M_z(t) = M_0\left(1 - e^{\frac{-t}{T_1}}\right) \qquad (2.6)$$

Otherwise, spin-spin interaction (or T_2 relaxation) is the mechanism that results in a decrease of M_{xy} after applying a RF pulse. For a 90° flip-angle, T_2 relaxation corresponds to the time it takes for 37% of M_{xy} to be obtained due to relaxation of transverse magnetization, from a certain value, which is determined from the RF pulse duration/intensity (see **Figure 2.5**). Mathematically this process is explained through the equation 2.7:

$$M_{xy}(t) = M_0\, e^{\frac{-t}{T_2}} \qquad (2.7)$$

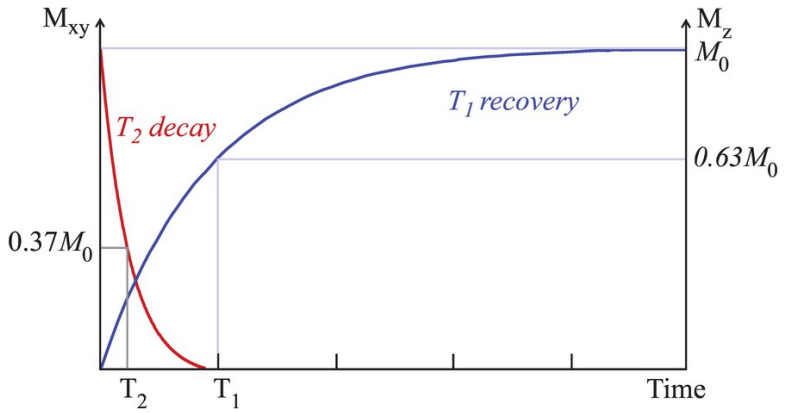

Figure 2.5 | T_1 and T_2 relaxation times. Although they happen simultaneously, T_2 is much quicker than T_1 for a certain tissue. This fact cannot be visible in other tissues because the relation between both curves can be different. Adapted from [46].

Furthermore, T_2 is also influenced by the inherent field inhomogeneities. In this case, the relaxation will occur at a rate of $T_2{}^*$, which is shorter than T_2 because it leads to faster dephasing. $T_2{}^*$ is given by:

$$\frac{1}{T_2{}^*} = \frac{1}{T_2} + \frac{1}{T_{inhom}} = \frac{1}{T_2} + \gamma \Delta B \qquad (2.8)$$

where γ is the gyromagnetic ratio and ΔB the relaxation rate contribution attributable to field inhomogeneities across a voxel.

2.2.2 Image Principles

2.2.2.1 Slice Selection / Image Acquisition and Reconstruction

If a coil is placed perpendicularly to the precessing M_{xy}, a voltage will be induced accordingly to Faraday's law of induction ($\varepsilon = -d\phi_B/dt$, where ϕ_B is the magnetic flux). The measured signal consists in an oscillating voltage according to the Larmor frequency which is exponentially decaying with time and is generally called Free Induction Decay (FID), since the spins are "freely" precessing. The FID is detected from the sample without any spatial discrimination and, in order to get that, magnetic field gradients can be used. [49] Spins affected by a magnetic field gradient will have a slightly different precessional frequency according to their position (z), and the intensity of the measured signal will then reflect the anatomical structure at different positions.

Firstly, a gradient G_z is applied (conventionally in the same direction as static magnetic field – z direction) in order to select a region of interest (ROI), in a process known as *Slice-selection*. The RF pulse is set up with a certain bandwidth ($\Delta\omega$) in order to stimulate a region (i.e. a 2D slice). The thickness of the excited slice (Δz) depends on the $\Delta\omega$ of the RF pulse and the steepness of the gradient (see **Figure 2.6**). [44, 45, 46]

$$\Delta z = \frac{\Delta\omega}{\gamma\, G_z} \qquad (2.9)$$

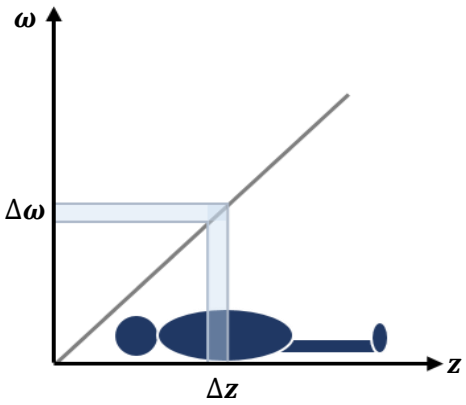

Figure 2.6 | Principle of slice selection. By applying a Radio-Frequency (RF) pulse with a finite bandwidth ($\Delta\omega$), only the spins in a slice thickness (Δz) are excited. Adapted from [46].

After the slice has been selected, extra steps are required to get individual information from each voxel. Once again, a gradient is applied in order to encode the spins in the slice, because the *Slice-selection* method does not differentiate between protons within each slice. As a result, protons precess with slightly different speeds, originating phase differences proportional to their positions (Phase-Encoding Gradient, G_y, conventionally applied along y). Finally, during the echo readout (i.e. while sampling the signal) and the application of the Frequency-Encoding gradient, G_x, in the x direction, the spins precess at a different rate along this axis, yielding a 3D encoding of the spin ensemble. By applying these gradients we linearly vary the frequency with spatial position. [46, 50]

Therefore, to achieve a full description of the sample, this procedure must be repeated several times, which is determined by the Repetition Time (T_R) - the time from the application of an excitation pulse to the application of the next pulse. The sampled signals are stored as spatial frequencies that vary with position, in what is called *k-space*, whose axes correspond to the integral of the applied gradients over time. In practice *k-space* is sampled over a grid and the separation between each sample is determined by the Field of View (FOV) of the desired image. [47] In the simplest type of *k-space* encoding, each repetition of the spin-echo experiment corresponds to a spatially encoding step, and one line in *k-space*. Since the data stored in *k-space* are spatial frequencies of the image (where the central ones contribute with image contrast and most part of the signal of tissues, while peripheral frequencies provide high detail about the image itself, but little information about contrast), by performing the inverse Fourier transform (FT), the reconstruction of an image from the spatial frequency space (*k-space*) can be computed. For 2D imaging, a 2D FT is applied, yielding a function that describes the distribution of spatial frequencies k_x and k_y, which are related to the time on gradient variables. While for 3D images, one more spatial frequency (k_z) and coordinate (z) should be considered. Consequently, 3D FT is applied for 3D imaging. [51]

2.2.2.2 Imaging Sequences

MRI pulses sequences are widely important allowing the acquisition of images with different kinds of contrast. There is a great variety of sequences in MRI, however I will only focus on Spin-Echo (SE), Gradient-Echo (GE), and Echo-planar Imaging (EPI), attending to their importance to understand further concepts along this dissertation.

2.2.2.2.1 Spin-Echo (SE)

In this MRI imaging sequence, after the application of a 90º RF excitation pulse, which is followed by a time span t where a gradient field G_y is applied to spatially encode the spins, a 180º RF pulse is applied in order to obtain the refocusing of the spins along with the same slice selective gradient. Consequently, by changing the orientation of spin precession, the ones that were precessing faster are now behind those that precessed at a lower frequency, which will lead to a regain of coherence after the same amount of time t, and to the emission of a spin echo, since phase differences will cancel out. The amount of time that goes between the application of 90º RF excitation pulse and the peak of the signal induced in the coil (maximum of the echo) is called Echo Time (T_E), when is also acquired the signal (echo). [46, 47]

A schematic overview of a SE sequence and respective sampled *k-space* is illustrated in **Figure 2.7**. As shown and according to the concepts introduced by ***Section 2.2.2.1***, after the application of the 90º RF excitation pulse simultaneously with a slice selection gradient, G_y is applied. The amplitude of this gradient determines the coordinate k_y of the line that will be sampled in *k-space* (orange line in **Figure 2.7**). Then, the 180º RF pulse is applied with the same slice selection gradient in order to flip the spins and make them rotate back towards coherence. Followed by the acquisition of the signal around T_E, while the k_x direction of the *k-space* (blue line in **Figure 2.7**) is scanned after the G_x along the x-axis has been switched on. Usually, G_x with the same polarity is applied during G_y in order to move the *k-vector* towards the beginning of the line that is to be acquired (negative k_x). Furthermore, to acquire the others *k-space* lines, the process has to be repeated according to a determined T_R.

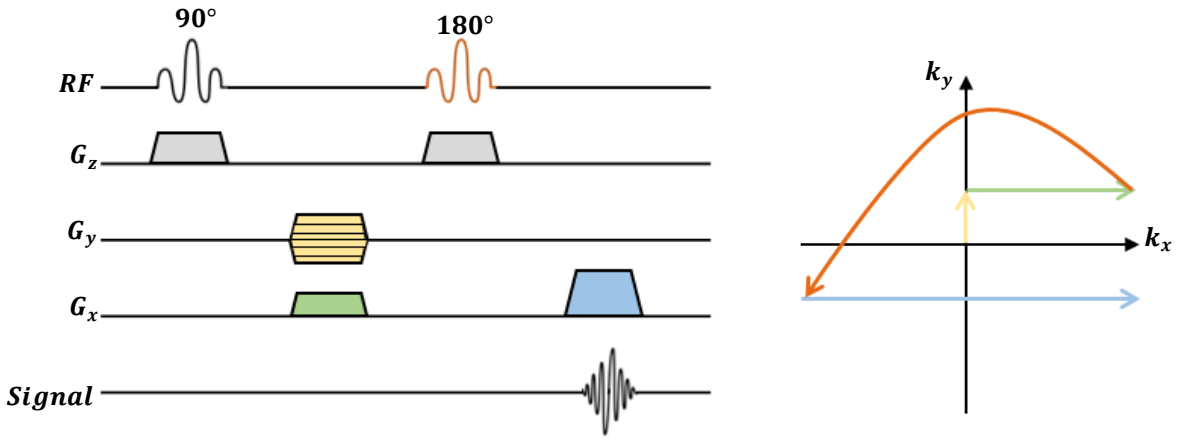

Figure 2.7 | Spin-Echo (SE) sequence: diagram of a 2D SE sequence (right) and the *k-space* trajectory in the k_x and k_y plane (left). The data is acquired, while scanning the blue line in *k-space.* Adapted from [46].

2.2.2.2.2 Gradient-Echo (GE)

When compared to SE sequence this technique allows reduced acquisition times, which could be accomplished by choosing a nutation angle (α) below 90º, in order to allow a more rapid longitudinal magnetization recovery.

The application of the GE sequence is characterized by the use of gradients to diphase and rephase the spins, instead of the 180º RF pulse. This sequence starts with the application of an initial 90º RF excitation pulse, simultaneously with the slice selection gradient. Then, by turning off the excitation pulse, the spin population gradually starts to precess with different frequencies (spins diphase), and G_y is applied along the *y*-axis. Simultaneously, a negative G_x is applied along the x direction in order to induce a faster dephasing of the spins. Thereafter, a positive G_x (gradient with

inverse polarity and same intensity) is applied to rephase the spins at the same time as the echo is measured (T_E) (see **Figure 2.8**, left). [46] The amplitude of the gradient determines the k_x and k_y coordinates of the line, which will be sampled in *k-space* (see **Figure 2.8**, right), as well as in the SE sequence.

Furthermore, since the refocusing of spins is purely based on gradients, and not on a 180° pulse, local field inhomogeneities arise due to susceptibility effects which are not compensated by the echo. Thereby, the signal is dependent of T_2^* rather than T_2, resulting in the acquisition of T_2^* - weighted images instead of T_2 - weighted images

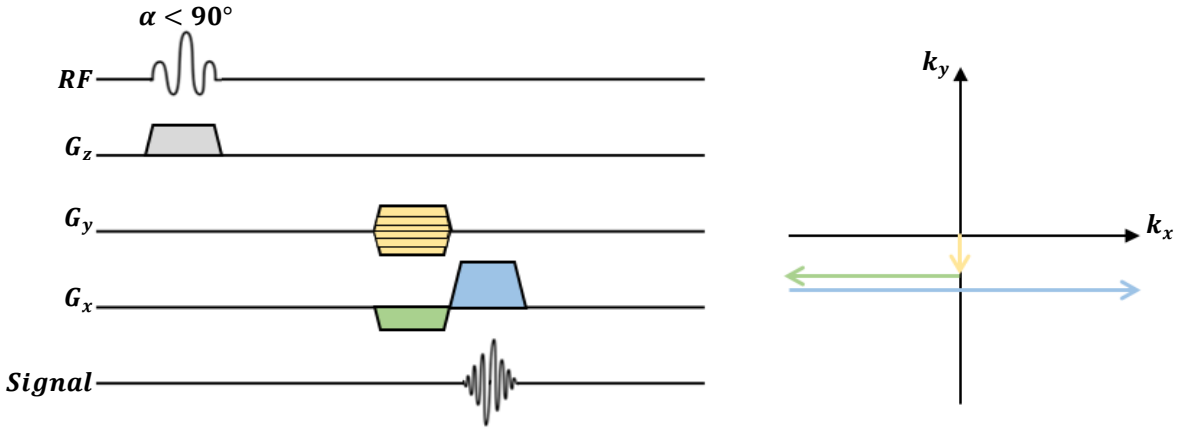

Figure 2.8 | Gradient-Echo (GE) sequence: diagram of a 2D GE sequence (left) and the *k-space* trajectory the k_x and k_y plane (right). Adapted from [46].

2.2.2.2.3 Echo-planar Imaging (EPI)

EPI is one the fastest methods for data collection, generating images in the order of tens of milliseconds. This imaging sequence uses multiple GE with different phase steps in order to sample the *k-space*, with multiple lines being acquired after a single 90º RF excitation. [52, 53]

Thereby, as a conventional SE sequence, an SE EPI sequence begins with 90° and 180° RF pulses. However, after the 180° RF pulse, the frequency-encoding gradient G_x oscillates rapidly from a positive to a negative amplitude, which consequently generates a train of gradient-echoes with same intensities; while simultaneously is applied blips in the phase-encoding gradient G_y which act as individual phase encoding steps. Further, each echo is phase encoded differently by phase-encoding blips on the phase-encoding axis. Each oscillation of G_x corresponds to one line of imaging data in *k-space*, and each blip corresponds to a transition from one line to the next in *k-space*. In GE EPI sequences, after a single 90º RF excitation pulse, the acquisition of the image is performed, using the gradient to generate the echoes following the same process explained before. [54, 55] A schematic representation of a 2D SE and GE EPI sequence is illustrated in **Figure 2.9**.

Allied to this strategy there are however some essential requirements that should be followed in terms of how fast gradients can change and the maximum intensity they can achieve. Furthermore, the rapid switching of the gradients, produces an electric field at any closed conducting surface, which may lead to the generation of eddy currents. The field generated by the eddy currents combines with the intended gradient field to create waveforms distortions, which can result in images artefacts and signal loss. In particularly, it changes the nominal diffusion weighting by biasing the expected gradient intensity and leads to geometrical distortions in the acquired images. Additionally to eddy-current

distortions, we can also have susceptibility artefacts when the local magnetic properties of the object are different, producing additional gradients that distort the acquired images. [56]

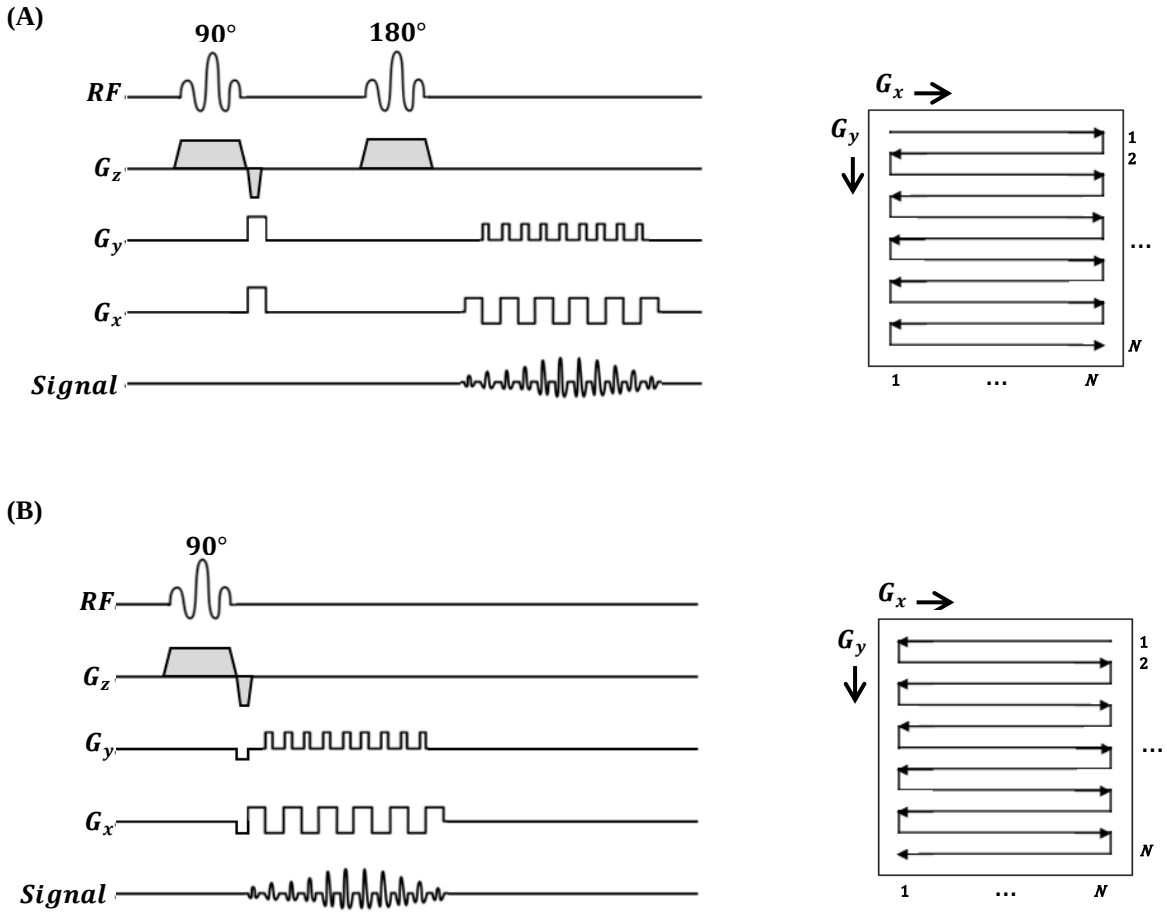

Figure 2.9 | 2D Echo-planar Imaging (EPI) sequence and respective *k-space* trajectory: **(A)** diagram of 2D Spin-Echo (SE) and *k-space* trajectory, and **(B)** diagram of 2D Gradient-Echo (GE) and *k-space* trajectory. Adapted from [55].

2.3 Diffusion-Weighted Magnetic Resonance Imaging

Throughout this section, the concept of diffusion is introduced with the methods that have been developed to study it. The details discussed below are essential to understand the behaviour of how water molecules interact with biological tissues, and how the measures, that are reconstructed with diffusion imaging, are influenced by those interactions.

Diffusion-Weighted Magnetic Resonance Imaging (dMRI) is a neuroimaging method capable of mapping the diffusion of water molecules across biological tissues. Water molecules interact with many obstacles, such as cell membranes and axonal fibres, and by studying their diffusional process we can recover patterns that can reveal microscopic details about brain tissue architecture, such as axonal orientation. Hence, water diffusion patterns have been useful to reflect the underlying microstructural organization of the brain.

2.3.1 Diffusion Principles

Diffusion is a physical phenomenon that was mathematically described by Fick, based on the random displacement of molecules in a fluid. This phenomenon is explained by Fick's first law by attributing the generation of a flux *J* from a particular substance to a gradient of concentration (∇_C) at a particular position *r* and time instance *t*:

$$J(r,t) = -D\nabla_C(r,t) \qquad (2.10)$$

where *D* is a constant of proportionality, called the diffusion coefficient (mm^2/s) given by the diffusion coefficient of the substance under study. This law takes into account that the direction of displacement takes place from areas of high to low concentration (Fick, 1855) [57].

Based on the principle of conservation of mass and supported by the idea the evolution of the concentration of particles can be derived at any particular point in time from the difference between the influx and efflux at a specific position (Price, 1997) [58], Fick's second law was postulated:

$$\frac{\partial c(r,t)}{\partial t} = D\nabla^2 c(r,t) \qquad (2.11)$$

However, the gap between the effect described by Fick and the initial microscopic observations was only filled out several years later by Albert Einstein (1905), who was responsible for quantifying diffusion as the random thermal motion of molecules in the absence of any external forces. More specifically, a relationship was drawn by introducing an explicit relationship between the mean-squared displacement (x) of molecules undergoing diffusion during a particular time interval ($\Delta\tau$), the diffusion coefficient (*D*) and the dimensions across which they spread (n):

$$\langle x^2 \rangle = 2\, n\, D\Delta\tau \qquad (2.12)$$

It should also be stated that diffusion depends on the temperature, molecular weight and viscosity of the medium (Le Bihan, 1995) [59]. The laws described above shed light on the behaviour of molecules in unbound diffusion, where there is no preferential direction of displacement, a process also known as isotropic diffusion (Philibert, 2006) [60].

However, there are numerous restrictions to the diffusion of molecules in the human body, contributing to a displacement profile of water molecules that is no longer uniform. In particular, there are barriers such as cell membranes and axon fibres, amongst others, which lead to an anisotropic diffusion that is not constant across directions (Moseley *et al.*, 1990) [61]. Particularly for axonal fibres, diffusion occurs preferentially along the axon's major axis and is lower in the transverse direction(s) ((Mori & Barker, 1999) [62]; (D. C. Alexander, 2006) [63]). Even though the main sources of anisotropy are still under debate, the dense packing of axons and the myelin sheath that surrounds them, has been shown to play a very important role in restricting diffusion in the transverse direction (Beaulieu, 2002) [64]. Currently, the recovery of the full information about water molecules displacement - given by the diffusion probability density function (PDF) or diffusion propagator – in biological tissues has been an active topic of research.

The propagator gives the probability of a particular molecule having moved from an initial position r_0 to a final position r within a specific time interval t, with a corresponding displacement given by $R = r - r_0$. [65] The averaged propagator could be obtained through the integration of $P(r_0, r + R, t)$ for a particle over all possible initial positions:

$$\bar{P}(R,t) = \int \rho(r_0)\, P(r_0, r+R, t)\, dr_0 \qquad (2.13)$$

where $\rho(r_0)$ is the molecular density. An analogous relationship between the probability of finding a particle with a specific displacement after a particular time interval and the evolution of concentration of particles [66] could be established by rewriting Fick's second law:

$$\frac{\partial P(r_0,r,t)}{\partial t} = D\nabla^2 P(r_0,r,t) \qquad (2.14)$$

Since the architecture of the tissue microstructure can indirectly be probed by looking at the behaviour of water molecules' displacement, the characterization of the diffusion propagator (and in particular the use of diffusion MRI) is of great importance.

In the next section the techniques used to characterize diffusion will be described, as well as the considerations that must keep in mind to fully take advantage of the power of diffusion imaging to probe microstructure.

2.3.2 Pulsed Gradient Spin Echo (PGSE) Sequence

Diffusion-weighted magnetic resonance imaging (dMRI) was designed to sensitize the MRI signal intensity to the amount of water diffusion, as was firstly described by Le Bihan *et al.* (1986) [67]. This technique allows the *in vivo* and non-invasive imaging of the diffusion process of the water in the brain tissue.

The most common sequence used for dMRI is the pulsed gradient spin echo (PGSE) [68], first introduced by Stejskal and Tanner (1965) [69]. This imaging sequence consists of a 90º RF dephasing pulse followed by a 180º refocussing pulse. Equal diffusion-encoding gradients are applied on either side of the 180º pulse in each of the *x*, *y* and *z* directions. Therefore as water molecules move in the direction of the gradient, their spins acquire phase shifts, proportional to their displacement, and there is a loss of signal. Stationary spins do not acquire a phase shift so there would be no loss of signal, which will provide contrast in dMRI.

For the PGSE sequence, the amount of diffusion and therefore dephasing of the signal is influenced by parameters that can be codified in term of *q-values* and diffusion times, or with an index denoted the *b-value*. The *b-value* reflects the degree of diffusion weighting applied, which could be conceptualize by the equation

$$q = \frac{1}{2\pi}\gamma\delta G \qquad (2.15)$$

$$b = \gamma^2 G^2 \delta^2 (\Delta - \delta/3) \qquad (2.16)$$

where γ is a physical constant known as the gyromagnetic ratio, G is the amplitude of the diffusion gradient typically measured in mT/m, δ is the duration of each diffusion gradient in ms. The diffusion time Δ is the interval between the onset of the diffusion gradient before the refocusing pulse and that after the refocusing pulse, measured in ms (see **Figure 2.10**), i.e. the time during which water molecules are "free" to explore tissue microstructure, corrected by a small factor ($\delta/3$) that accounts for the fact of the gradients having a finite duration. The units of *b-value* are s/mm^2. [69,70]

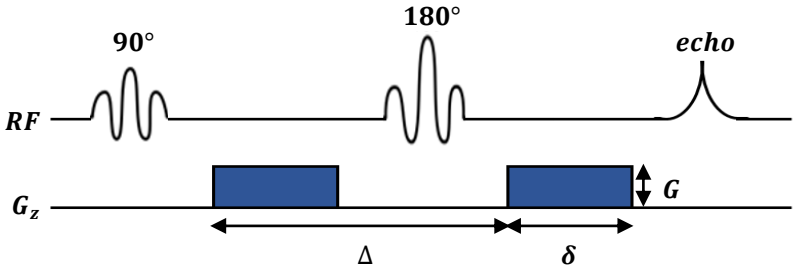

Figure 2.10 | Pulse sequence diagram for a diffusion-weighted acquisition shows that two diffusion sensitizing gradients (blue) are added to a spin-echo sequence, one before and one after the 180° refocusing pulse. The diffusion-weighting factor *b* depends on the amplitude of the diffusion gradient (G), the duration of each diffusion gradient (δ), and the interval between the onset of the diffusion gradient before the refocusing pulse and that following the refocusing pulse (Δ). *RF* indicates radio-frequency pulses; G_z, gradient pulses. Adapted from [70].

dMRI is an MRI technique where the signal intensity in a voxel is determined by the amount of diffusion in it, described mathematically by an apparent diffusion coefficient (ADC) which is a scalar value that reflects the interaction of molecules with the microstructure. To quantify diffusion, a minimum of two signal measurements (with different *b-value*) are needed: one with diffusion weighting (S) and one without diffusion weighting (S_0), which are related according to:

$$S = S_0 e^{(-bD)} \qquad (2.17)$$

where b is the diffusion weighting factor (defined above), and D is the ADC which values could be calculated using the equation:

$$ADC = -\frac{ln(S_1/S_0)}{b_1 - b_0} \qquad (2.18)$$

where S_0 and S_1 are signal intensities obtained with $b_0 = 0\ s/mm^2$ and $b_1 = 1000\ s/mm^2$, respectively. An ADC of a tissue is expressed in units of mm^2/s. [69, 71, 72]

Overall the magnitude of the diffusion-weighted signal depends on two factors: (1) the three-dimensional angular orientation in which the diffusion gradients are applied during image acquisition, and (2) the strength of diffusion weighting applied, as parameterized by the *b-value* for the acquisition. [73] According to Jones (2009) [74], it could be also concluded that, in tissues where diffusion is isotropic (such as CSF) there will be phase shifts in each of the three gradient directions resulting in signal loss, so they will appear dark on dMRI. The diffusion in each voxel can therefore be sufficiently described by a large ADC. In voxels containing WM, where diffusion is anisotropic, there will not be equal phase shifts in all directions, so the ADC (and appearance on dMRI) will depend on the direction in which it is measured.

2.4 Diffusion Tensor Imaging

While in a single direction diffusion may be simply explained using a scalar parameter D, in order to characterize anisotropy, and in particular to describe molecular mobility along different directions, a tensor should be used. Diffusion Tensor Imaging (DTI) was able to overcome this limitation, by providing estimation for the average diffusion or the degree of anisotropy in each voxel, as well as the main direction of diffusivities in each voxel and the diffusion values associated with these directions (Basser *et al.*, 1994) [75]. The expression for the obtained signal is given by:

$$ln\ \frac{S}{S_0} = -\sum_i^3 \sum_j^3 b_{ij} D_{ij} \qquad (2.19)$$

where b_{ij} is the *b-matrix* and D_{ij} is the Diffusion Tensor (DT), which is a 3x3 symmetrical matrix applied to dMRI data allowing the direction of greatest diffusivity to be described in 3D. The *b-matrix* is calculated from the combination of the applied gradient vectors and the defined *b-value*, and it requires only 6 non-colinear different gradient directions to compute the diffusion tensor, along with the non-diffusion (S_0) image. [75, 76]

This DT is commonly used to characterize diffusion in brain tissue, where water displacement per unit is unlikely to be equal in all directions. It can be conceptualised as an ellipsoid of which the long axis represents the direction with the highest diffusivity. As it can be obtained from the Single Value Decomposition (SVD) of DT matrix, the magnitude of its direction is called the major eigenvalue (λ_1) and its direction called the major eigenvector. Perpendicular to the major eigenvector are the two short axes: the median and minimum eigenvectors, with their eigenvalues λ_2 and λ_3 (see **Figure 2.11**). [62]

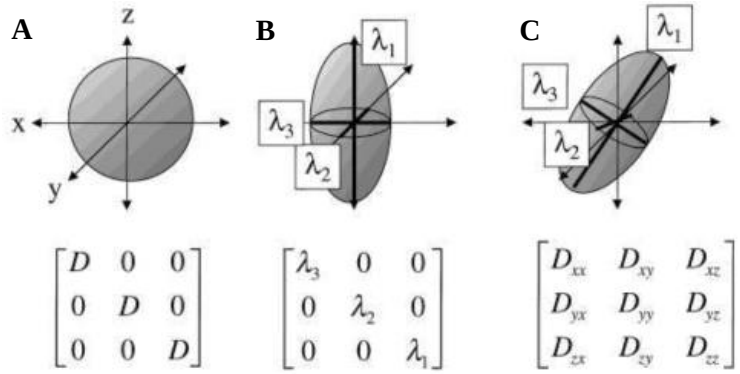

Figure 2.11 | Relationship between diffusion ellipsoid (first row) and diffusion tensor (second row). **(A)** In an isotropic medium, the diffusion is equal in all directions. The diffusion ellipsoid of this system is spherical and can be depicted by one diffusion constant D. **(B, C)** In an anisotropic medium the diffusion along one direction, termed the principal eigenvalue (λ_1), is greater than the other two eigenvalues (λ_2 and λ_3). To fully characterize such a system, 3 × 3 tensor is needed and the values of the nine elements depend on the orientation and the principal axes. Adapted from [62].

From the DT, several useful parameters can be extracted (Basser, 1995) [77]. In particular, various measures of the anisotropic or orientation dependence of diffusion have been proposed, such as fractional anisotropy (FA) and mean diffusivity (MD).

Fractional anisotropy is a quantitative measure that describes the degree of anisotropic diffusion. FA ranges from 0 to 1, with a value of 0 indicating perfectly isotropic diffusion and a value approaching 1 indicating pure anisotropic diffusion. Low values of FA are typically observed within CSF, whereas high values of FA are found in highly organized WM.

$$FA = \sqrt{\frac{1}{2}}\sqrt{\frac{(\lambda_1+\lambda_2)^2+(\lambda_2+\lambda_3)^2+(\lambda_3+\lambda_1)^2}{\lambda_1^2+\lambda_2^2+\lambda_3^2}} \qquad (2.20)$$

Mean diffusivity, on the other hand, describes the overall diffusion in units of mm^2/s. In contrast to FA, the values of MD are high in regions of unrestricted diffusion (such as CSF) and lower in regions of restricted diffusion (such as WM).

$$MD = \frac{\lambda_1+\lambda_2+\lambda_3}{3} \qquad (2.21)$$

Therefore, many previous studies such as the ones performed by Feldman *et al.* (2010) [8], Pannek *et al.* (2013) [78] or Yoshida *et al.* (2013) [79], allowed to conclude that increased FA and decreased MD are typically associated with higher organization, (pre-) myelination and decreased water content

(see **Figure 2.12**). FA is highly sensitive to microstructural changes but it is less specific to the type of change, whereas MD is sensitive to cellularity, oedema and necrosis.

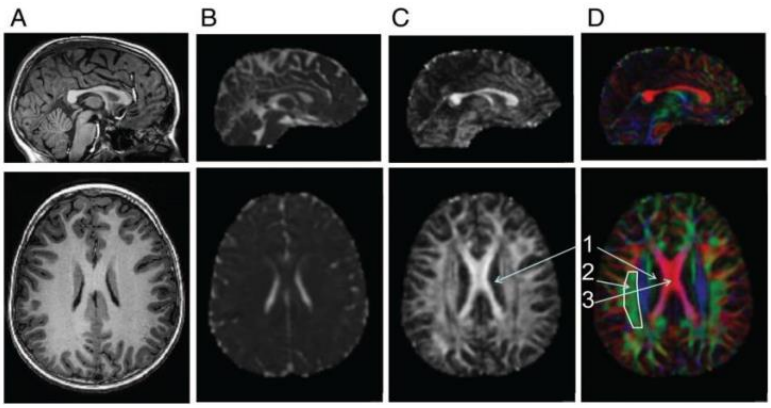

Figure 2.12 | Sagittal (top) and axial (bottom) slices from a healthy 12-year-old girl. **(A)** Conventional T_1 weighted anatomical image. **(B)** Mean Diffusivity (MD) map calculated from Diffusion Tensor Imaging (DTI) data. High signal (white areas) represents high diffusion; low signal (gradations of dark areas) represents reduced diffusion. **(C)** Fractional Anisotropy (FA) map calculated from DTI data. High signal (white areas) represents high FA; low signal (dark areas) represents reduced anisotropy. **(D)** Red-Green-Blue map calculated from DTI data. Voxels displayed as red represent tracts with primarily left-right orientation (*x*-axis); voxels displayed as green represent tracts with primarily anterior-posterior orientation (*y*-axis); voxels displayed as blue represent tracts with primarily superior-inferior orientation (*z*-axis). The superior longitudinal fasciculus, a tract containing fibres projecting along the *y*-axis (outlined in white) is represented in green. The corpus callosum, a tract containing fibres projecting along the *x*-axis, is represented in red. From [8].

In recent years, DTI, based on DT model, has emerged as a method to noninvasively measure WM microstructure *in vivo* throughout the life span, beyond structural size assessed using T_1- and T_2 -weighted MRI. It has been widely used to investigate changes in WM at different stages of brain development as well as their relationship to different pathological conditions. [67]

The measurement of MRI signal in a diffusion experiment is not related to a single spin, but rather to a spin population, which leads us to measure the PDF of water molecules' displacement or diffusion propagator (Callaghan *et al.*, 1990) [80]. In the regime of large displacements and short *q-values*, the propagator may be described using a Gaussian distribution (Basser, 2002) [81]. Nevertheless, in the presence of cell barriers or restrictions such as regions with crossing fibres, DTI is no longer capable of reflecting the index of anisotropic diffusion and fibre orientation, since the behaviour of water molecules is no longer Gaussian for high *q-values*.

In the next section, moving beyond the DTI model, High-Angular-Resolution Diffusion Imaging techniques will be introduced and the reconstruction methods associated discussed, as well as metrics that can be extracted and related with microstructural properties.

2.5 High Angular Resolution Diffusion Imaging

Given the acquired diffusion signal, deciding how to translate it to biophysical information is based on the choice of reconstruction method of the diffusion propagator. There are different approaches to reconstruct the propagator, each one having advantages and disadvantages, but most of them rely on high angular resolution diffusion imaging (HARDI) acquisitions ((Frank, 2001) [82]; (Tuch *et al.*, 2002) [83]; (Tuch, Reese *et al.*, 2002) [84]).

Addressing the limitation of DT model, HARDI is capable of discriminating multiple fibre populations crossing within the same voxel, through the exploration of the anisotropy of the diffusion signal by employing many directions on a sphere with a single (single shell) or multiple diffusion weightings (multi-shell). As procedures provided through the natural extension of the single-fibre case, they require the acquisition of data with a large number of different gradient directions applied on a

sphere, but with a much larger angular resolution (Le Bihan *et al.*, 2001) [85]. The generated shape of the surface (for a single voxel) is composed with different measured diffusion directions, which can be divided into small components (tessellations), similar to icosahedrons. The possibility of explicitly defining this spacing is achieved, and consequently the number of directions, which corresponded to the vertices of the tessellations, could be also defined. This idea leads to a very simple and practical method for the identification of diffusion anisotropy without the necessity of invoking the DT formalism and storing large files.

Numerous methods exist to reconstruct the architecture of brain tissue from HARDI data. All methods have in common the ability to provide the orientation of multiple WM tracts within each voxel. HARDI methods allow the estimation of more than one fibre population within a voxel, whereas DTI not because it assumes a Gaussian distribution for the behaviour of the displacement of water molecules. [84, 83]

With this in mind, over the next subsections there will be discussed two types of HARDI methods: model-free approaches, if we try to get a three dimensional displacement probability profile from data directly, collecting an Orientation Density Function (ODF); or, on the other hand, model-based approaches, if we try to apply a model to our data and extract a Fibre Orientation Distribution (FOD).

2.5.1 Model free approaches

With the rapid evolution of dMRI methods, the literature now contains a wide variety of model-free based techniques, which allow to provide a more precise and efficient description of complex tissue structures. Based on the achievements accomplished by Callaghan *et al.* (1988) [86], as tissue microstructure influences water particles mobility, it is possible to determine the PDF, which in its turn tells information about the material microstructure. Since the PDF gives us information about the distribution of water molecules displacement, it will peak in the preferential direction of fibres, elucidating us regarding their orientation.

By using model free approaches we are able to retrieve the diffusion propagator either by transforming the diffusion signal directly or by extracting a set of coefficients that better fit a mathematical representation of choice.

In this section, we do not attempt to provide a complete review of the existing techniques, but rather aim to introduce the basic concepts behind one of the most recent mathematical representations that could be computed based on the principles defined by this approaches, establishing its benefits and limitations.

2.5.1.1 Mathematical representations

Some descriptors of the underlying diffusion propagator can be defined using the transformation of the diffusion signal. However, the same could be achieved through its representation using some mathematical functions, which can yield a continuous description of the signal. In this kind of approaches, the diffusion signal is fitted to a linear combination of continuous functions from a set of discrete measures and, consequently, analytical relations can be drawn to explore the diffusion propagator (Merlet *et al.*, 2011) [87]. The main idea behind this is that for each direction the signal can approximated described by a series expansion of an orthonormal basis that simultaneously characterises the angular profile of the signal and its radial decay. It was also proved that the angular profile of the diffusion signal can be modelled using the Spherical Harmonic basis, as it enables a characterization of any spherical function analogous to a Fourier decomposition on the sphere (Frank, 2002) [88]. The signal $E(q)$ can be then represented as:

$$E(q) = \sum_{n=0}^{N} \sum_{l=0}^{L} \sum_{m=-l}^{l} c_{nlm} R_n(\|q\|) Y_l^m(u) \qquad (2.22)$$

where c_{nlm} are the coefficients, and R_n the basis functions of n radial order that we want to fit to the diffusion decay, and Y_l^m the spherical harmonics of l and m angular order and degree, respectively. In order to just attend to the modulus of the complex diffusion MR signal, real and even Spherical harmonics could be used, which are given by the following mathematical expression:

$$Y_l^m(\theta,\phi) \begin{cases} \sqrt{\frac{2(2l+1)(l-m)!}{(l-m)!} P_l^m(\cos\theta)\cos(m\phi)} & , \ m < 0 \\ \sqrt{(2l+1)P_l^m(\cos\theta)} & , \ m = 0 \\ \sqrt{\frac{2(2l+1)(l-m)!}{(l-m)!} P_l^m(\cos\theta)\sin(m\phi)} & , \ m > 0 \end{cases} \qquad (2.23)$$

where P_l^m are the associated Legendre polynomials. The radial and angular orders are usually truncated at a maximum value of *N* and *L* respectively, and they are related to the number of samples acquired. These orders are chosen so that the resulting number of coefficients are at least half of the number of measurements, with the choice of *N* and *L* depending on what aims to be observed (Assemlal *et al.*, 2009) [89].

The description of the radial decay of the diffusion signal is still an open field of research, but in essence it depends on using a R_n basis functions that incorporate particular mathematical functions capable of characterizing the signal decay.

2.5.1.1.1 Simple Harmonic Oscillation based Reconstruction and Estimation

This approach defined by Özarslan *et al.* (2008) [90] and named Simple Harmonic Oscillation based Reconstruction and Estimation (SHORE) was applied to characterize the diffusion signal decay in 1D, where a decomposition based on a complete orthogonal basis was achieved; with the diffusion signal, obtained from a 1D acquisition, described by:

$$R_n(\|q\|) = i^n (2^n\, n!)^{-\frac{1}{2}} e^{-2\pi^2 q^2 u^2} H_n(2\pi q) \qquad (2.24)$$

where H_n are the *n-th* order Hermite polynomial and u is the scaling function to be determined. This basis has an adequate behaviour as q approaches infinity and also enables to characterize the non-monotonical radial decay as it is the case for the signature signal coming from restriction.

In order to represent the measured diffusion signal in 3D, this approach was later expanded using the Spherical Harmonics basis and Laguerre polynomials, through the application of a scale parameter ζ, defined as $\zeta = \frac{1}{8\pi^2 \Delta D}$, to adapt to different diffusivity profiles, where Δ and *D* represent the diffusion time and the diffusivity, respectively.

Depending if the scale parameter is applied isotropically or anisotropically in all directions, the technique is named 3D-SHORE or Mean Apparent Propagator (MAP) – MRI (Özarslan *et al.*, 2013) [91].

Based on a more general description of 3D-SHORE using a tensorial scale parameter, MAP-MRI is a powerful analytical framework that efficiently measures the PDF of spin displacement and quantifies useful metrics of this PDF indicative of diffusion in complex microstructure (e.g., restrictions, multiple compartments), allowing the characterization of novel features of diffusion anisotropy and the non-Gaussian character of the three-dimensional diffusion process. Consequently, from MAP-MRI we can extract some of the most traditionally used metrics to describe the propagator which were originally developed from *q-space* imaging analysis. These *q-space* indices are scalar quantities estimated as analytic integrals of the diffusion signal and Ensemble Average Propagator (EAP), which values can be

linked to tissue microstructure such as the axonal diameter, but only when we assume that the diffusion signal originates from inside an ensemble of parallel cylinders with no extra-axonal space (see **Figure 2.13**). [92, 93]

One of these metrics is the Mean Squared Displacement (MSD) of the molecules in each voxel, which is related to the full width half maximum of the PDF. Consequently, MSD is defined as a sensitive biomarker to detect pathologic changes in WM, with the ability of characterize the cell mobility. Another metric probes the restriction of the specific microstructure environment by quantifying the maximum probability of water molecules undergoing zero displacement (P0).

The zero displacement probability metric has also been referred to return to origin probability (RTOP); it is calculated as the integral of the signal attenuation function over the entire *q-space* or the EAP in zero, and can be seen as a reciprocal value of the mean pore volume. [91] So, this metric is par excellence used to characterize cellularity and restrictions in diffusion. Directions in which diffusion is mostly restricted will be associated with lower diffusivity values; in these regions, considering coherently organized WM, a return to axis probability (RTAP) can be defined as the integral of the signal in the plane passing through the origin and perpendicular to the main diffusion direction. This metric shows the contrast between single-fibre WM and regions with crossing fibres. [92] Additionally, RTAP can also be defined as reciprocal mean cross sectional area, from which certain studies have tried to infer axon diameters. [94] Complementary to RTAP, a return to plane probability (RTPP) can also be defined, in this case as the integral of the signal when the *q-vector* is parallel to the expected fibre orientation. [91] RTPP provides information about the complexity of WM, presenting higher values in regions containing several fibre orientations as opposed to regions with coherent fibre pathways.

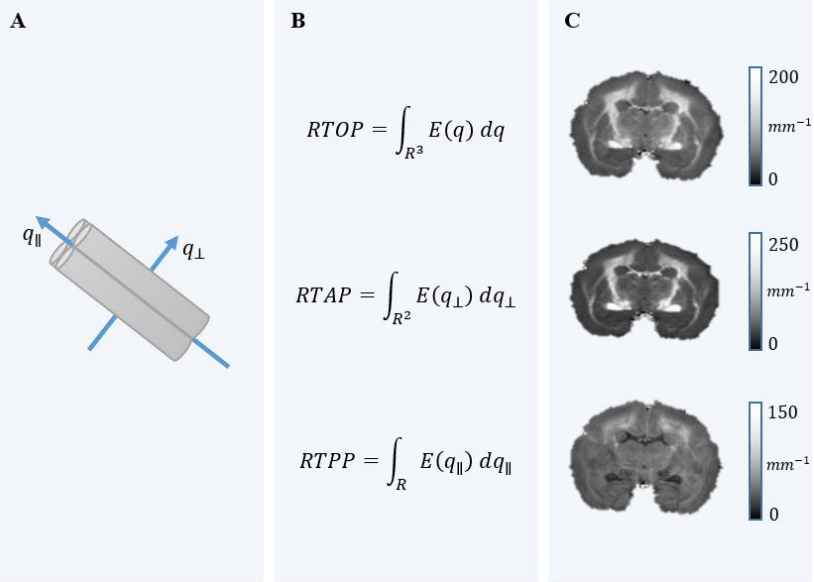

Figure 2.13 | (A) Pictorial representation of coherent white matter pathways, assumption used in the calculation of some propagator metrics. **(B)** Global propagator metrics, calculated directly from the diffusion signal, namely return to origin probability (RTOP), a return to axis probability (RTAP), and return to plane probability (RTPP). **(C)** MAP-MRI-derived parameter (cube-root of RTOP, square root of RTAP, and RTPP) coronal maps of marmoset brain. Adapted from [91].

2.5.2 Model based approaches

In the previous subsection, HARDI techniques were based on extracting the orientation distribution function from the data rather than providing insight about the actual fibre orientations.

On the other hand, model based approaches assume particular biological features of the tissue being imaged and reconstruct the diffusion propagator having that in mind, providing more directly interpretable measures of the contents and organization of microstructure, without capturing the full complexity of the microstructure underpinning the generation of the diffusion signal. [95, 96, 97] Therefore, and as described by Frank (2002) [88], model-based approaches could be based on the assumption of looking for multiple fibres per voxel as a mixture of diffusion tensors. This assumption affirms that the signal that came from a single voxel could be extended from a concept of single fibre. Furthermore, it was considered that there was no exchange between fibres yielding independent signals per fibres, and summing all contributions together to get the final intensity.

Some specific cases of model-based approaches will be explored in the next two subsections, namely Spherical Deconvolution and Neurite Orientation Dispersion and Density Imaging (NODDI).

2.5.2.1 Spherical Deconvolution

As seen in the previous section, one limitation of DTI is that it only describes one principal direction of fibres for each voxel so it does not take into account voxels that contain crossing fibres. There have been many techniques developed attempting to overcome this problem as has been seen, however one of the most successful has been spherical deconvolution. This method can be used to estimate the distribution of fibre orientations present within each imaging voxel (Tournier *et al.*, 2004) [98].

With this technique, the diffusion-weighted signal attenuation that would be measured from a single coherently oriented fibre population, during a HARDI session, can be represented by an axially symmetric response function $R(\theta)$, where θ is the elevation angle in spherical coordinates. The signal $S(\theta, \phi)$ can be expressed as the convolution over the unit sphere of the response function $R(\theta)$ with a fibre ODF $F(\theta, \phi)$, where ϕ is the azimuthal angle in spherical coordinates:

$$S(\theta, \phi) = F(\theta, \phi) \otimes R(\theta) \qquad (2.25)$$

The fibre ODF gives the fraction of fibres within the sample that are aligned along the direction (θ, ϕ), expressed in spherical coordinates. Mathematically, the fibre ODF represents the probability distribution on the sphere, as each point on the sphere corresponds to a unique orientation.

If the response function $R(\theta)$ is known *a priori*, then the fibre ODF $F(\theta, \phi)$ can be obtained by performing the spherical deconvolution of $R(\theta)$ from $S(\theta, \phi)$.

The spherical deconvolution method can reconstruct the original fibre ODF adequately, without the need to impose any *a priori* information about the likely number of fibre populations present.

With this methodology, different levels of anisotropy can be interpreted not only as the presence of different mixture of fibre orientations, but more physically also as partial volume from isotropic components. This means that in the presence of isotropic components the algorithm leads to physically meaningless spurious spikes. Consequently, it can be used a threshold on FA maps to exclude GM or CSF voxels (isotropic partial volume), however this is not viable when considering regions with low anisotropy due to highly complicated fibre orientations. [99] Nonetheless, it is important to highlight that this limitation could be overcome through the knowledge of information regarding the microstructure, which could be extremely useful in order to characterize multiple WM pathways based on the values assumed by specific diffusion metrics, as well as to be able to analyse global metrics either at voxel level or along each fibre´s trajectory.

On the other hand, deconvolution methods are very sensitive to noise effects, but the robustness of the operation can be greatly enhanced by a non-negativity constraint. This technique is known as constrained spherical deconvolution (CSD). CSD provides an estimate of FOD that is robust to noise while being able to resolve multiple orientations of fibres in a voxel. This is possible by assuming the signal from a WM fibre can be described by a single response function (Tournier *et al.*, 2007) [100]. The response function can be estimated directly from the data by measuring the diffusion-weighted signal profile in regions likely to contain a single coherently oriented fibre population.

It is important to note that, although the DT model could be used to estimate the response function, one advantage of the present method is that it does not rely on any particular model of diffusion. CSD may prove most useful in the field of tractography, where the improved characterization of the fibre orientations is likely to make tracking through regions contaminated with partial volume effects much more reliable.

2.5.2.2 Neurite Orientation Dispersion and Density Imaging

Neurite orientation dispersion and density imaging (NODDI) is a practical diffusion MRI technique for estimating the microstructural complexity of WM *in vivo* on clinical MRI scanners (Zhang *et al.*, 2012) [97]. Quantifying neurite morphology in terms of its density and orientation distribution provides a window into the structural basis of brain function both in normal populations and in populations with brain disorders. An increase in the dispersion of neurite orientation distribution is associated with brain development, whereas a reduction in the dendritic density is linked with the aging of the brain.

NODDI adopts a tissue model that distinguishes three types of microstructural environments. Hence, the normalised signal A can be written as:

$$A = (1 - \nu_{iso})(\nu_{ic} A_{ic} + (1 - \nu_{ic})A_{ec}) + \nu_{iso} A_{iso} \qquad (2.26)$$

where A_{ic} and ν_{ic} are the normalized signal and volume fraction of the intra-cellular compartment (refers to the space bounded by the membrane of neurites); A_{ec} is the normalized signal of the extracellular compartment (refers to the space around the neurites, which is occupied by various types of glial cells and, additionally in GM, cell bodies); and, A_{iso} and ν_{iso} are the normalized signal and volume fraction of the free diffusion compartments (the space occupied by fluid). Each affects water diffusion within the environment in a unique way.

Based on its multi-compartment biophysical model of brain microstructure, NODDI can estimate properties of WM, such as orientation dispersion index (ODI) and neurite density index (NDI), corresponding to the degree of incoherence in fibre orientations and to the intracellular volume fraction, respectively, within each imaging voxel (Tournier *et al.*, 2007) [100].

The ODI is defined to characterize angular variation of neurites, such as:

$$ODI = \frac{2}{\pi} \arctan\left(\frac{1}{\kappa}\right) \quad , \; 0 \leq ODI \leq 1 \qquad (2.27)$$

where κ is the concentration parameter of Watson distribution. The Watson distribution is the simplest orientation distribution that can capture the dispersion in orientations.

The parameter maps from the NODDI model exhibit a spatial pattern of tissue distribution that is in concordance with the known brain anatomy. The map of NDI shows the expected pattern of neurite density by assuming the lower values in GM than in WM, with the highest values being taken in the major WM tracts, such as the corpus callosum. On the other hand and as expected, ODI demonstrates to be higher in GM than in WM, which justifies that the lowest values are reached in the corpus callosum. The sensitivity of FA to ODI can be seen most clearly from examining the WM, where FA shows a

strong negative correlation to ODI and it exhibits a weaker positive correlation to NDI. To visualize the specific dependency of FA on NDI and ODI, **Figure 2.14** illustrates the relationship between ODI and NDI among the voxels with similar FA values. The figure confirms that a particular value of FA in tissue can be achieved by different combinations of NDI and ODI. Furthermore, it reveals a sensible positive correlation between the two microstructural parameters, i.e., two voxels can have the same FA value as long as the one with the larger value of NDI also has the larger ODI. Moreover, a small change in ODI needs to be compensated with a much larger change in NDI. [97]

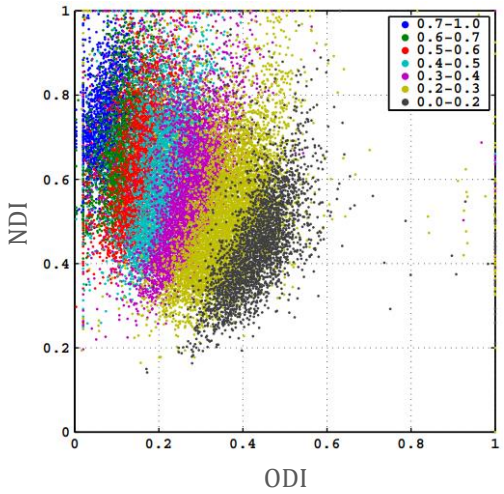

Figure 2.14 | Scatterplots of neurite density index (NDI) *vs* orientation dispersion index (ODI) for white matter. To assess the relationship between NDI and ODI for the voxels with similar FA values, we stratify the voxels into smaller groups each of which has their fractional anisotropy (FA) values falling between a narrow ranges specified in the legend. Adapted from [97].

However, despite its rapid adoption in neuroimaging, it is extremely important to be aware of NODDI's limitations [97, 101]. First, the NODDI tissue model currently parametrizes the neurite orientation distribution with Watson distribution. This has limited accuracy in modeling orientation distributions that are not cylindrically symmetric (such as in the regions with fanning or crossing axons), since the orientation distribution of neurites is modelled by constraining the dispersion about the dominant orientation as isotropic. Second, NODDI relies on a representation with a single WM fascicle while fascicles with various microstructures have been observed, such as in the body of the corpus callosum. Consequently, this model ignores the intra-axonal radial diffusivity and, similarly to the DTI model, considers only a single fascicle compartment per voxel while fascicles crossings occur a lot in the human brain. NODDI may capture crossing fascicles as increased dispersion but cannot characterize each of them separately. Furthermore, due to its much more complex mathematical formulation compared to DTI, the computational time is higher even if it has a relatively low number of parameters to estimate.

2.5.2.2.1 Accelerated Microstructure Imaging via Convex Optimization

With the aim of improve the burdensome fitting time required by the existing microstructure imaging techniques in diffusion, Accelerated Microstructure Imaging via Convex Optimization (AMICO) framework (Daducci *et al.*, 2015) [102] was introduced based on the reformulation of these models as simple linear systems that can be solved very efficiently using convex optimization, which thus enable a drastic reduction in the computation time by orders of magnitude, while still preserving the accuracy and robustness of the estimated parameters.

According to the principles of AMICO, the microstructural properties of the tissue can be expressed as a system of linear equations:

$$y = \Phi_N\, x + \eta \qquad (2.28)$$

where y is the vector containing the dMRI signal acquired at each voxel, η accounts for the acquisition noise, Φ_N is the linear operator, also called dictionary, that relates the microstructure properties in study (fibre density and orientation dispersion) with the measurements, and x represents the microstructure properties contributions.

In order to linearize the NODDI model, defined by Zhang *et al.* (2012) [97], the dictionary is divided into the following two blocks:

$$\Phi_N = \left[\Phi_N^t \mid \Phi_N^i\right] \qquad (2.29)$$

in which the signal attenuation that arises from a micro-environment characterized by specific axon density and dispersion is represented by Φ_N^t, and Φ_N^i comprises the isotropic contributions.

In order to know how much each micro-environment contributes to y, AMICO uses DTI to obtain the main direction of the fibres at each voxel, and calculate the values of fibre density and orientation dispersion that compose the dictionary. Then, the contributions given by each combination for a specific density and dispersion are computed in order to minimise $y - \Phi_N\, x$.

The parameters generated by the NODDI model are the intracellular volume fraction (ICVF), the isotropic volume fraction (ISOVF) and the orientation dispersion (OD); which can be computed for each voxel as:

$$v_{ic} = \frac{\sum_{j=1}^{N_t} f_j\, x_j^t}{\sum_{j=1}^{N_t} x_j^t} \qquad (2.30)$$

$$v_{iso} = \sum_{j=1}^{N_t} x_j^i \qquad (2.31)$$

$$\kappa = \frac{\sum_{j=1}^{N_t} k_j\, x_j^t}{\sum_{j=1}^{N_t} x_j^t} \qquad (2.32)$$

where, for $j \in \{1, \ldots, Nt\}$, f_j represents the ICVF, and k_j the concentration parameter of Watson distribution (κ) at the *j-th* position of Φ_N^t.

Although this is still an open field of research, AMICO has already proved its availability as an ultrafast framework that by fitting specific models as NODDI will help to accelerate the spread of microstructure imaging to larger cohorts of patients and to study a wider spectrum of neurological disorders.

2.6 Tractography

In dMRI we are interested in studying tissue microstructure and infer about the underlying cytoarchitecture. Knowledge of the anatomy of WM connections is crucial to the understanding of normal and abnormal brain function. By reconstructing the fibre orientations from the diffusion profile (by any diffusion weighting technique that allows us a voxel estimation of the diffusion profile) it is possible to generate a three-dimensional image that follows trajectory of fibres throughout the brain – tractography (Mori *et al.*, 1999) [103]. Tractography is the only tool we currently have that allows us to visualise WM trajectories *in vivo* and noninvasively. This technique is used to identify and visualize a continuous three-dimensional trajectory by sequentially piecing together the estimates of fibre orientation from the directionality of individual voxels. Mathematically, the set of local fibre orientations can be considered as a three-dimensional vector field and the global fibre trajectories as its

streamlines. A streamline is designed to any curve that along its trajectory is tangent to the vector field and that can be represented as a three-dimensional space curve. [70, 104]

There are also several tractography algorithms that can be used, which can be split into two major classes: deterministic and probabilistic tractography algorithms.

The general principle of deterministic tractography algorithms (see **Figure 2.15 (A)**) is to use the directional information described by the DT from voxel to voxel. The most common directional assignment corresponds to the major eigenvector of the DT. By assuming a unique fibre orientation estimated in each voxel, a deterministic tractogram is generated by starting from one or more "seed" locations, typically within WM, and propagating the trajectories according to the tractography algorithm until the tracts are terminated. Specific constraints may be placed on the tractography algorithm to determine whether or not the result is consistent with predicted connectivity patterns. A significant limitation of deterministic tractography methods is the lack of information they provide regarding the error in the tracking procedure in any given experiment. Without this knowledge, it is not possible to know how much confidence we should have in the observed results. [105, 106, 107]

Probabilistic tractography methods (see **Figure 2.15 (B)**) attempt to overcome this limitation by explicit characterization of the confidence with which connections may be established through the diffusion MRI dataset. In this order, for probabilistic tractography, the tensor is visualized as a mathematical representation of the probabilistic distribution of fibre directions. Consequently, the next water molecule's direction is obtained by running a stochastic procedure which will draw a sample direction from this distribution. For each direction, the chance of it being selected is in proportion to its magnitude in the probabilistic distribution, and this direction is accepted if it satisfies the condition of shape constraints. [105, 106, 107]

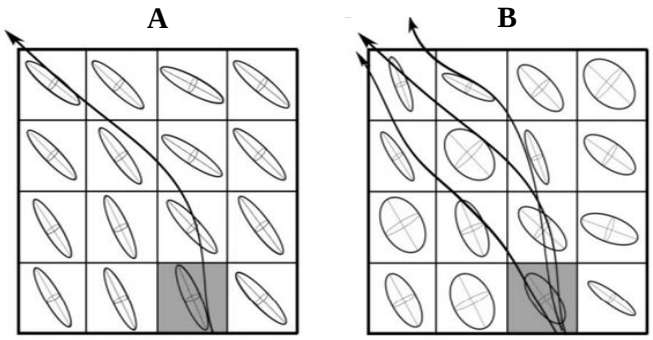

Figure 2.15 | Visual representation of the differences between deterministic **(A)** and probabilistic **(B)** approaches to tractography. Probabilistic approaches are considerably more extensive and computationally demanding, as they track all orientations in all voxels adjacent to the seed point (grey square). Adapted from [107].

However, it is worth reminding that both of these tractography algorithms share common points while generating the tracks: the reconstruction is terminated if the front of a streamline enters a region where the FA is below the established threshold; and, the same happens if the maximum angle that is taken between voxels is higher than the predefined angle. [105]

In general, the streamline approaches described previously are the prime example of local tractography algorithms. Tracking is performed in small successive integration steps by following the local fibre orientations that have previously been extracted. Although these type of methods could be characterized by its fastness, being therefore widely used, they have important drawbacks. The most apparent is associated to minor errors in the local fibre orientations, which can accumulate and significantly affect the final result. Another is related to the fact that resulting fibre tracks have little to no quantitative or biological meaning, since the streamline tractograms are typically a very poor predictor of the dMRI data that was actually measured. [70, 104]

On the other hand, global methods try to reconstruct all tracks simultaneously by finding the configuration that best describes the measured dMRI data. In general, global tracking promises a better stability with respect to noise and imaging artefacts and a better agreement with the actual dMRI data that was acquired. The main problem related to these methods is that they rely on stochastic optimization procedures, which consequently do not guarantee the convergence to a globally optimal solution. Furthermore, the application of these tracking approaches requires *prior* knowledge about the expected properties of the trajectories. However, the arbitrariness associated to the process of defining *prior* knowledge is a problem, which can leads to inconsistencies with the actual data, potentially resulting in non-existent fibre trajectories, or on the other hand, fibre tracks that perfectly match the underlying data, but that make little sense anatomically. [104, 108]

In summary, throughout the years we have seem incredible developments in tractography, which has become the method of choice to investigate quantitative MRI parameters in specific bundles of WM, however we are still far from knowing everything about the human brain and how this technique can help. Despite its unique abilities and exciting applications, fibre tracking is not without controversy, in particular when it comes to interpretation of its results. The only possible certainty that we have about tractography is that it is an extremely useful technique not only to localize tracts on an individual but also to register them into an atlas, to understanding, or perhaps even predicting, dysfunction caused by (structural) disconnections in specific locations (Catani *et al.*, 2007) [14] or even to study structural connectivity (Dell'acqua & Catani, 2012) [109]. Furthermore, there are still several problems that can be addressed such as finding the exact termination to connections in the boundary between WM and GM (causing false negatives, in which tracking can terminate prematurely, or false positives, in which tracking can switch to an unrelated adjacent tract), tracking the horizontal intra-cortical connections, or detecting synapses. [104, 110]

3 Subjects & Data Acquisition

This chapter begins with a description of the data that was used during the project, followed by a discussion on how the data was obtained and processed.

According to the principles settled in the Research Governance Framework for Health and Social Care, an approval has been issued on behalf of Great Ormond Street Hospital (GOSH) for Children National Health Service (NHS) Trust for this study. The inclusion criteria for this study were images acquired in subjects with or less than nineteen years old. Eighteen controls and eighteen subjects with a diagnosis of TLE (pre-surgical images) with a broad range in age (see **Table 3.1**) were chosen from a larger initial sample of subjects.

Table 3.1 | Control group and patients with Temporal Lobe Epilepsy (TLE) characterisation according to gender. Age is given in years old (y.o.) with mean ± standard deviation and with the respective range.

	Control group	**Patients with TLE**
N	18	18
Gender	10 M / 8 F	12 M / 6 F
Age (y.o.) by gender	$[12 \pm 3]$ / $[12 \pm 2]$ [8 - 18] / [8 - 15]	$[12 \pm 5]$ / $[13 \pm 5]$ [3 - 19] / [5 - 19]
Age (y.o.) group total	12 ± 3 [8 – 18]	12 ± 5 [3 – 19]

All imaging data were collected as part of the clinical imaging protocol at Great Ormond Street Hospital (London, UK), acquired on a Siemens 3.0 T Prisma scanner (Siemens, Erlangen, Germany), equipped with a 20 channel head receive coil. The protocol included a multi-shell diffusion sequence employing a diffusion-weighted spin-echo single shot 2D EPI acquisition, with multi-band radio frequency pulses to accelerate volume coverage along the slice direction. [111, 112] A multi-band factor of 2 was used to image 66 slices of 2 mm thickness with 0.2 mm slice gap. Diffusion gradients were applied over two 'shells': b = 1000 s/mm^2 and b = 2200 s/mm^2, with 60 non-co-linear diffusion directions per shell, in addition to 13 interleaved b = 0 s/mm^2 (non-diffusion weighted) images. Other imaging parameters were: TR = 3050 ms, TE = 60 ms, FOV = 220×220 mm^2, *matrix size* = 110 × 110, *in-plane voxel resolution* = 2.0 mm, GRAPPA (*GeneRalized Autocalibrating Partial Parallel Acquisition*, which is a parallel imaging technique, based on *k-space* that can be used to shorten the acquisition time or increase the spatial resolution in the same examination time) factor 2, phase-encoding (PE) partial Fourier = 6/8. An additional b = 0 s/mm^2 acquisition was performed, with identical readout to the diffusion-weighted scan, but with the phase encode direction flipped by 180° (in the anterior-posterior direction), for correction of susceptibility-related artefacts. The total scan time for the multi-shell diffusion sequence (including the b = 0 s/mm^2 acquisition with flipped PE) was 7 min 50 s. In addition, a T_1-weighted 3D FLASH (*Fast Low Angle SHot*, which is a GE MRI-sequence that uses RF excitation pulses with a low flip angle (less than 90°) and subsequent reading gradient reversal for producing the signal) structural image was acquired using 176 contiguous sagittal slices, FOV = 256×240 mm^2 and 1×1×1 mm^3 image resolution; TE = 4.9 ms and TR = 11 ms.

Along the next four chapters, presented in a chronological order of the executed tasks, each of the analyses carried out will be depicted, beginning with a brief description about the methodologies regarding the tractography reconstructions and the extraction of multiple microstructural parameters of interest in this study. The outcome of the analyses described will be also summarized, followed by the discussion of the results obtained, putting them into context and highlighting their importance in light of other scientific studies.

With this in mind and knowing that the natural motion of water molecules in biological tissues is highly influenced by the microstructural environment, and the anisotropy of this random process in WM can be exploited to probe important features of the neuronal tissue, with three independent analyses of the diffusion dataset, we aim to:

- use the information about the diffusion process, based on diffusion tensor derived parameters and more advanced features from MAP-MRI and NODDI model, in order to gather information about the whole-brain architecture, or the microstructure of some specific WM pathways (as the arcuate fasciculus, the corticospinal tract, and the corpus callosum) reconstructed with tractography;
- analyse regions comprised by multiple fibre populations, which results in complex architecture configurations, in order to improve their characterization through the study of different components / WM tracts that cross it;
- use the information regarding the diffusion process to create signatures / models of specific WM tracts;
- study the microstructural and macrostructural changes in WM tracts of TLE patients in temporal and extratemporal WM tracts of both hemispheres;
- be able to apply the findings provide by the previous bullet points to identify pathological changes between groups.

4 Tractography Reconstructions & Microstructural Parameters Extraction

The data analysis of all thirty six subjects was performed on diffusion images that have been acquired previously to this study (see ***Chapter 3*** for more details) and pre-processed. Briefly, regarding the pre-processing methodology, the diffusion MRI data were denoised using MRtrix [113] (which provides a large suite of tools for image processing, analysis and visualisation, with a focus on the analysis of WM using diffusion-weighted MRI), followed by TOPUP and EDDY from FSL software [114] (which is a comprehensive library of analysis tools for dMRI brain imaging data), that were used to correct for susceptibility distortions and to perform motion and eddy current correction. For bias field corrections and skull stripping of structural scans, Freesurfer [115, 116] (which is a software package for the analysis and visualization of structural and functional neuroimaging data) was used to provide parcellation of cortical and subcortical structures based on a standard atlas.

With regard to the tractography protocols, a compulsory step in spherical deconvolution is deriving the response function, which is used as the kernel during the deconvolution step. Using MRtrix, this function was inferred directly from the image data by averaging the diffusion signal from a set of empirically-determined 'single-fibre' voxels in different tissues, such as WM, GM and CSF. In order to estimate that, the *dwi2response* command was applied using the *msmt_5tt* algorithm. By providing the tissue-segmented anatomical image (in the five-tissue-type (5TT) format) of each subject, which were previously generated using the *5ttgen* command, this response function's estimation algorithm was able to identify single-tissue voxels in the diffusion image based on the high-resolution tissue segmentations. [117] Briefly, this algorithm starts by resampling the 5TT segmented image to the diffusion image space. Then, for each of the three tissues (WM, GM, CSF), voxels with tissue partial volume fraction higher than 0.95 (default value) are selected, and GM and CSF are further constrained by an (upper) 0.2 (default value) FA threshold. This step allows us to derive a mask based on which will be selected single-fibre voxels for WM. Finally, the multi-shell response for each tissue type was derived since the diffusion images of this study were acquired as multi-shell data.

The output response functions will be the inputs for the *dwi2fod* command that estimates the FOD for each tissue, within a specified binary mask created using the BET tool from FSL software. This output mask is generated based on the deletion of non-brain tissue from an image of the whole head, using a fractional intensity threshold of 0.3. After this, to estimate the FODs, the multi-tissue CSD algorithm was used. This choice was based on its superior ability to reliably track fibres in areas containing crossing fibres. [100] After this, the *mtnormalise* command was applied, which was responsible for the multi-tissue informed log-domain intensity normalisation by performing the bias field correction via a third order polynomial.

MRtrix protocols, based on HARDI tractography, were designed to extract the arcuate fasciculus, corticospinal tract and corpus callosum. These WM pathways were chosen having in mind a complex region such as the centrum semiovale which contains fibre structures belonging to the arcuate fasciculus, corticospinal tract and corpus callosum. Our aim was to explore how different microstructural parameters change along these specific WM tracts and investigate the values assumed by each scalar map in the chosen region.

In order to reconstruct the WM tracts, ROIs were manually defined on each subjects' image. In this study, the accuracy of the ROI location is based on anatomical knowledge, and the width and height of the regions were chosen so they could take into account inter-subject variability.

Briefly, for the arcuate fasciculus, the first inclusion region was a one-slice thick volume delineated on the coronal view, at the level of the classical arcuate fasciculus ''bottleneck''. [118] This region is coded green on the eigenvector map (see **Figure 4.1**) – indicating an anterior-posterior orientation. The second inclusion region was delineated in the axial plane in the superior temporal gyrus, coded blue on the eigenvector maps (left-right direction). [10]

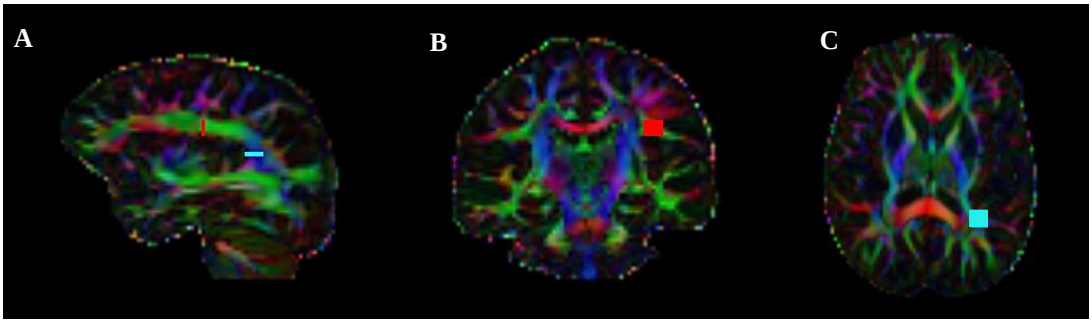

Figure 4.1 | (A) Location of inclusion ROIs for the arcuate fasciculus. Colours on each eigenvector map represent the main direction of WM tracts (red: left–right, blue: superior-inferior, green: anterior-posterior). **(B, C)** The first inclusion region is a one-slice thick volume coloured by red and positioned on the coronal view, and the second inclusion region was delineated on the axial plane using one-slice thick volume coloured by light-blue. See text for anatomical landmarks used.

To identify the corticospinal tract bundle, three one-slice ROIs were drawn on the axial view (see **Figure 4.2**) along this WM pathway (blue on the eigenvector map) at different levels following the inferior – superior direction, for left and right hemispheres. The first inclusion ROI was placed on the corticospinal tract portion of the pontomedullary junction (yellow square), and the following inclusion ROIs, on the corticospinal tract portion of the anterior mid-pons (magenta square) and on the posterior limbs of the internal capsules (light-blue square). [23, 119]

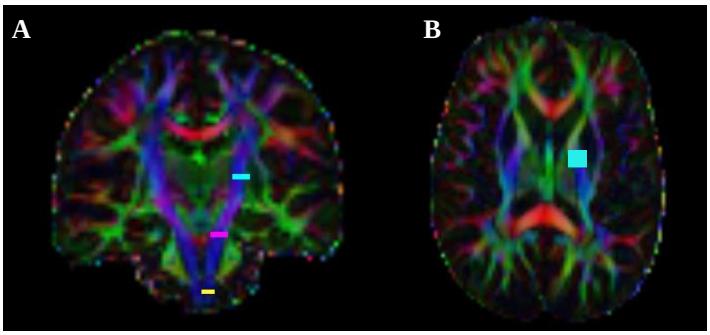

Figure 4.2 | (A) Location of inclusion ROIs for the corticospinal tract. Colours on each eigenvector map represent the main direction of WM tracts (red: left–right, blue: superior-inferior, green: anterior-posterior). The first region is a one-slice thick volume coloured by yellow and delineated on the inferior plane of the axial view, and following inclusion regions were also delineated on the axial plane along the inferior - superior direction using one-slice thick volume coloured by magenta and **(B)** light-blue. See text for anatomical landmarks used.

The corpus callosum was tracked using a single inclusion ROI (see **Figure 4.3**) from a manually delineated entire sagittal cross section (five slices thick, red on the eigenvector map). [10]

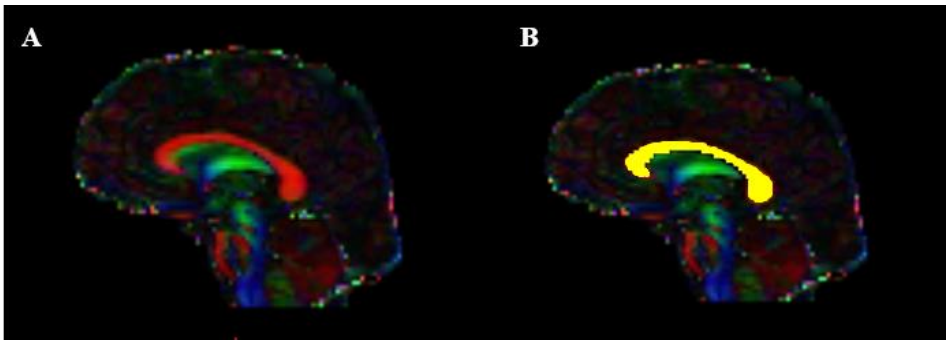

Figure 4.3 | Location of inclusion ROI for the corpus callosum. **(A)** Colours on each eigenvector map represent the main direction of WM tracts (red: left–right, blue: superior-inferior, green: anterior-posterior). **(B)** The inclusion region is a five-slice thick volume coloured by yellow and delineated on the entire sagittal cross section of the corpus callosum.

Exclusion masks were also created in order to avoid streamlines from other WM pathways, and according to the previously knowledge about the expected anatomy of each tract that was aiming to be reconstructed. It is also important to say that tailoring the ROI sizes to encompass the distinguishing anatomical features of the three tracts examined enabled immediate and reliable tract identification, without the need for *post hoc* exclusion ROIs.

The next step was the tracking using the *tckgen* command of MRtrix. Specifically, a probabilistic Anatomically-Constrained Tractography (ACT) algorithm [120] was performed on the resulting FODs, with seeds on the WM-GM boundary. This whole-brain tractography was restricted to reconstruct just the tracts of interest by providing the respective inclusion and exclusion ROIs, forming their *tractograms*. Those tracts were filtered using a spherical deconvolution-informed filtering of tractograms (SIFT) [121] algorithm, to obtain just the streamlines per subject that best match the apparent fibre densities in the reconstructed FODs. The tractography of each WM pathway was performed using auxiliary scripts, and the final result visualized with *mrview* (MRTrix viewer).

Additionally, with the aim of having just the homologous connection of the corpus callosum between motor cortices, it was developed an auxiliary MATLAB function (***Appendix 11.1***) that uses as inputs the numbers of the correspondent labels (which are representations of different parcellations) from the lookup table of FreeSurfer (in this study: left – *1022 ctx-lh-postcentral* / *1024 ctx-lh-precentral*; right – *2022 ctx-rh-postcentral* / *2024 ctx-rh-precentral*). As output, this script returns the ROIs related to the precentral and postcentral regions of each hemisphere, which were consequently used to select the fibres from the corpus callosum between those regions by running the *tckedit* command.

Then, regarding the extraction of the microstructural parameters derived from DTI, DIPY [122] was used to reconstruct the diffusion tensor in each voxel. Knowing that the diffusion tensor model is a model that describes the diffusion from a highly-oriented single fibre population within a voxel, it is still very commonly used in demonstrating the utility of diffusion MRI in characterizing the micro-structure of WM tissue and of the biophysical properties of tissue, inferred from local diffusion properties. So, a python script using the commands of this library was implemented to reconstruct the diffusion tensor and extract associated FA and MD maps (***Appendix 11.2***).

Prior to reconstruction, to decrease computational time, the data was masked and cropped in order to remove the non-brain tissue from each subject´s diffusion image of the whole head. To achieve the expected result, the diffusion image was multiplied by the mask provided by the BET tool.

By calling *fractional_anisotropy* module function, it was possible to generate the FA images from the eigen-values of the tensor; and, the MD images were generated by calling the *mean_diffusivity* module function on the eigen-values.

The next step was also about the generation of microstructural scalar maps. Using DIPY, a script was developed to achieve the MAP-MRI based scalar maps: MSD, RTOP, RTAP, and RTPP (***Appendix 11.3***).

After this, the AMICO toolbox [102] was used to fit the NODDI model to the sample dataset in study (***Appendix 11.4***). In a python shell, the AMICO library, which is based on the fact that the microstructural properties of the tissue can be expressed as a system of linear equations, was imported and the framework was initialized. By loading the data (using as inputs the diffusion image, the gradient scheme and the brain mask computed with BET tool) and setting the model for NODDI, the response functions for all the compartments were generated. Finally, after the NODDI model fitting, the maps of estimated parameters (ODI, ICVF, and ISOVF) were obtained.

5 Along-Tract Analysis

5.1 Methods

With all microstructural features for each subject computed, using MATLAB and through the function *read_mrtrix_tracks* (which was developed by the MRtrix team), a structure containing the header information and subject´s data for each MRtrix format track file was determined. Based on the outputs of this function, it was possible to have access to a list with all the positions automatically generated along each streamline that are part of the reconstruction obtained for each WM pathway using tractography. Then, an auxiliary script was written with the aim to calculate the maximum number of points that were positioned along each subject´s tract in study. Having a list with this maximum number of points along a streamline in each WM pathway (left/right arcuate fasciculus, left/right corticospinal tract, and corpus callosum) per subject, the mode of those values was calculated.

Prior to sampling the values of the microstructural parameters along the reconstructed WM tracts, each streamline in each track file was resampled to a fixed number of points (using the *tckresample* command of MRtrix with *-num_points* as option) in order to ensure that every streamline in each WM tract had the same number of points. This methodology consists of first perform the re-sample of the streamlines at equivalent locations along the tract of interest, by using the "fixed number of points" equal to the value obtained on the previous step through the mode of the maximum number of points initially positioned along each streamline for each subject´s WM pathway. With this step, the streamlines from the arcuate fasciculus had the same number of samples uniformly spaced (see **Figure 5.1**), as well as the streamlines from the corticospinal tract and corpus callosum, across all subjects from the dataset in study.

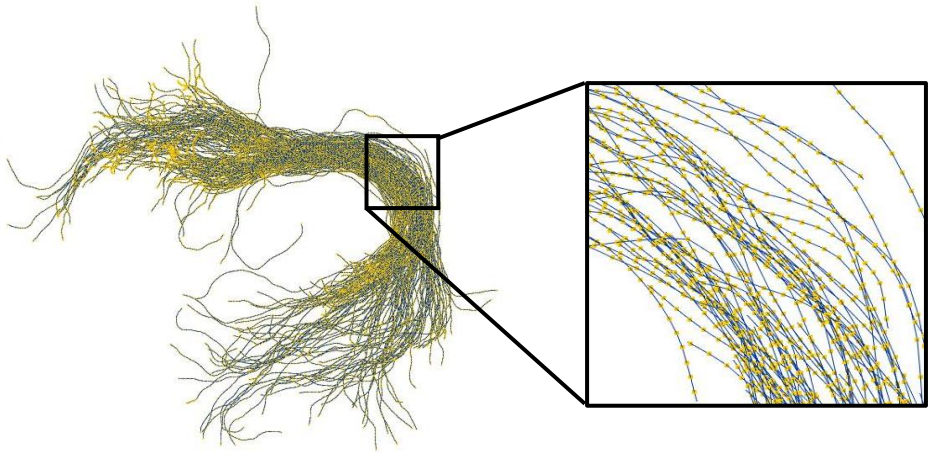

Figure 5.1 | Representation generated using MATLAB of the left arcuate fasciculus (sagittal view) after the re-sampling of each streamline that is part of this WM pathway. Due to this step, all the streamlines have the same number of points distributed along itself. A closer look at the level of the classical arcuate fasciculus ''bottleneck'' allow us to confirm that the position of all the point were done uniformly spaced. The streamlines are coloured in blue and the points were the scalar maps will be sampled are in yellow.

This step was followed by the sample of the values of each scalar map along each WM pathway using the *tcksample* command. This produced a text file with independent information on an equal number of sampled values of the scalar map for each streamline of the specified track file. The results were organized in an excel file, in order to assess the variation of each microstructural parameter (FA, MD, MSD, RTAP, RTOP, RTPP, ODI, ICVF and ISOVF) along the WM tracts, across patients with TLE and healthy controls. All values were plotted along each streamline of the tract and averaged along the whole tract.

This along-tract analysis (summarized in **Figure 5.2**) was a valuable tool to have access to the variance of the microstructural parameters between subjects with TLE and a group of healthy controls. With this purpose in mind, the average graphs of each scalar map were also delineated having in consideration the microstructural information from patients and controls, aiming to compare and describe the differences between these two groups regarding the diffusion properties associated to each one.

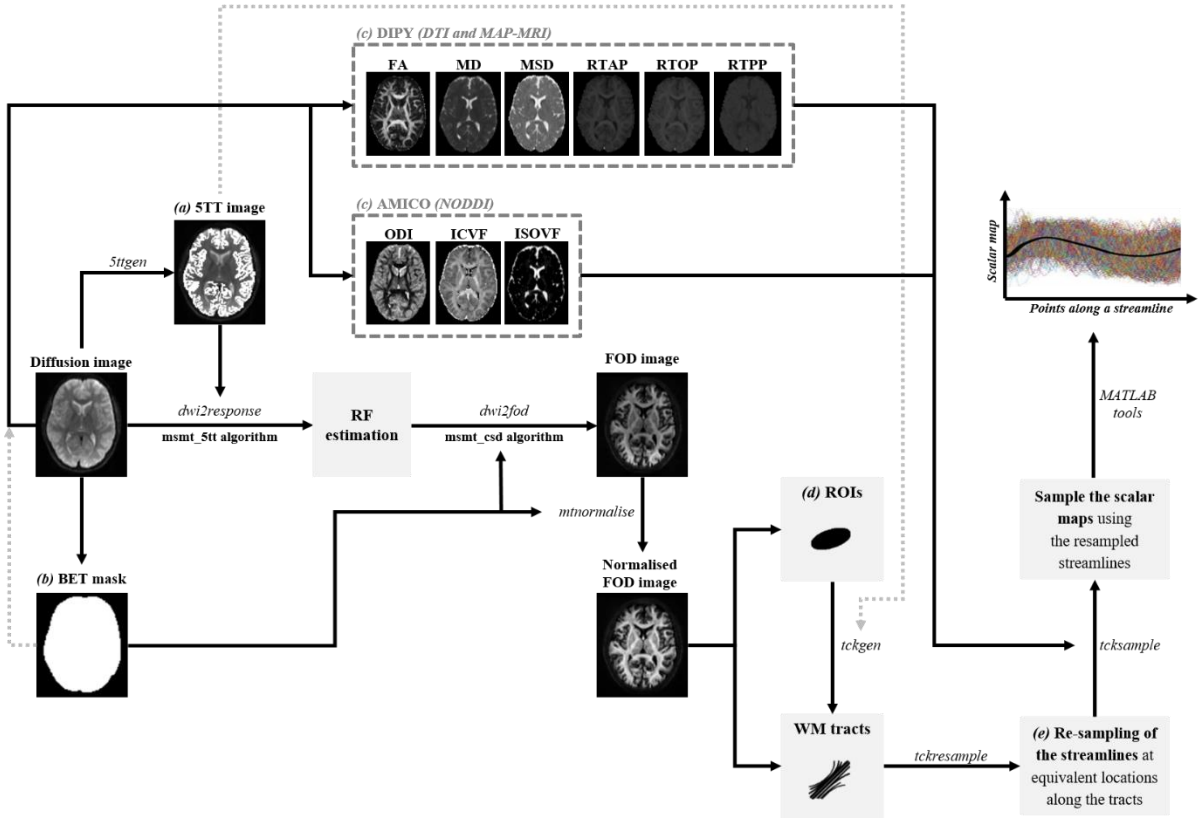

Figure 5.2 | A comprehensive processing pipeline of the different methods applied throughout the Along-tract analysis. After performing the pre-processing methodologies, from the diffusion images were generated: (a) the 5TT images that were posteriorly used as inputs on the estimation of the response functions; (b) the BET masks, which were used to compute the FOD images and their respectively normalised images; and, (c) the microstructural scalar maps using DIPY and AMICO as frameworks, within the BET mask. (d) The ROIs were drawn in order to compute the WM tracts of interest, using the 5TT image to delineate the propagation and termination of streamlines. (e) From each WM pathway reconstructed, each streamline was resampled at equivalent points, which were positioned uniformly spaced along the tracts, and used to sample the scalar maps along the resampled streamlines of each tract. Using MATLAB tools, the along-tract analysis of each scalar map along the WM tracts of interest was computed.

Additionally, with the purpose of having a more specific analysis of the variation of each scalar map along the WM tracts (left/right arcuate fasciculus, left/right corticospinal tract, and corpus callosum - homologous connection between motor cortices), even in a region as the centrum semiovale where there are crossing fibres from the tracts in study, sphere regions were extracted (using the *tckedit* command from MRtrix) from each of the tracts and from the centrum semiovale after merging the tractograms of the three tracts in one track file, for the left and right hemispheres.

Then, the same methodology of resample/sample of the streamlines that was applied to each WM tract was repeated, but now just using these small regions extracted. So, through the calculation of the mode of the maximum number of points initially sampled along each streamline, which positions were listed using *read_mrtrix_tracks* function, it was possible to do the re-sample of each streamline of the extracted regions with points uniformly spaced. After this, the sample of the different scalar maps was performed and the results were plotted using the facilities of MATLAB.

With this step, the main goal was to characterise and describe the microstructural variations taking into account the potentially rich anatomical variation in each diffusion metric not only along the WM pathways of interest in this study (and to do this it was imperative to use a region just with streamlines from the tract of interest), but also along a complex region with multiple crossing fibres from the WM tracts, as the centrum semiovale. In addition, this analysis contributed to obtain a more complete description in terms of the diffusion properties that characterize the neuropathological group in study based on the identification of microstructural changes between patients with TLE and healthy controls.

5.2 Results

Standard tractography methods collapse tract groups and yield only a single mean microstructural metric, by ignoring the potentially rich anatomical variation in diffusion imaging metrics along the tracts and reducing the effectiveness of this technique. With this analysis, we aim to provide a more complete microstructural analysis of the WM tracts of interest, having in mind that along the WM pathways the variation of some diffusion parameters should consider the anatomical features of the tracts: geometric properties of the tract, such as curvature; partial volume effects with neighbouring structures; and the admixing of crossing, branching, merging or kissing fibres from other fibre tracts.

This section is focused on the developing tools that could allow to extract information regarding how microstructural information can be used to guide and improve tractography algorithm. With this aim, it was developed a workflow to conduct along-tract analysis of WM pathways of interest and integrate not only diffusion tensor measures, since their biological interpretation is often equivocal, but also more advanced parameters from MAP-MRI and NODDI, having also in consideration just a small extracted region from the whole tract, and a complex region with crossing fibres as the centrum semiovale. And secondly, it was investigated each diffusion profile drawn by each microstructural parameter along the reconstructed WM tracts between TLE patients and healthy controls in order to identify microstructural changes between these two groups.

5.2.1 Single-subject analysis: normal region *versus* complex region

Note that in this section, tractography of each WM pathway and associated microstructural scalar maps are illustrated for a subject with 17 years old who posteriorly had undergone an extended left temporal lobectomy.

Firstly, the tractography of each WM pathway in study (arcuate fasciculus, corticospinal tract and corpus callosum – homologous connection between motor cortices) was performed (see **Figure 5.3 (A)**), which allowed us to merge each resulted tractogram in just one track file, from where it was extracted a complex region, the centrum semiovale. In each WM pathway reconstructed was also highlighted, using a white sphere, a small spherical region considered to be a good representation of the whole tract avoiding potential fibres from other WM pathways in the neighbourhood (see **Figure 5.3 (B)**). Following the sequential steps described along the previous section, **Figure 5.3 (C)** represents a reconstruction obtained with MATLAB for each subject´s WM tract in the study, after every streamline has been resampled to a fixed number of points uniformly spaced along the tract of interest. It is also imperative to highlight that this "number of points" was calculate using the mode of the maximum number of positions automatically generated along each streamline from each WM pathway reconstructed using tractography. This "number" was then specific for each WM tract, which quantitatively means that the arcuate fasciculus' streamlines were resampled using 182 points, the corticospinal tract's streamlines were resampled using 201 points, the corpus callosum's streamlines

were resampled using 163 points, and the merging tractograms were resampled using 243 points. Before sampling the metrics values, it was also necessary to resample each extracted streamline of the WM tracts within the masking ROI at points uniformly spaced, following the same methodology that was applied before to the whole tract. The "number of points" was again calculate using the mode of the maximum number of positions automatically generated along each extracted streamline from the WM pathways, with the arcuate fasciculus' streamlines resampled using 39 points, the corticospinal tract's streamlines resampled using 29 points, the corpus callosum's streamlines resampled using 27 points, and the streamlines part of the centrum semiovale resampled using 74 points.

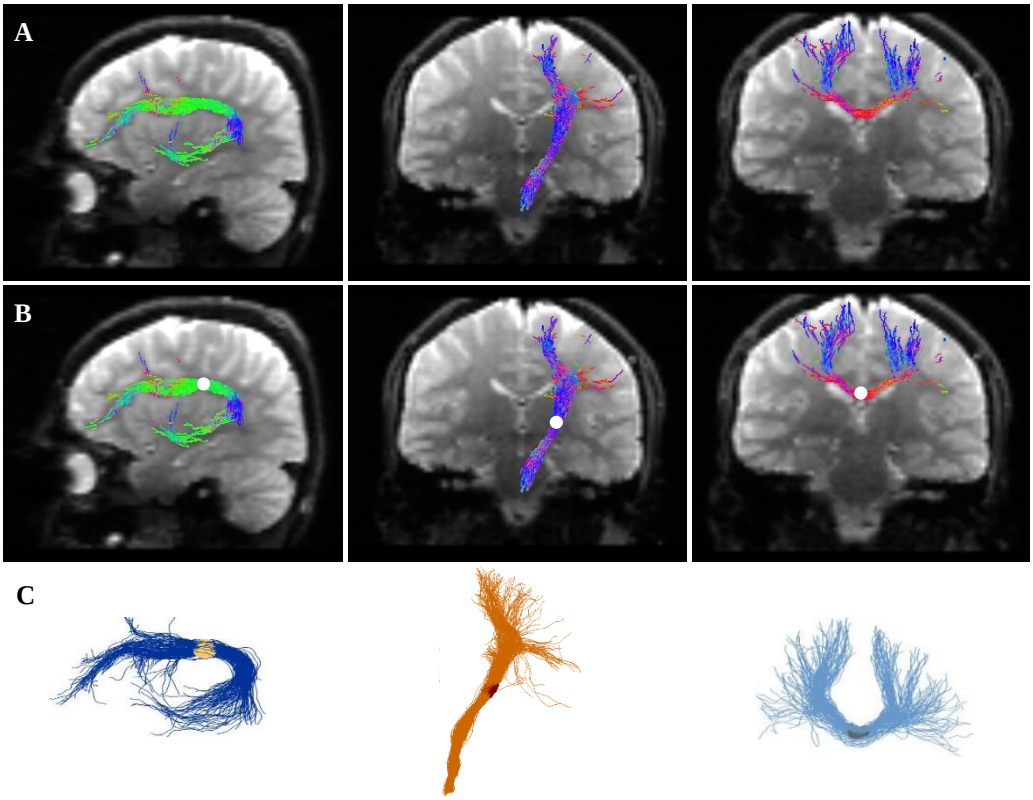

Figure 5.3 | (A) Tractography of the left arcuate fasciculus (left, sagittal view), left corticospinal tract (middle, coronal view) and corpus callosum (right, coronal view); **(B)** Spherical ROI extracted from each WM pathway (left arcuate fasciculus (left, sagittal view), left corticospinal tract (middle, coronal view) and corpus callosum (right, coronal view) coloured by white and overlapped on (A); **(C)** MATLAB reconstruction: left arcuate fasciculus (left, sagittal view) coloured by blue and with the extracted spherical ROI coloured by yellow, left corticospinal tract (middle, coronal view) coloured by orange and with the extracted spherical ROI coloured by red, and corpus callosum - homologous connection between motor cortices (right, coronal view) coloured by light-blue and with the extracted spherical ROI coloured by grey.

Based on the DT and its reconstruction in each voxel achieved by DIPY, MD and FA scalar maps were obtained along the WM tracts and the respective extracted region, for all subjects. The MAP-MRI based scalar maps (MSD, RTAP, RTOP, and RTPP) were generated using also the facilities of DIPY, and the NODDI model was fitted using the AMICO toolbox, and as result, ODI, ICVF and ISOVF volumes were mapped.

The sample of the values of each scalar map along each WM tract in study and each extracted region is shown by **Figure 5.4** (left hemisphere) and **Figure 5.5** (right hemisphere). It is also shown how each microstructural parameter change even in a complex region as the centrum semiovale. Each coloured line of the following graphs represents a streamline that is part of the tract for which we aim to delineate a specific microstructural signature, on the other hand the thick line represents the average variation of each microstructural parameter along the tract. In order to ensure a better analysis of these results, in ***Appendix 11.6 (Figure 11.1 – 11.6)*** we can find the next two figures in a larger scale.

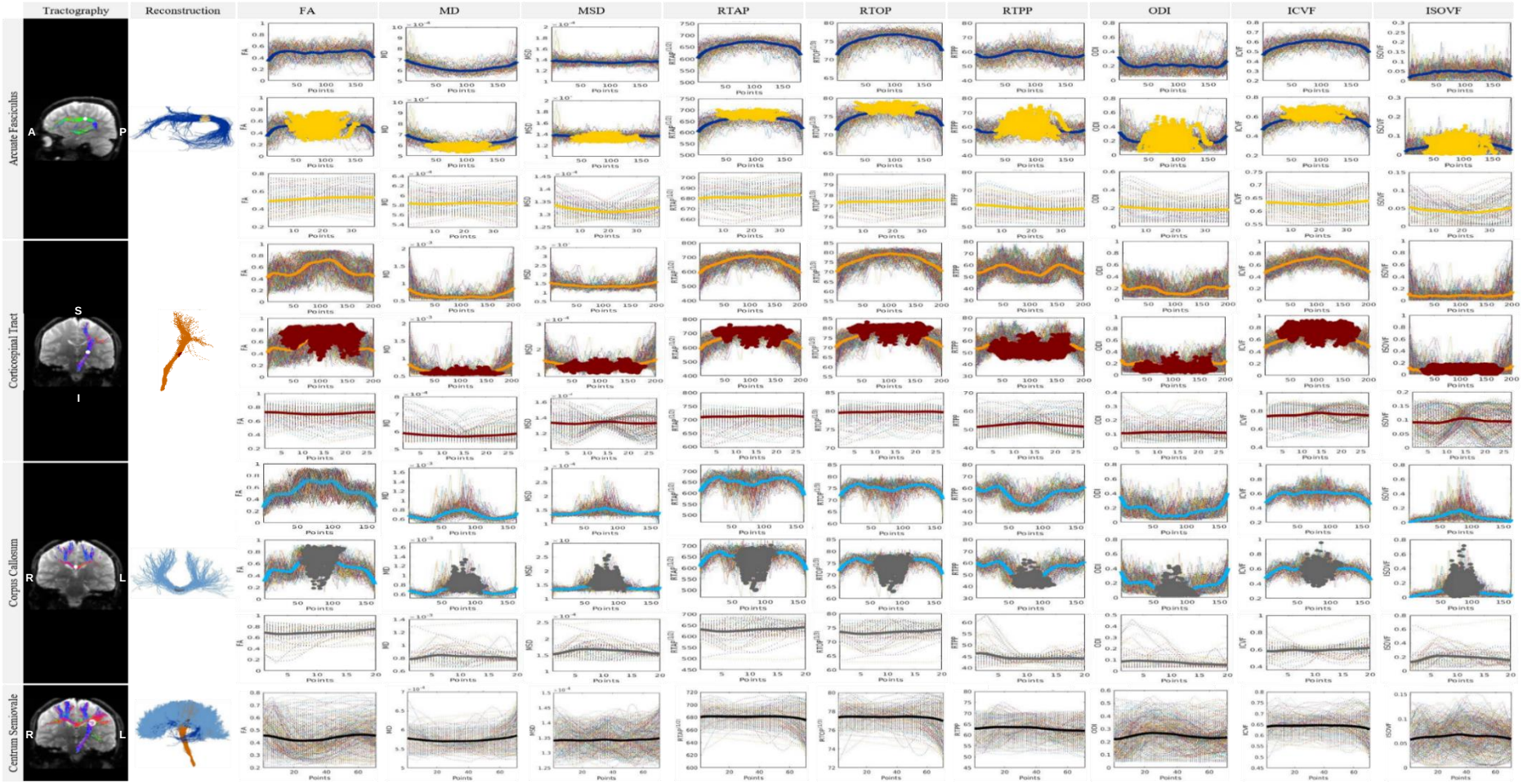

Figure 5.4 | Along-tract analysis of the left arcuate fasciculus (AF), left corticospinal tract (CST), corpus callosum (CC) - homologous connection between motor cortices, and left centrum semiovale (from top to bottom) based on their tractograms (first column), from which it was possible to generate the reconstructions via MATLAB (second column). The following columns are divided in groups of three rows. The first row illustrate the variation of each microstructural parameter (fractional anisotropy (FA), mean diffusivity (MD), mean square displacement (MSD), (square-root of) return to axis probability (RTAP), (cube-root of) return to origin probability (RTOP), return to plane probability (RTPP), orientation dispersion index (ODI), intracellular volume fraction (ICVF) and isotropic volume fraction (ISOVF)) along each WM tract of interest. In the second row, it was highlighted, from all the streamlines, the value of each diffusion metric assumed by each resampled point that is part of the extracted ROI from each WM pathway. The respective average variation of each scalar map along the extracted ROI is represented in the third row of graphs. The reconstruction of left AF was coloured by blue and its analyses should follow the A-P direction, the left CST by orange and following the I-S direction, and the CC by light-blue and following the R-L direction, from which the extracted ROIs were coloured by yellow, red and grey, respectively. The centrum semiovale (left hemisphere) was coloured by black after merging the left AF (blue), left CST (orange) and CC (light-blue) and its analyses should follow the R-L direction. The units of MD and MSD are mm^2/s, and RTAP, RTOP and RTPP are given by mm^{-1}. Abbreviations: A – anterior; P – posterior; S – superior; I – inferior; L – left; R – right.

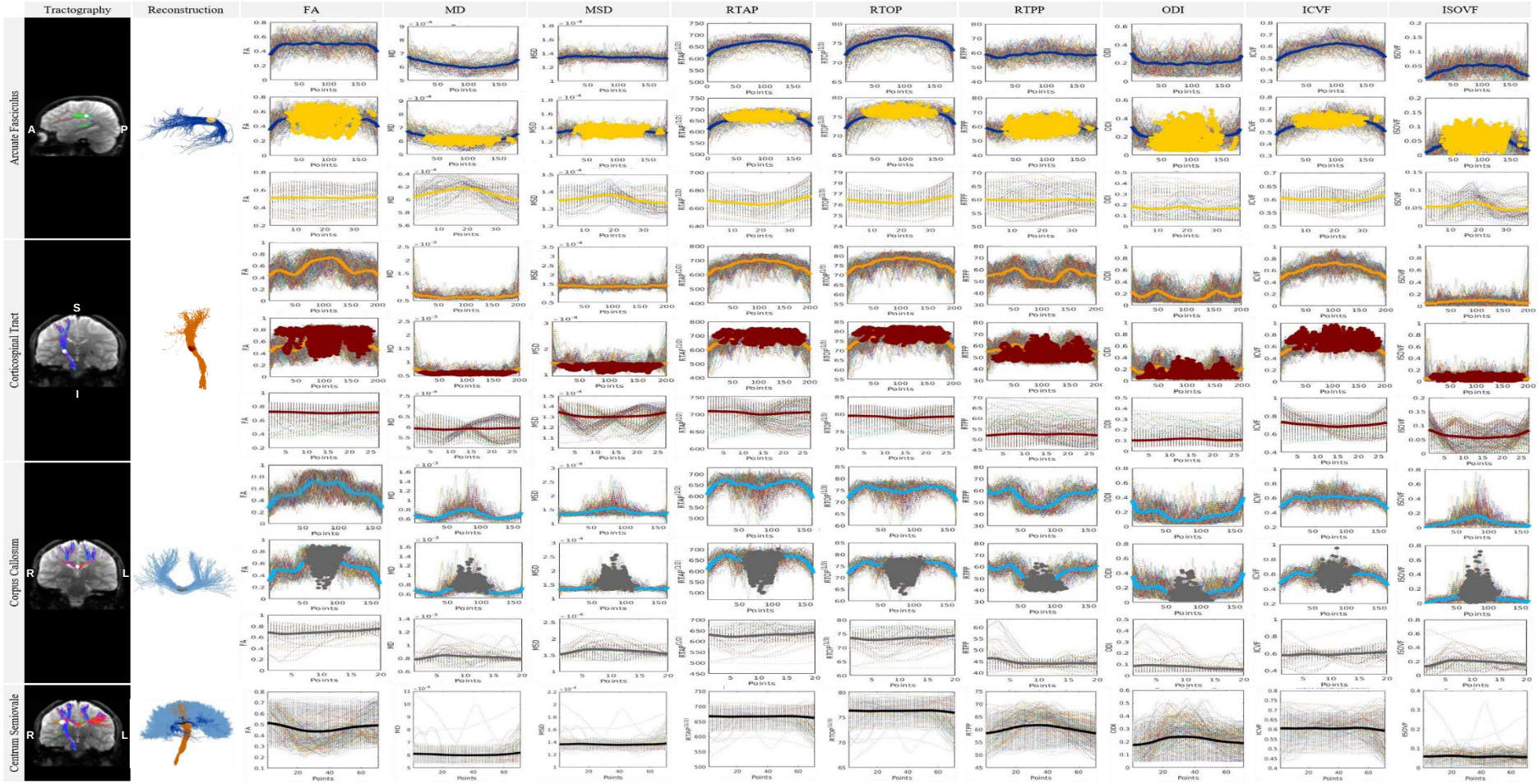

Figure 5.5 | Along-tract analysis of the right arcuate fasciculus (AF), right corticospinal tract (CST), corpus callosum (CC) - homologous connection between motor cortices, and right centrum semiovale (from top to bottom) based on their tractograms (first column), from which it was possible to generate the reconstructions via MATLAB (second column). The following columns are divided in groups of three rows. The first row illustrate the variation of each microstructural parameter (fractional anisotropy (FA), mean diffusivity (MD), mean square displacement (MSD), (square-root of) return to axis probability (RTAP), (cube-root of) return to origin probability (RTOP), return to plane probability (RTPP), orientation dispersion index (ODI), intracellular volume fraction (ICVF) and isotropic volume fraction (ISOVF)) along each WM tract of interest. In the second row, it was highlighted, from all the streamlines, the value of each diffusion metric assumed by each resampled point that is part of the extracted ROI from each WM pathway. The respective average variation of each scalar map along the extracted ROI is represented in the third row of graphs. The reconstruction of right AF was coloured by blue and its analyses should follow the A-P direction, the right CST by orange and following the I-S direction, and the CC by light-blue and following the R-L direction, from which the extracted ROIs were coloured by yellow, red and grey, respectively. The centrum semiovale (right hemisphere) was coloured by black after merging the right AF (blue), right CST (orange) and CC (light-blue) and its analyses should follow the R-L direction. The units of MD and MSD are mm^2/s, and RTAP, RTOP and RTPP are given by mm^{-1}. Abbreviations: A – anterior; P – posterior; S – superior; I – inferior; L – left; R – right.

In order to be able to quantitative describe the variation of each scalar map along the WM pathways of interest, the values assumed (as "reference values") by the microstructural parameters at three different sections (start, middle, end) of each tract, across the TLE patient in study, were summarized in **Table 5.1 – 5.3**. Furthermore, **Table 5.4** illustrates the minimum and maximum values of the averaged variation of each diffusion metric along the centrum semiovale, for each hemispheric side.

Table 5.1 | Values provided by the along-tract analysis of fractional anisotropy (FA), mean diffusivity (MD), mean square displacement (MSD), (square-root of) return to axis probability (RTAP), (cube-root of) return to origin probability (RTOP), return to plane probability (RTPP), orientation dispersion index (ODI), intracellular volume fraction (ICVF) and isotropic volume fraction (ISOVF) along the arcuate fasciculus (left and right), taking into account three different sections (start, middle, end) of this white matter tract. Each value represents the average value of each microstructural parameter $\pm$ the standard deviation associated, across the TLE patient in study. The units of MD and MSD are mm^2/s, and RTAP, RTOP and RTPP are given by mm^{-1}.

	Left Arcuate Fasciculus			**Right Arcuate Fasciculus**		
	Broca's area	*Geschwind's area*	*Wernicke's area*	*Broca's area*	*Geschwind's area*	*Wernicke's area*
FA	0.3326 ± 0.1342	0.4756 ± 0.1059	0.3943 ± 0.1192	0.3414 ± 0.1068	0.4964 ± 0.1119	0.3832 ± 0.1206
MD	0.0007000 ± 0.0000502	0.0005939 ± 0.0000326	0.0006805 ± 0.0000562	0.0006774 ± 0.0000382	0.0005964 ± 0.0000353	0.0006575 ± 0.0000404
MSD	0.0001363 ± 0.0000082	0.0001345 ± 0.0000046	0.0001358 ± 0.0000088	0.0001323 ± 0.0000057	0.0001342 ± 0.0000047	0.0001317 ± 0.0000063
RTAP	600.8982 ± 29.0248	672.7215 ± 17.3365	614.8866 ± 32.4175	608.4153 ± 26.3697	672.5108 ± 18.9524	622.7768 ± 28.4802
RTOP	71.1906 ± 2.2895	76.7700 ± 1.3247	72.2872 ± 2.5567	71.7866 ± 2.0724	76.7529 ± 1.4441	72.9101 ± 2.2279
RTPP	58.6962 ± 3.1681	61.2225 ± 4.1840	57.8886 ± 3.3165	59.2416 ± 2.6097	60.1803 ± 4.5375	59.1529 ± 3.2947
ODI	0.3288 ± 0.1312	0.2132 ± 0.1061	0.2718 ± 0.1046	0.3137 ± 0.1012	0.1976 ± 0.1034	0.2872 ± 0.1043
ICVF	0.4594 ± 0.0548	0.6149 ± 0.0452	0.4877 ± 0.0647	0.4717 ± 0.0506	0.6182 ± 0.0500	0.5009 ± 0.0551
ISOVF	0.0137 ± 0.0180	0.0488 ± 0.0232	0.0211 ± 0.0306	0.0071 ± 0.0109	0.0538 ± 0.0231	0.0128 ± 0.0194

Table 5.2 | Values provided by the along-tract analysis of fractional anisotropy (FA), mean diffusivity (MD), mean square displacement (MSD), (square-root of) return to axis probability (RTAP), (cube-root of) return to origin probability (RTOP), return to plane probability (RTPP), orientation dispersion index (ODI), intracellular volume fraction (ICVF) and isotropic volume fraction (ISOVF) along the corticospinal tract (left and right), taking into account three different sections (start, middle, end) of this white matter tract. Each value represents the average value of each microstructural parameter $\pm$ the standard deviation associated, across the TLE patient in study. The units of MD and MSD are mm^2/s, and RTAP, RTOP and RTPP are given by mm^{-1}.

	Left Corticospinal Tract			**Right Corticospinal Tract**		
	At the level of brainstem	*At the level of internal capsule*	*At the level of motor cortex*	*At the level of brainstem*	*At the level of internal capsule*	*At the level of motor cortex*
FA	0.4126 ± 0.1644	0.6999 ± 0.1072	0.4315 ± 0.1605	0.4212 ± 0.1579	0.7228 ± 0.1042	0.4381 ± 0.1529
MD	0.0008493 ± 0.0002765	0.0005862 ± 0.0000475	0.0008704 ± 0.000319	0.0007939 ± 0.0002609	0.0006072 ± 0.0000714	0.0007765 ± 0.0002373
MSD	0.0001591 ± 0.0000380	0.0001324 ± 0.0000087	0.0001569 ± 0.0000392	0.0001487 ± 0.0000326	0.0001358 ± 0.0000115	0.0001468 ± 0.0000297
RTAP	585.2448 ± 54.2943	708.4938 ± 21.8747	595.6669 ± 60.5585	593.1641 ± 52.9391	706.0574 ± 30.3871	600.2441 ± 53.1029
RTOP	69.8983 ± 4.3669	79.4652 ± 1.6516	70.7116 ± 4.8460	70.5303 ± 4.2947	79.2746 ± 2.3057	71.0922 ± 4.2771
RTPP	52.7403 ± 7.6897	53.5081 ± 5.3737	52.5388 ± 7.5503	54.1549 ± 7.2574	52.1260 ± 5.9923	54.1482 ± 6.5715
ODI	0.2655 ± 0.1655	0.1034 ± 0.0566	0.2477 ± 0.1630	0.2389 ± 0.1686	0.0947 ± 0.0516	0.2217 ± 0.1492
ICVF	0.4530 ± 0.0937	0.7339 ± 0.0684	0.4656 ± 0.1089	0.4531 ± 0.0933	0.7166 ± 0.0822	0.4709 ± 0.0904
ISOVF	0.1247 ± 0.1832	0.0838 ± 0.0437	0.1510 ± 0.2110	0.0702 ± 0.1485	0.0948 ± 0.0492	0.0688 ± 0.1318

Table 5.3 | Values provided by the along-tract analysis of fractional anisotropy (FA), mean diffusivity (MD), mean square displacement (MSD), (square-root of) return to axis probability (RTAP), (cube-root of) return to origin probability (RTOP), return to plane probability (RTPP), orientation dispersion index (ODI), intracellular volume fraction (ICVF) and isotropic volume fraction (ISOVF) along the corpus callosum - homologous connection between motor cortices, taking into account three different sections (start, middle, end) of this white matter tract. Each value represents the average value of each microstructural parameter $\pm$ the standard deviation associated, across the TLE patient in study. The units of MD and MSD are mm^2/s, and RTAP, RTOP and RTPP are given by mm^{-1}.

	Corpus Callosum		
	Near the cortical region of the right hemisphere	*At the level of the mid-sagittal plane*	*Near the cortical region of the left hemisphere*
FA	0.2964 ± 0.1277	0.7042 ± 0.1418	0.2489 ± 0.1159
MD	0.0006869 ± 0.0000674	0.0008155 ± 0.0001455	0.0007427 ± 0.0001453
MSD	0.0001352 ± 0.0000120	0.0001575 ± 0.0000230	0.0001432 ± 0.0000206
RTAP	605.7924 ± 32.1487	635.0490 ± 43.1766	589.0861 ± 39.2985
RTOP	71.5725 ± 2.5414	73.8430 ± 3.3880	70.2373 ± 3.1525
RTPP	60.3508 ± 2.9770	45.1417 ± 4.8397	59.6628 ± 3.6751
ODI	0.3594 ± 0.1244	0.0844 ± 0.0735	0.4033 ± 0.1269
ICVF	0.4670 ± 0.0571	0.6232 ± 0.0844	0.4449 ± 0.0632
ISOVF	0.0152 ± 0.0293	0.1766 ± 0.1165	0.0459 ± 0.0876

Table 5.4 | Values provided by the along-tract analysis of fractional anisotropy (FA), mean diffusivity (MD), mean square displacement (MSD), (square-root of) return to axis probability (RTAP), (cube-root of) return to origin probability (RTOP), return to plane probability (RTPP), orientation dispersion index (ODI), intracellular volume fraction (ICVF) and isotropic volume fraction (ISOVF) along the centrum semiovale (left and right hemisphere), taking into account the minimum and maximum values of the averaged variation along this complex region with multiple fibre populations from the arcuate fasciculus, corticospinal tract and corpus callosum. Each value represents the average value of each microstructural parameter $\pm$ the standard deviation associated, across the TLE patient in study. The units of MD and MSD are mm^2/s, and RTAP, RTOP and RTPP are given by mm^{-1}.

	Right Centrum Semiovale		**Left Centrum Semiovale**	
	Minimum	*Maximum*	*Minimum*	*Maximum*
FA	0.4159 ± 0.1060	0.4640 ± 0.0994	0.4368 ± 0.1183	0.5145 ± 0.1097
MD	0.0005700 ± 0.0000181	0.0005852 ± 0.0000328	0.0005983 ± 0.0000338	0.0006191 ± 0.0000571
MSD	0.0001341 ± 0.0000036	0.0001349 ± 0.0000049	0.0001356 ± 0.0000046	0.0001377 ± 0.0000080
RTAP	675.4714 ± 20.1501	681.6977 ± 10.7638	661.9629 ± 30.0824	667.8986 ± 17.9269
RTOP	76.9771 ± 1.5357	77.4550 ± 0.8153	75.9371 ± 2.3198	76.4021 ± 1.3714
RTPP	61.9657 ± 4.2052	63.6928 ± 4.1299	58.4471 ± 3.6543	61.7158 ± 4.2187
ODI	0.2208 ± 0.1072	0.2692 ± 0.1073	0.1759 ± 0.0836	0.2391 ± 0.1068
ICVF	0.6283 ± 0.0525	0.6463 ± 0.0301	0.5929 ± 0.0695	0.6084 ± 0.0432
ISOVF	0.0575 ± 0.0234	0.0681 ± 0.0265	0.0559 ± 0.0233	0.0626 ± 0.0226

The results suggested by the previous example will be discussed in detail along the ***Section 5.3.1***. It will be taken into account how each microstructural parameter change along each WM tract of interest, as well as the diffusion profile assumed by each scalar map at the centrum semiovale, having also in mind the contribution of each tract individually to achieve that specific values along this complex region.

5.2.2 Between-group analysis: TLE patients *versus* healthy controls

Aiming to better describe the microstructural changes between patients with TLE and healthy controls, the following figures (**Figure 5.6** and **Figure 5.7**) show the average results of each microstructural feature along the left and right arcuate fasciculus, the left and right corticospinal tract, and the corpus callosum - homologous connection between motor cortices. The focus of this along-tract analysis was TLE patients with left epileptic focus (9 patients, 5 male, mean age 12 years, range 5 – 19 years), which were selected from our initial population in study, and compared to healthy controls (9 subjects, 5 male, mean age 12 years, range age 8 – 18 years); allowing us to distinguish the different diffusion properties associated to each group and discuss the relationship between them and the neurological condition present in the patients against the controls. Additionally, a Kruskal-Wallis test was also executed in order to verify that the groups are statically different, taking into account three sections (start, middle, end) of each tract with equivalent number of resampled points. A 1% significance value was considered.

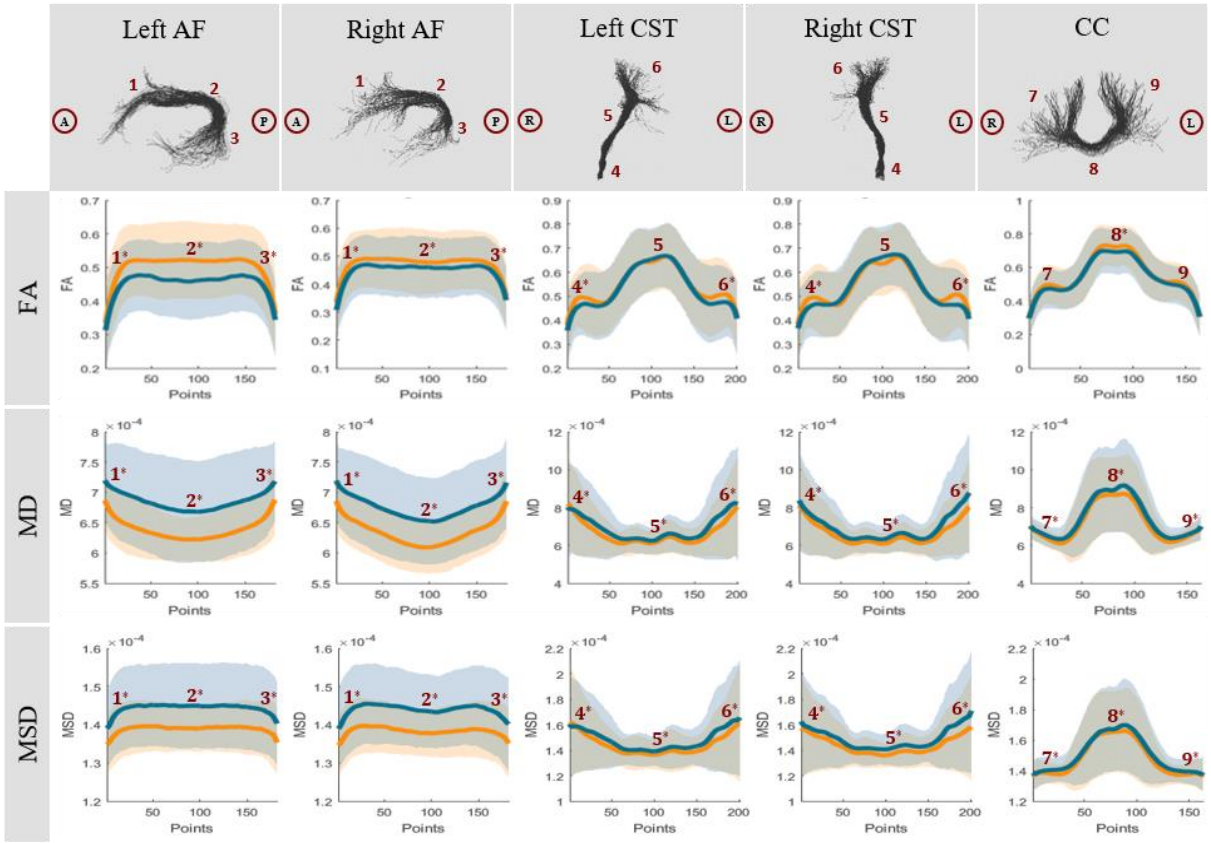

Figure 5.6 | Along-tract analysis of the fractional anisotropy (FA), mean diffusivity (MD) and mean square displacement (MSD) along (from left to right) the left / right arcuate fasciculus (AF), where **(1)** represents the Broca's area, **(2)** the Geschwind's area and **(3)** the Wernicke's area; the left / right corticospinal tract (CST), where **(4)** represents the region near the brainstem, **(5)** the region at the level of the internal capsule and **(6)** the region near the motor cortex; and the corpus callosum (CC) - homologous connection between motor cortices, where **(7)** represents the connections to right motor cortex, **(8)** the colossal fibres near the mid-sagittal plane and **(9)** the connections to left motor cortex. The level of significance is represented by one star (*) where the *p-value* is lower than 0.01 (i.e. difference between groups with statistical relevance). The average variation of each microstructural parameter across the TLE patients is represented by the blue line and the associated standard deviation coloured by light-blue; and, the average variation of each microstructural parameter across the healthy controls is represented by the orange line and the associated standard deviation coloured by light-orange. The units of MD and MSD are mm^2/s. Abbreviations: A – anterior; P – posterior; L – left; R – right.

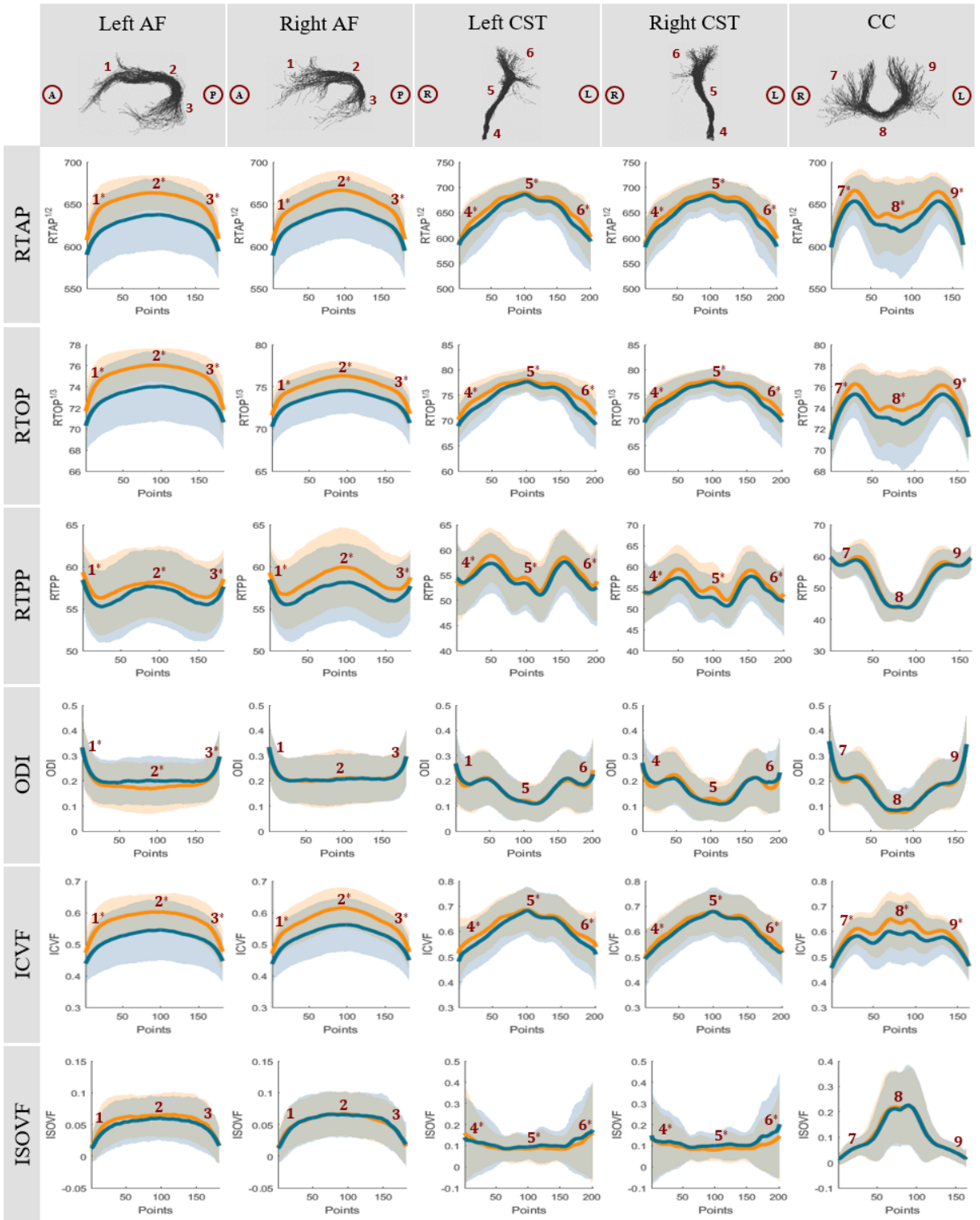

Figure 5.7 | Along-tract analysis of the (square-root of) return-to-the-axis probability (RTAP), (cube-root of) return-to-the-origin probability (RTOP), return-to-the plane probability (RTPP), orientation dispersion index (ODI), intracellular volume fraction (ICVF), and isotropic volume fraction (ISOVF) along (from left to right) the left / right arcuate fasciculus (AF), where **(1)** represents the Broca's area, **(2)** the Geschwind's area and **(3)** the Wernicke's area; the left / right corticospinal tract (CST), where **(4)** represents the region near the brainstem, **(5)** the region at the level of the internal capsule and **(6)** the region near the motor cortex; and the corpus callosum (CC) - homologous connection between motor cortices, where **(7)** represents the connections to right motor cortex, **(8)** the colossal fibres near the mid-sagittal plane and **(9)** the connections to left motor cortex. The level of significance is represented by one star (*) where the *p-value* is lower than 0.01 (i.e. difference between groups with statistical relevance). The average variation of each microstructural parameter across the TLE patients is represented by the blue line and the associated standard deviation coloured by light-blue; and, the average variation of each microstructural parameter across the healthy controls is represented by the orange line and the associated standard deviation coloured by light-orange. The units of RTAP, RTOP and RTPP are mm^{-1}. Abbreviations: A – anterior; P – posterior; L – left; R – right.

In order to be able to perform a comparison analysis between the groups with high specificity, the quantitative findings regarding the variation of each scalar map along the WM pathways of interest were summarized in **Table 5.5 – 5.7**, which illustrate the values assumed (as "reference values") by the microstructural parameters at three different sections (start, middle, end) of each WM tract, across the TLE patients and healthy controls.

Table 5.5 | Values provided by the along-tract analysis of fractional anisotropy (FA), mean diffusivity (MD), mean square displacement (MSD), (square-root of) return to axis probability (RTAP), (cube-root of) return to origin probability (RTOP), return to plane probability (RTPP), orientation dispersion index (ODI), intracellular volume fraction (ICVF) and isotropic volume fraction (ISOVF) along the arcuate fasciculus (left and right), taking into account three different sections (start, middle, end) of this white matter tract. Each value represents the average value of each microstructural parameter $\pm$ the standard deviation associated, across the TLE patients and healthy controls. The level of significance is represented by one star (*) where the *p-value* is lower than 0.01 (i.e. difference between groups with statistical relevance). The units of MD and MSD are mm^2/s, and RTAP, RTOP and RTPP are given by mm^{-1}.

	Left Arcuate Fasciculus						**Right Arcuate Fasciculus**					
	Broca's area		*Geschwind's area*		*Wernicke's area*		*Broca's area*		*Geschwind's area*		*Wernicke's area*	
	TLE	Controls	TLE	Controls	TLE	Controls	TLE	Controls	TLE	Controls	TLE	Controls
FA	0.3130* ± 0.1123	0.3357* ± 0.1251	0.4575* ± 0.1142	0.5222* ± 0.1136	0.3438* ± 0.1121	0.3621* ± 0.1241	0.3077* ± 0.1080	0.3359* ± 0.1110	0.4599* ± 0.1110	0.4793* ± 0,1137	0.3431* ± 0.1130	0.3567* ± 0.1160
MD	0.000720* ± 0.000065	0.000687* ± 0.000050	0.000669* ± 0.000085	0.000622* ± 0.000036	0.000718* ± 0.000066	0.000688* ± 0.000056	0.000719* ± 0.000066	0.000686* ± 0.000047	0.000653* ± 0.000072	0.000609* ± 0.000043	0.000716* ± 0.000077	0.000685* ± 0.000051
MSD	0.000139* ± 0.000010	0.000135* ± 0.000008	0.000145* ± 0.000011	0.000139* ± 0.000006	0.000140* ± 0.000011	0.000135* ± 0.000009	0.000139* ± 0.000011	0.000135* ± 0.000008	0.000144* ± 0.000010	0.000138* ± 0.000006	0.000140* ± 0.000013	0.000135* ± 0.000009
RTAP	589.7206* ± 32.8664	607.0301* ± 30.3228	636.8385* ± 42.5961	663.2598* ± 20.4569	593.8082* ± 33.9718	608.7195* ± 33.1051	588.9008* ± 31.5346	606.2940* ± 27.2179	643.6321* ± 35.3609	666.6062* ± 23.0112	594.6570* ± 34.0421	608.3667* ± 29.7856
RTOP	70.2986* ± 2.6173	71.6725* ± 2.3895	73.9827* ± 3.3399	76.0460* ± 1.5669	70.6218* ± 2.6976	71.8017* ± 2.6081	70.2353* ± 2.5133	71.6183* ± 2.1493	74.5204* ± 2.7588	76.2995* ± 1.7621	70.6887* ± 2.7156	71.7784* ± 2.3490
RTPP	58.4233* ± 3.5744	59.3445* ± 3.4742	57.6256* ± 4.3534	58.0963* ± 4.1584	57.6307* ± 3.5493	58.5387* ± 3.5568	58.4629* ± 3.5899	59.2965* ± 3.2650	58.1018* ± 4.6333	59.9131* ± 4.7147	57.6840* ± 3.9547	58.7344* ± 3.3214
ODI	0.3329* ± 0.1203	0.3307* ± 0.1229	0.2013* ± 0.0983	0.1680* ± 0.0994	0.2958* ± 0.1098	0.2963* ± 0.1129	0.3339 ± 0.1182	0.3258 ± 0.1128	0.2063 ± 0.1023	0.2097 ± 0.1135	0.2960 ± 0.1142	0.2978 ± 0.1100
ICVF	0.4381* ± 0.0627	0.4729* ± 0.0612	0.5430* ± 0.0962	0.6014* ± 0.0566	0.4465* ± 0.0673	0.4764* ± 0.0667	0.4367* ± 0.0604	0.4700* ± 0.0537	0.5606* ± 0.0849	0.6145* ± 0,0648	0.4488* ± 0.0640	0.4749* ± 0.0582
ISOVF	0.0121 ± 0.0228	0.0150 ± 0.0257	0.0592 ± 0.0346	0.0643 ± 0.0335	0.0164 ± 0.0280	0.0168 ± 0.0285	0.0125 ± 0.0293	0.0140 ± 0.0250	0.0656 ± 0.0354	0.0664 ± 0.0346	0.0186 ± 0.0374	0.0154 ± 0.0275

Table 5.6 | Values provided by the along-tract analysis of fractional anisotropy (FA), mean diffusivity (MD), mean square displacement (MSD), (square-root of) return to axis probability (RTAP), (cube-root of) return to origin probability (RTOP), return to plane probability (RTPP), orientation dispersion index (ODI), intracellular volume fraction (ICVF) and isotropic volume fraction (ISOVF) along the corticospinal tract (CST, left and right), taking into account three different sections (start, middle, end) of this white matter tract. Each value represents the average value of each microstructural parameter ± the standard deviation associated, across the TLE patients and healthy controls. The level of significance is represented by one star (*) where the *p-value* is lower than 0.01 (i.e. difference between groups with statistical relevance). The units of MD and MSD are mm^2/s, and RTAP, RTOP and RTPP are given by mm^{-1}.

	Left Corticospinal Tract						**Right Corticospinal Tract**					
	At the level of brainstem		*At the level of internal capsule*		*At the level of motor cortex*		*At the level of brainstem*		*At the level of internal capsule*		*At the level of motor cortex*	
	TLE	Controls	TLE	Controls	TLE	Controls	TLE	Controls	TLE	Controls	TLE	Controls
FA	0.3568* ± 0.1544	0.3813* ± 0.1428	0.6547 ± 0.1272	0.6437 ± 0.1285	0.4067* ± 0.1603	0.4138* ± 0.14889	0.3658* ± 0.1490	0.3830* ± 0.1518	0.6446 ± 0.1248	0.6559 ± 0.1340	0.4052* ± 0.1530	0.4208* ± 0.1600
MD	0.000801* ± 0.000272	0.000819* ± 0.000270	0.000624* ± 0.000071	0.000611* ± 0.000065	0.000820* ± 0.000309	0.000802* ± 0.000273	0.000838* ± 0.000267	0.000809* ± 0.000256	0.0006312* ± 0.000074	0.000609* ± 0.000057	0.000877* ± 0.000318	0.000802* ± 0.000264
MSD	0.000160* ± 0.000041	0.000162* ± 0.000045	0.000139* ± 0.000012	0.000136* ± 0.000012	0.000166* ± 0.000046	0.000160* ± 0.000046	0.000163* ± 0.000043	0.000157* ± 0.000041	0.000141* ± 0.000012	0.000136* ± 0.000010	0.000171* ± 0.000048	0.000158* ± 0.000042
RTAP	585.3306* ± 50.3936	588.8720* ± 49.9674	685.7362* ± 33.8459	689.6537* ± 30.7613	592.9129* ± 60.9917	601.5638* ± 56.6732	581.2712* ± 50.9790	587.7421* ± 47.8737	683.8566* ± 35.3607	689.2011* ± 28.4669	582.6295* ± 63.3671	598.2669* ± 56.1135
RTOP	69.9148* ± 4.0446	70.1984* ± 3.9973	77.7411* ± 2.5831	78.0408* ± 2.3482	70.4918* ± 4.8780	71.1900* ± 4.5012	69.5885* ± 4.1128	70.1129* ± 3.8362	77.5969* ± 2.7020	78.0093* ± 2.1684	69.6642* ± 5.1037	70.9302* ± 4.4674
RTPP	54.3191* ± 7.3265	53.8800* ± 7.7448	53.3125* ± 5.4607	54.4246* ± 5.4082	52.4853* ± 7.6404	53.7527* ± 7.6529	53.9339* ± 7.7905	54.2614* ± 7.5258	52.5364* ± 5.3229	54.9867* ± 5.9797	51.7184* ± 8.0666	53.4764* ± 7.4578
ODI	0.2688 ± 0.1560	0.2668 ± 0.1507	0.1161 ± 0.0704	0.1224 ± 0.0755	0.2263 ± 0.1469	0.2426 ± 0.1445	0.2711 ± 0.1565	0.2625 ± 0.1575	0.1134 ± 0.0712	0.1303 ± 0.0840	0.2330 ± 0.1522	0.2326 ± 0.1522
ICVF	0.4807* ± 0.1431	0.5123* ± 0.1371	0.6821* ± 0.0945	0.6861* ± 0.0857	0.5090* ± 0.1519	0.5381* ± 0.1395	0.4908* ± 0.1256	0.4913* ± 0.1220	0.6786* ± 0.0946	0.6798* ± 0.0819	0.5150* ± 0.1345	0.5170* ± 0.1292
ISOVF	0.1389* ± 0.2137	0.1594* ± 0.2350	0.0937* ± 0.0599	0.0839* ± 0.0613	0.1745* ± 0.2310	0.1603* ± 0.2345	0.1483* ± 0.2256	0.1342* ± 0.2103	0.0990* ± 0.0608	0.0795* ± 0.0512	0.2010* ± 0.2486	0.1451* ± 0.2141

Table 5.7 | Values provided by the along-tract analysis of fractional anisotropy (FA), mean diffusivity (MD), mean square displacement (MSD), (square-root of) return to axis probability (RTAP), (cube-root of) return to origin probability (RTOP), return to plane probability (RTPP), orientation dispersion index (ODI), intracellular volume fraction (ICVF) and isotropic volume fraction (ISOVF) along the and corpus callosum (CC) - homologous connection between motor cortices, taking into account three different sections (start, middle, end) of this white matter tract. Each value represents the average value of each microstructural parameter ± the standard deviation associated, across the TLE patients and healthy controls. The level of significance is represented by one star (*) where the *p-value* is lower than 0.01 (i.e. difference between groups with statistical relevance). The units of MD and MSD are mm^2/s, and RTAP, RTOP and RTPP are given by mm^{-1}.

	Corpus Callosum					
	Near the cortical region of the left hemisphere		*At the level of the mid-sagittal plane*		*Near the cortical region of the right hemisphere*	
	TLE	Controls	TLE	Controls	TLE	Controls
FA	0.2963 ± 0.1204	0.2985 ± 0.1162	0.6927* ± 0.1309	0.7233* ± 0.1194	0.3047 ± 0.1272	0.3071 ± 0.1208
MD	0.000702* ± 0.000072	0.000698* ± 0.000060	0.000893* ± 0.000225	0.000867* ± 0.000197	0.000701* ± 0.000083	0.000699* ± 0.000074
MSD	0.000138* ± 0.000011	0.000137* ± 0.000010	0.000168* ± 0.000028	0.000165* ± 0.000027	0.000139* ± 0.000013	0.000137* ± 0.000012
RTAP	598.4324* ± 32.7645	599.6507* ± 29.9888	620.2166* ± 52.7702	634.6519* ± 45.0439	601.3572* ± 34.6726	601.5763* ± 31.1330
RTOP	70.9901* ± 2.5994	71.0904* ± 2.3753	72.6666* ± 4.1741	73.8088* ± 3.5241	71.2244* ± 2.7469	71.2352* ± 2.4671
RTPP	59.6081 ± 3.5765	59.6751 ± 3.1194	43.8233 ± 4.1910	43.8790 ± 4.0988	59.3904 ± 3.8498	59.4631 ± 3.3695
ODI	0.3572 ± 0.1307	0.3533 ± 0.1220	0.0882 ± 0.0771	0.0764 ± 0.0692	0.3454 ± 0.1323	0.3444 ± 0.1230
ICVF	0.4550* ± 0.0618	0.4568* ± 0.0561	0.5894* ± 0.1204	0.6339* ± 0.1096	0.4623* ± 0.0649	0.4631* ± 0.0583
ISOVF	0.0155 ± 0.0343	0.0138 ± 0.0331	0.2102 ± 0.1461	0.0216 ± 0.1429	0.0224 ± 0.0480	0.0189 ± 0.0466

5.3 Discussion

Diffusion imaging tractography is a valuable tool for neuroscience researchers because it allows the generation of individualized virtual dissections of major WM tracts in the human brain. With most of the tractography studies using a "tract-averaged" approach to analyse by averaging the scalar values from the many streamline vertices in a tract dissection into a single point-spread estimate for each tract, there is a growing interest in methods that can provide greater within-tract detail since it is well known that there is a prominent variation in diffusion imaging metrics within tracts.

In this study, a complete workflow used to conduct an along-tract analysis of WM pathways and integrate multiple microstructural scalar maps is described, based on the technical facilities of MRtrix and the visualization tools available through MATLAB for graphic computing.

5.3.1 Single-subject analysis: normal region *versus* complex region

Figure 5.4, **Figure 5.5** and **Table 5.1 – 5.3** demonstrate the effectiveness of such an along-tract approach in an example analysis of three major WM tracts (arcuate fasciculus, corticospinal tract and corpus callosum - homologous connection between motor cortices) in a single subject with TLE. By having into account the potentially rich anatomical variation in diffusion imaging metrics along the tracts, this approach allows to see the extent of within-tract variability of each scalar map without compressing all the microstructural information in one averaged diffusion metric for the WM tract in study.

Beyond the true biological variation in diffusion properties along tracts, we show that this technique allows a more detailed analysis of small ROIs extracted from the whole tract in order to avoid fibres from the WM pathways in the neighbourhood, which might lead to equivocal biological interpretations of the microstructural parameters. Consequently, such type of analysis can be also used to address some types of partial volume effects by checking the along-tract streamline distribution from complex fibre geometries with multiple fibres populations as the centrum semiovale (a region with crossing fibres from the arcuate fasciculus, corticospinal tract and corpus callosum) where microstructure properties may be also altered due to methodological issues. Therefore, the application of this along-tract technique can be used to highlight crossing fibres areas that are not resolved by the single tensor model of diffusion.

Looking at the results it was also verified that this method shows to reveal significant along-tract variations in each microstructural parameter for all of the major WM tracts studied, as would be expected based on previous voxel-based studies of the WM ((Schmithorst & Yuan, 2010) [123]; (Wozniak & Lim, 2006) [124]), and other tract-based approaches ((Concha *et al.*, 2010) [125]; (Davis *et al.*, 2009) [126]; (Sullivan & Pfefferbaum, 2006) [127]; (Xue *et al.*, 1999) [128]; (Yushkevich *et al.*, 2008) [129]).

In order to evaluate the structural changes that could be caused in the brain, one must have in mind is the pathophysiological effect of TLE in WM organization, since this neuropathological condition changes the microstructural environment (e.g., neuronal swelling or shrinkage, increased or decreased extracellular space and loss of tissue organization), which consequently result in altered diffusion and/or anisotropy along the WM pathways (graphic results illustrated by **Figure 5.4** and **Figure 5.5**). Patients with TLE suffer from dysfunctions affecting large-scale brain networks, which involves temporal and extratemporal regions of both hemispheres (Fahoum *et al.*, 2012) [130], rather than a single focal region (Laufs, 2012) [131]. Therefore, evaluation of WM tracts connecting these various affected regions may provide useful information as to pinpoint the origin of these diffuse changes in the brain that accompany TLE.

As a unique source of information about the underlying tissue structure of brain WM *in vivo*, DTI provides information regarding the geometry of major fibre bundles as well as quantitative

information about tissue properties represented by derived tensor measures, such as MD (used to measure the orientationally averaged diffusivity) and FA (which tells the degree of diffusion anisotropy). In fact, studies using DTI have consistently revealed bilateral patterns of microstructural damage to multiple long-range association tracts, with greater compromise to fibre tracts ipsilateral and proximal to the seizure focus ((Ahmadi *et al.*, 2009) [132]; (Otte *et al.*, 2012) [133]; (Concha *et al.*, 2012) [134]). This is typically demonstrated by decreases in FA and/or increases in MD along entire fibre tracts or within subsections of a tract, which are interpreted as reflecting axonal loss and demyelination of WM within the affected regions.

Despite the unique insights obtained from DTI, it is increasingly appreciated that FA and MD are nonspecific measures of cerebral pathology that are influenced by a number of tissue-related factors. For example, in addition to axonal loss and demyelination, decreases in FA may reflect the presence of crossing fibres or increases in extracellular diffusion due to oedema or inflammation ((Pasternak *et al.*, 2012) [135]; (McDonald *et al.*, 2013) [136]). Recent studies suggest that inflammation may play a role in the pathogenesis of TLE, which allows to better understand the neurobiology of decreased FA in temporal and extratemporal regions, helping to improve the treatments in patients with TLE (French *et al.*, 2016) [137].

However, the assumption of a Gaussian spin displacement distribution underlying DTI often renders the pathophysiological interpretation of changes in FA and MD problematic. Consequently, and aiming to assess brain tissue microstructure through microanatomical parameters that have higher sensitivity and specificity than DTI-derived parameters, a quantitative physical and mathematical framework was recently proposed, the MAP-MRI, which is able to compute some associated microstructural parameters: MSD, RTAP, RTOP and RTPP.

The mean square displacement travelled by a particle following a random walk is represented by MSD, which is proportional to the average amount of diffusion. Used to characterize cell mobility, MSD can be related to MD via the Einstein equation. Regarding the family of zero displacement probability measures, the contrast between single-fibre WM and regions with crossing fibres can be described by RTAP, which is in theory the integrated probability that a spin diffuses along the axis of the axons. RTOP gives the value of the propagator in the origin, which is considered to be proportional to the level of restricted diffusion, reflecting the cellularity and restrictions in diffusion. Lastly, as a directional index, RTPP quantifies the probability that a proton will be on the plane perpendicular to the main eigenvector of the diffusion tensor during both gradient pulses.

Additionally, as the DTI model also fails to account for the dispersion of axonal orientation, by assuming a single orientation within each voxel, NODDI aims to introduce a model sufficient to capture the morphology of neurites *in vivo* whilst ensuring that it remains simple enough to be acquired in a clinically feasible duration. This multi-compartment diffusion model is able to provide specific indices of tissue microstructure such as ODI, ICVF and ISOVF, which were obtained via the AMICO framework.

The dispersion of the neurite structures is further characterised by ODI which reflects the spatial configuration of the neurite structures, with small values of ODI corresponding to highly aligned axons (e.g. WM tracts). On the other hand, ICVF represents the space bound within the neuronal membrane, acting as a marker of neuronal density and taking its highest values in the major WM tracts, such as the corpus callosum. Through the ISOVF maps it is possible to highlight the ventricles and surrounding CSF that have a very high isotropic diffusivity. One previous study done by Loi *et al.* (2016) [138] revealed that reduced FA in the temporal lobes was primarily driven by reductions in intracellular diffusion, commensurate with neurite loss (i.e., cell and axonal or myelin loss), whereas reduced FA in extratemporal regions was also driven by fibre orientation changes (i.e., high ODI), potentially reflecting disorganized fibre orientation and packing.

Anatomically, the arcuate fasciculus is designed as a bundle of axons that connects caudal temporal cortex and inferior parietal cortex to locations in the frontal lobe. Across the TLE population in study and following the posterior – anterior direction, this WM pathway shows lower FA values (left: 0.3326 ± 0.1342; right: 0.3414 ± 0.1068) at the level of the Broca's area in the frontal lobe, with a small increase (left: 0.4756 ± 0.1059; right: 0.4964 ± 0.1119) as this tract goes into the parietal lobe, until a subtle decrease (left: 0.3943 ± 0.1192; right: 0.3832 ± 0.1206) occur at the Wernicke's Area. On the other hand, a slightly initial decrease of MD values was observed along the WM fibres of the arcuate fasciculus with the lower values (left: $(5.939 \pm 0.326) \times 10^{-4}$; right: $(5.964 \pm 0.353) \times 10^{-4}$) being reached at the level of the Geschwind's territory (due to a reduction in diffusivity perpendicular to the direction of the WM tract, which may indicate changes associated to the axonal width and/or the myelination process as Hüppi and Dubois (2006) [139] made reference), followed by an increase of MD values. Regarding *the q-space* indices, minimal changes were registered for MSD along the arcuate fasciculus, with the values varying around approximately $(1.355 \pm 0.072) \times 10^{-4}$ (left) / $(1.327 \pm 0.056) \times 10^{-4}$ (right). By analysing the graphic results for RTAP, RTOP and RTPP, the values changed according to what was expected, since the highest values (left: 672.7215 ± 17.3365, 76.7700 ± 1.3247, and 61.2225 ± 4.1840, respectively; right: 672.5108 ± 18.9524, 76.7529 ± 1.4441, and 60.1803 ± 4.5375, respectively) correspond to the Gesehwind's territory, region with a higher level of restricted diffusion and comprised by complex fibres orientations distributions due to the proximity to the centrum semiovale, known as crossing region with multiple fibres population. From **Figure 5.4**, **Figure 5.5** and **Table 5.1**, it also can clearly be seen that ODI values started around 0.3288 ± 0.1312 (left) / 0.3137 ± 0.1012 (right), followed by a decrease and a minimal increase at the level of the Geschwind's territory (left: 0.2132 ± 0.1061; right: 0.1976 ± 0.1034), which can be explained by the presence of fibre crossings and fanning fibres, or might be a result from the high tract curvature in this region. Then the ODI values decrease again and near the Wernicke's area they achieved higher values (left: 0.2718 ± 0.1046; right: 0.2872 ± 0.1043) similar to the starting values. The results for ICVF and ISOVF suggest that the higher values (left: 0.6149 ± 0.0452, and 0.0488 ± 0.0232, respectively; right: 0.6182 ± 0.0500, and 0.0538 ± 0.0231, respectively) also correspond to the Geschwind's territory. However, due to the complexity of fibres architecture that it is present in this region, the result regarding ICVF was unexpected since higher values are achieved in regions with highly anisotropic coherent single fibres, which does not occur in the Geschwind's territory. Particularly and although this TLE patient has being diagnosed with a left focused TLE, the variation of all the microstructural parameters along the arcuate fasciculus in study was similar between both hemispheres, which could be explained by the bilateral patterns of microstructural damage usually observed in previously studied cases.

The corticospinal tract ascends from the brainstem, paralleling the ventricles to the cortex. Analysing the results (**Figure 5.4**, **Figure 5.5** and **Table 5.2**), FA starts off relatively low (left: 0.4126 ± 0.1644; right: 0.4212 ± 0.1579) due to partial voluming in the brainstem, then FA peaks roughly half way (left: 0.6999 ± 0.1072; right: 0.7228 ± 0.1042) and MD assumes its lower values (left: 0.0005862 ± 0.0000475; right: 0.0006072 ± 0.0000714) at the level of the internal capsule, where the fibres are coherently oriented inferior-superior; followed by a briefly decrease of FA at the level of the centrum semiovale, a location where colossal fibres cross medial to lateral through the corticospinal tract and SLF fibres cross posterior to anterior through the corticospinal tract. Before arriving at the motor cortex, FA assumes low values (left: 0.4315 ± 0.1605; right: 0.4381 ± 0.1529), which were similar to the values initially taken at the level of the brainstem. Additionally, no major differences were registered for MSD along the corticospinal tract, with the values oscillating around approximately $(1.495 \pm 0.286) \times 10^{-4}$ (left) / $(1.438 \pm 0.246) \times 10^{-4}$ (right). For RTAP and RTOP, the higher values (left: 708.4938 ± 21.8747, and 79.4652 ± 1.6516, respectively; right: 706.0574 ± 30.3871, and 79.2746 ± 2.3057, respectively) were found at the level of the internal capsule, where the fibres are coherently oriented inferior-superior and, consequently, a huge level of restricted diffusion is observed. Based on this and

as expected, RTPP starts off relatively low (left: 52.7403 ± 7.6897; right: 54.1549 ± 7.2574) due to partial voluming that exists in the brainstem, then after a brief increase, RTTP values decrease (left: 53.5081 ± 5.3737; right: 52.1260 ± 5.9923) at the level of the internal capsule, where the fibre bundles are coherently oriented. Due to the approximation to the centrum semiovale, the configuration of the neurite structures tend to disperse. Consequently, RTPP values increase, followed by a reduction (left: 52.5388 ± 7.5503; right: 54.1482 ± 6.5715) just before the motor cortex bas been reached. Regarding the NODDI parameters, ODI values were around 0.2655 ± 0.1655 (left) / 0.2389 ± 0.1686 (right) in the brainstem, followed by a brief decrease, which was immediately followed by a slightly increase until the lowest values (left: 0.1034 ± 0.0566; right: 0.0947 ± 0.0516) being reached at the level of the internal capsule, where the fibres are highly aligned. Then, close to centrum semiovale, ODI increases due to the highly dispersed spatial configuration assumed by regional neurites, value that tend to decrease (left: 0.2477 ± 0.1630; right: 0.2217 ± 0.1492) again at the level of the motor cortex. The results for ICVF suggest that the highest values (left: 0.7339 ± 0.0684; right: 0.7166 ± 0.0822) correspond to the internal capsule, where the fibres are highly aligned, so the neuronal density is elevated. According to the changes observed with ISOVF, no major differences were registered, maintaining a value of approximately 0.1198 ± 0.1460 (left) / 0.0779 ± 0.1098 (right) constant along the whole tract. This WM pathway also showed microstructural change patterns without major differences across the TLE population in study, with similar variations at equivalent locations in all individuals, achieving at those points similar levels in each subject's hemisphere.

The corpus callosum (**Figure 5.4**, **Figure 5.5** and **Table 5.3**) shows a twofold decrease in FA as the fibres traverse away from the mid-sagittal plane. This symmetric parasagittal dips in FA along the corpus callosum likely result from partial volume averaging with CSF in the adjacent lateral ventricles (Jones *et al.*, 2005) [140], which leads to maximum values of MD ($(8.155 \pm 1.455) \times 10^{-4}$) registered in this region. Along the colossal segments FA takes high values near the mid-sagittal plane, where colossal fibres are tightly bundled together and coherently organized in the medial-lateral direction; consequently, a reduction of MD values is observed. Then, FA decreases substantially (right: 0.2964 ± 0.1277; left: 0.2489 ± 0.1159) and MD slightly increases (right: $(6.869 \pm 0.674) \times 10^{-4}$; left: $(7.427 \pm 1.453) \times 10^{-4}$) as fibres start diverging toward their specific cortical destinations, along the homologous regions of left and right hemisphere. Associated to MD, the MAP-MRI parameter MSD registered a slight increase of its values ($(1.575 \pm 0.230)) \times 10^{-4}$) on the mid-sagittal plane due to the partial volume effect derived from the presence of CSF on the lateral ventricles, which justifies the fact that here, RTAP, RTOP and RTPP assume lower values (635.0490 ± 43.1766, 73.8430 ± 3.3880, and 45.1417 ± 4.8397, respectively), since this is a WM region where the level of restricted diffusion is attenuated and the spatial configuration of the fibres assume an architecture similar to a highly anisotropy coherent single fibre. Consequently, as expected, near the mid-sagittal plane it also can clearly be seen that the lowest ODI values (0.0844 ± 0.0735) were registered, as well as the higher values of ICVF and ISOVF (0.6232 ± 0.0844, and 0.1766 ± 0.1165, respectively), due to an increase of the neuronal density and from the possible CSF contamination, respectively. As was verified on arcuate fasciculus and corticospinal tract, the variation of all the microstructural parameters along the corpus callosum was similar across all the TLE patients in study, despite they have been diagnosed with different neurological conditions derived from TLE.

Having in mind the magnitude of the recorded values along the ROIs extracted from each of the WM tracts of interest and looking in detail to the along-tract analysis performed on the centrum semiovale (**Figure 5.4**, **Figure 5.5** and **Table 5.4**), it was determined that the application of multiple diffusion approaches was proven feasible and its derived microstructural parameters demonstrated to be in general sensitive biomarkers with increased pathophysiological specificity.

The centrum semiovale, as a region containing complex WM configuration, showed lower FA values (right: 0.4159 ± 0.1060 - 0.4640 ± 0.0994; left: 0.4368 ± 0.1183 - 0.5145 ± 0.1097) and relatively

higher MD values (right: (5.700 ± 0.181 - 5.852 ± 0.328) × 10^{-4}; left: (5.983 ± 0.338 - 6.191 ± 0.571) × 10^{-4}). However, when interpreting diffusion parameters provided by DTI, the dispersion of fibre orientations is known to be a critical factor, limiting the interpretation of the derived parameters for fibre integrity in crossing fibre regions ((Jones, 2010) [141]; (Wheeler-Kingshott *et al.*, 2009) [142]; (Grinberg *et al.*, 2016) [143]). Nevertheless, these results are in line with previous diffusion studies, which showed low anisotropy at the level of the centrum semiovale ((Groeschel *et al.*, 2014) [144]; (Hervé *et al.*, 2011) [145]; (Reich *et al.*, 2006) [146]). Related to MD, an average amount of diffusion represented by MSD was registered, achieving higher values (right: (1.341 ± 0.036 - 1.349 ± 0.049) × 10^{-4}; left: (1.356 ± 0.046 - 1.377 ± 0.080) × 10^{-4}) and without significant variations along this WM region characterized by a complex fibre architecture, which consequently is correlated to the highest values that were observed for RTAP (right: 675.4714 ± 20.1501 - 681.6977 ± 10.7638; left: 661.9629 ± 30.0824 - 667.8986 ± 17.9269), RTOP (right: 76.9771 ± 1.5357 - 77.4550 ± 0.8153; left: 75.9371 ± 2.3198 - 76.4021 ± 1.3714) and RTPP (right: 61.9657 ± 4.2052 - 63.6928 ± 4.1299; left: 61.7158 ± 4.2187 - 58.4471 ± 3.6543). Regarding quantitative measures derived from NODDI, where FA is low, ODI shows higher values (right: 0.2208 ± 0.1072 - 0.2692 ± 0.1073; left: 0.1759 ± 0.0836 - 0.2391 ± 0.1068), reflecting the crossing of many axons, whereas ICVF remains high throughout (right: 0.6283 ± 0.0525 - 0.6463 ± 0.0301; left: 0.5929 ± 0.0695 - 0.6084 ± 0.0432) and ISOVF relatively low (right: 0.0575 ± 0.0234 - 0.0681 ± 0.0265; left: 0.0559 ± 0.0233 - 0.0626 ± 0.0226). Additionally, we can also say that the ICVF parameter was less influenced by the spread of fibre orientation, better reflecting the integrity of WM pathways in crossing fibre regions, as was recently shown by others studies and underlined by histology (Sepehrband *et al.*, 2015) [147].

5.3.2 Between-group analysis: TLE patients *versus* healthy controls

This technique was easily extended to between-group analysis (**Figure 5.6**, **Figure 5.7** and **Table 5.5 – 5.7**) which is typically used in neuroscience applications, by conducting an along-tract analysis of differences in multiple microstructural parameters between 9 patients with TLE and 9 healthy controls. This analysis aims to reveal localized differences between TLE and control group that possibly were not evident using a tract-averaged method.

Diffusion can be characterized using scalar quantities such as MD and FA, which have demonstrated high sensitivity to pathological changes. In epilepsy, increased diffusivity and reduced diffusion anisotropy were associated to the diagnosis of this neuropathological condition, suggesting a loss of structural organization and expansion of the extracellular space (Wieshmann *et al.*, 1999) [148].

As expected, the results suggest a significant decrease of FA on the left and right arcuate fasciculus in the TLE patients compared to the controls. Also a slight decrease of FA values were detected in the brainstem and close to the motor cortex along the corticospinal tract in both hemispheres of the TLE patients, with a brief decrease also being verified near the mid-sagittal plane of the corpus callosum. This result is in concordance with the literature findings, since with a lower degree of anisotropy diffusion due to the destruction of axons associated to a diagnosis of TLE, which may lead to a disorganization of the fibres orientation, FA tends to decrease. However, it is also important to highlight the fact that these achievements were quantified in WM pathways involved in different human capacities such as language, motor, sensory or cognitive functions, which allow us to conclude that these WM tracts, as extratemporal WM tracts, can also be affected. Associated to the neuronal loss, which is the most common histologic finding in patients with TLE, a significant increase in MD within the WM in the arcuate fasciculus (both hemispheres) was demonstrated compared to the control group. Along the left/right corticospinal tract and the corpus callosum, the same was verified, however with less difference between the two groups.

Additionally, the *q-space* indices were calculated in order to describe the properties of the brain tissue microstructure using MAP-MRI. With this in mind, the MSD values, which are used to characterize cell mobility, showed the expected variation, with TLE patients being characterized by higher values when compared to healthy controls along the WM pathways in study. However, it can be observed that the major difference between the two groups was verified on the left and right arcuate fasciculus. The contrast between single-fibre WM and regions with crossing fibres is described by RTAP. Based on this and since with this neuropathological condition the level of restricted diffusion tend to reduce with the neuronal destruction, lower RTAP values were observed in TLE patients along all the WM pathways of interest. Although, along the left and right corticospinal tract the differences were almost insignificant between the TLE patients and the control group. With the loss of axons and as a microstructural parameter proportional to the level of restricted diffusion, RTOP proved to take the lowest values along the WM tracts of the TLE patients' brain as the diffusion tends to become less anisotropic. It was also verified that this diffusion parameter shows a spatial variation of its values along the WM tracts very similar to RTAP. The results also suggest that minimal differences were found for RTPP along the WM pathways of the TLE patients compared to healthy controls, which might be associated to a reduction on the complexity of the FODs. Despite RTPP assume lower values along the left/right arcuate fasciculus and left/right corticospinal tract of TLE patients, a smaller variation was displayed across the corpus callosum between the two groups, with no statistically significance being observed.

Nevertheless, a more detailed tissue characterization based on MAP-MRI parameters was obtained, reflecting the physically meaningfulness of these microstructural features with greater neuroanatomical specificity along the tracts. For example, we show that the arcuate fasciculus is microstructurally abnormal bilaterally despite the unilateral TLE diagnosed in these patients. And, RTAP and RTOP showed an increased difference within the corpus callosum between the two groups compared to the along-tract behaviour drawn by the FA profile, which highlights the biologically specificity of these tissue markers in pathologies characterized by neuronal reduction as TLE.

Then, as explained before, we used NODDI in order to provide more specific indices of tissue microstructure. In **Figure 5.7** and based on the along-tract variation of the ODI values, it can clearly be seen that major differences with statistical relevance between the two groups were not detected, except for the left arcuate fasciculus. However as index associated to the spatial configuration of the neurite structures, larger values of ODI were expected to be registered for TLE patients characterized by an increase of dispersed neurites, against the healthy controls. Through the graphic results we can also observe that the TLE patients showed significant lower values of ICVF when compared to healthy controls. Knowing that ICVF acts as a marker of neuronal density, we can affirm that the results illustrate the expected difference in the presence of neurological condition as TLE. Focusing on the results about ISOVF no major differences were found between the two groups, with the values assumed by this microstructural parameter being similar for TLE patients and healthy controls. However and as an exception, the results for left and right corticospinal tract showed a minimal difference with statically significance between the two groups. Higher values were observed along the WM fibres of this WM pathway in both hemispheres of the neuropathological group when compared to the control group. Nevertheless, higher ISOVF values were expected to be verified along all the WM pathways of the TLE patients when compared to the healthy controls, which was just observed with statistical relevance along the left and right corticospinal tracts.

In summary, the results showed increased diffusivity and reduced anisotropy, suggesting a loss of structural organization and expansion of the extracellular space with TLE, both locally and in extratemporal tracts despite the left epileptic focus, which agrees with the concept that epilepsy is a network disorder.

5.3.3 Final remarks

With this study interesting results about the along-tract analysis of WM pathways were achieved, focusing on the within-tract variability of the microstructural parameters that exists along tracts and highlighting its feasibility and potential benefits for clinical purposes based on the increased pathophysiological specificity. Specifically, by doing this analysis we also show that a more detailed tissue characterization could be obtained through the study of more advanced microstructural parameters derived from MAP-MRI and NODDI along the WM tracts, which reflect the greater neuroanatomical specificity of these microstructural features along the tracts and reveal to be a powerful outcome to overcome the well-known limitations of tensor derived metrics regarding their interpretation.

Alternatively, we showed that this analysis could also be limited to more specific portions of the tract(s), which could be performed by extracting a spherical subsection of the tract(s), allowing a restricted along-tract analysis to only the high confidence central portion from a tract, or to a complex region with multiple fibre populations, where the averaged-tract approaches tend to outcome critical conclusions about the diffusion process. Nevertheless, it is important to recognize that this along-tract technique had some limitations.

This analysis is based on the reconstruction of WM pathways generated by tractography. Even though as a technique that can circumvent some of the issues of traditional voxelwise registration (since the tract groups are individualized dissections based on the WM anatomy of each subject), tractography suffers from some limitations, as it is indirect, inaccurate, and difficult to quantify (Jbabdi & Johansen-Berg, 2011) [110]. Discrepancies between the scale of the axonal diameter and the imaging voxel size (i.e., low spatial resolution), the noise contained in the diffusion data, and image artefacts comprise most of the limitations associated with tractography. Other limitations include the inability to distinguish afferent from efferent connections, to detect the presence of synapses, or to determine whether a pathway is functional ((Campbell & Pike, 2014) [149]; (Ciccarelli *et al.*, 2008) [150]; (Johansen-Berg & Behrens, 2006) [151]). Several tractography algorithms have been described but there is no consensus on which is the most effective since this is a technique sensitive to a large array of user-definable or algorithm-specific parameters (Lazar & Alexander, 2003) [152]. Thresholds and other parameters of tractography need to be optimised, which is likely to lead to disagreements among researchers. Despite this, diffusion MRI tractography can contribute significantly to basic and clinical neuroscience research but its limitations must be clearly understood and considered when interpreting results.

On the other hand, as it is referred in Tariq *et al.* (2012) [153], although both NODDI and DTI probe microstructure from the diffusion of the water molecules within the brain, DTI is limited in its ability to provide information about the specific changes in microstructure; the indices obtained are affected simultaneously by a number of microstructural changes (e.g. demyelination, inflammation, axonal loss, gliosis), which give rise to the same alterations of their values. In order to overcome this limitation, higher-order models of diffusion have been developed. NODDI estimates the microstructure directly, using an analytical model relating these parameters to the diffusion MRI signal. However, as parametric diffusion model, NODDI relies on *a priori* assumptions about the tissue microstructure. In contrast, the non-parametric framework of MAP-MRI can efficiently measure the PDF of spin displacements and it is able to quantify useful metrics of this PDF indicative of diffusion in complex microstructure (e.g., restrictions, multiple compartments), as Avram *et al.* (2016) [92] made reference. In particular, the along-tract analysis of MAP-MRI parameters show significant microstructural brain tissue changes and are a useful adjunct to conventional DTI parameters.

Finally, it was used a “constant number of points” approach to resample streamlines because it is simple and allows the straightforward between-group analysis since every subject's tract data will have a one-to-one mapping along the streamlines. However, each streamline has a different length, and despite the requirements indicated for the tracking regarding the minimal length for a streamline to be included in the reconstruction of the WM tract of interest, the control of the inter-subject variation

regarding the tract length, as well as between streamlines of one tract, is not possible. Consequently, even with the same number of points resampled along each streamline for a WM pathway in study, the spatial match cannot be guaranteed. So, it is clear that this decision could be more appropriate for some tract geometries than others, and suggests that this method will be best suited for WM tracts that are comprised by relatively long fibres and restricted to relatively tube-like point-to-point trajectories between functional or anatomical regions, against short WM tracts or those where there is little directional changes along its length.

Despite all the limitations associated to this analysis, which were previously mentioned, with this study we have shown that by implementing a relatively simple along-tract analysis workflow, we might be able to answer questions in regard to fibre integrity or fibre disruption, associated to diffusion changes of WM tracts in the presence of pathology, and its effect on brain connectivity, which has proved to be an extremely important topic for clinical research over the last few years.

6 Tract-Based Spatial Statistics (TBSS)

6.1 Methods

TBSS [154, 155, 156], which uses non-linear image transformation, is a technique that combines the strength of both voxelwise and tractography-based analyses. Posteriorly, the TBSS method is explained, with a block diagram of this method being shown in **Figure 6.1**.

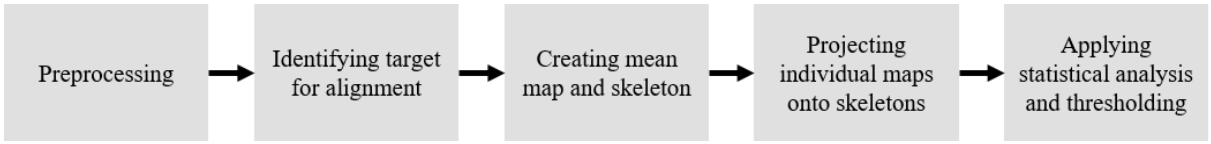

Figure 6.1 | Block diagram of TBSS method.

As a specific example of this analysis and its results, the TBSS analysis was applied to patients with a diagnosis of TLE with left epileptic focus (9 patients, 5 male, mean age 12 years, range 5 – 19 years), which were selected from our initial population in study, and compared to healthy controls (9 subjects, 5 male, mean age 12 years, range age 8 – 18 years).

With the FA data for the eighteen subjects generated since the first analysis, the first TBSS script (*tbss_1_preproc* command) was ran, which removed the brain-edge artefacts from the FA images and turned to zero the end slices (in order to remove outliers from the diffusion tensor fitting).

By running the next TBSS script (*tbss_2_reg* command using the *-n* flag option), a common registration target was identified as the "most representative" FA volume (i.e. the single individual target that minimises the amount of warping required for all other subjects to be aligned to it) [154] and, consequently all subjects' FA images were aligned to this target using nonlinear registration. So, this target image was then affine-aligned into MNI152 standard space, and every image was transformed into 1x1x1*mm* MNI152 space by combining the nonlinear transform to the target FA image with the affine transform from that target to MNI152 space.

The next step was running the *tbss_3_postreg* script, which applied those registrations to take all subjects into 1x1x1*mm* standard space. Afterward, all subjects' standard space nonlinearly aligned images were merged into a single 4D image file. As output, the mean of all aligned FA images was created, and by applying ''thinning'' methods (non-maximum-suppression perpendicular to the local tract structure), a skeletonised mean FA image (see **Figure 6.2**) was estimated, which represents the centres of all fibre bundles that are generally common to the subjects involved in the study. Regarding this mean FA skeleton, such is computed from the mean FA volume, by first estimate the local surface perpendicular to the tract directions and then by computing the centre of the tract using non-maximum-suppression. [154]

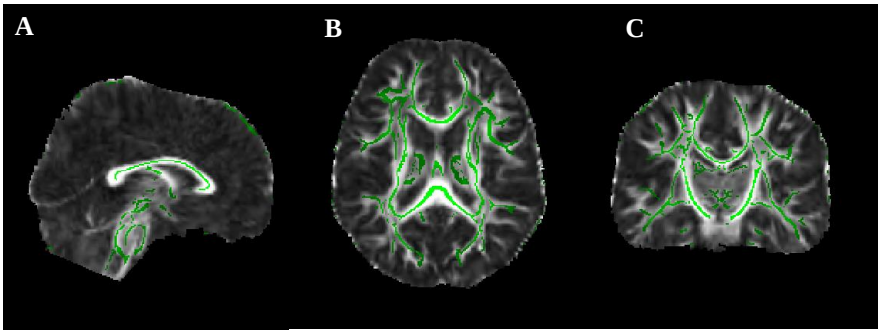

Figure 6.2 | Representation of the skeletonisation stage: original mean FA image with final skeleton at sagittal view **(A)**, axial view **(B)** and coronal view **(C)**.

The last TBSS script (*tbss_4_prestats* command) carried out the final steps necessary before running the voxelwise cross-subject stats. The mean FA skeleton image was thresholded to suppress areas of low mean FA and/or high inter-subject variability, and as ultimate goal to restrict the further analysis to voxels that only correspond to WM voxels that were successfully aligned across subjects. The threshold can be set as an input on the FSL script *tbss_4_prestats*. For the mean FA skeleton generated, the threshold was adjusted to a value of 0.3 once it shown to be an adequate value to select typical WM tracks in the studied subjects´ population.

From this step a binary skeleton mask was generated, which allowed to define the set of voxels used in all subsequent processing steps. Each subject's FA data was then projected onto the mean FA skeleton in such a way that each skeleton voxel takes the FA value from the nearest relevant tract centre. This was achieved, for each skeleton voxel, by searching perpendicular to the local skeleton structure for the maximum value in the subject's FA image.

TBSS allows also the projection of other invariant metrics to the skeleton. The script *tbss_non_FA* was used, given as input a folder containing all subject volumes for a specific metric. By running this script, the nonlinear registration (determined on TBSS, first and second steps) were applied to the non-FA data, which was followed by the projection of the maximum on the non-FA values on each individual skeleton. [156] On this study *tbss_non_FA* was applied to the preliminary study of microstructural changes on MD, MSD, RTAP, RTOP, RTTP, ODI, ICVF and ISOVF, between a control group and a group composed by patients with left TLE.

Having the individual skeletons, TBSS can finally be followed with the voxelwise statistics across subjects through the randomise tool [157] (with 500 permutations), by assuming two contrasts: *contrast 1* corresponds to the patient > control test, and *contrast 2* gives the control > patient test. In this study, it was tested the brain regions that shown significance increases and decreases in the presence of neuropathology as TLE, on FA, MD, MSD, RTAP, RTOP, RTPP, ODI, ICVF, and ISOVF scalar maps (with significances computed based on Threshold-Free Cluster Enhancement (TFCE) *p-values* [158]).

6.2 Results

By setting the colourmap and with the display ranging from 0.95 to 1, which corresponds to thresholding the results at $p < 0.05$, it was possible to analyse the results of this voxelwise statistics analysis. Two different contrasts regarding the microstructural scalar maps were assumed: *contrast 1* corresponding to the patient > control test, and *contrast 2* giving the control > patient test. Knowing that the skeleton that delineates the major WM tracts is shown in green, *blue – light blue* regions on the skeletons correspond to regions where increases of the microstructural parameters in study were significant (which were given by *contrast 1*), while significant decreases are shown in *red - yellow* (which were given by *contrast 2*).

Figure 6.3 shows the changes in FA, MD, MSD, RTAP, RTOP, RTPP, ODI, ICVF and ISOVF volumes along the WM skeleton of patients with left TLE compared with healthy controls.

Therefore, the results suggest an increase in MD and MSD along the WM skeleton of TLE patients compared with healthy controls, while a significant decrease was verified in FA, RTAP, RTOP, RTPP and ICVF skeletons. No significant changes of ODI and ISOVF were found in the TLE group.

TLE group exhibited widespread changes of the microstructural parameters along the WM tracts on frontal, parietal and temporal lobes. The location was consistent in the FA, MD, MSD, RTAP, RTOP and ICVF along the WM tracts, but significantly smaller in the RTTP volume along the corresponding areas identified.

Compared with healthy subjects, lower FA values were verified in TLE patients, with the same profile being demonstrated by RTAP, RTOP, RTPP and ICVF. In particular, FA and ICVF were shown to significantly decrease on the left and right arcuate fasciculus, genu and splenium of corpus callosum, and sporadically along the left and right corticospinal tract. The results of RTAP and RTOP skeletons

revealed the same decreasing pattern, which was visible along left and right arcuate fasciculus, genu and splenium of corpus callosum and along the left and right corticospinal tract. An occasionally decrease of RTPP was observed on the left and right corticospinal tract.

On the other hand, the spatial profile assumed by the increase of MD was evident on many brain-networks in both hemispheres, while the increasing spatial profile of MSD was observed having a special focus along left arcuate fasciculus and, occasionally, along the left corticospinal tract and splenium of corpus callosum.

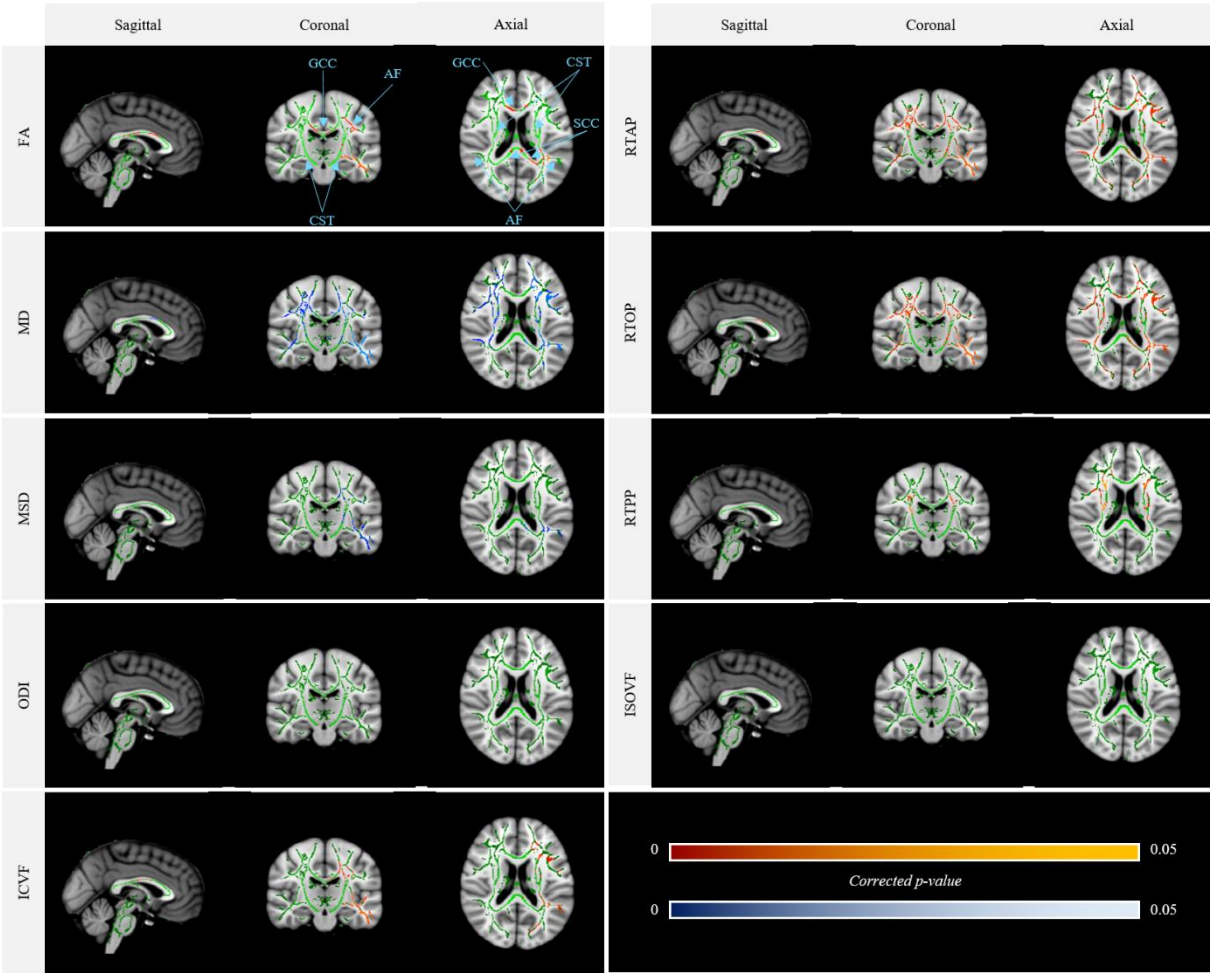

Figure 6.3 | TBSS of fractional anisotropy (FA), mean diffusivity (MD), mean squared displacement (MSD), square root of return to axis probability (RTAP), cube root of return to origin probability (RTOP), return to plane probability (RTPP), orientation dispersion index (ODI), intracellular volume fraction (ICVF), and isotropic volume fraction (ISOVF) skeletons along WM pathways and correlated with increases (coloured by blue to light blue) and decreases (coloured by red to yellow) on brain, displaying the results threshold at *p-value* < *0.05*. Compared with healthy controls, MD and MSD increase along the WM skeleton of TLE patients, while a significant decrease was verified in FA, RTAP, RTOP, RTPP and ICVF skeletons. ODI and ICVF changes are not evident within WM tracts between both groups. Abbreviations: AF - arcuate fasciculus, GCC - genu of corpus callosum, SCC - splenium of corpus callosum, CST - corticospinal tract.

6.3 Discussion

The purpose of this study was to investigate WM change patterns across the whole brain in patients with left TLE, and explore changes in multiple diffusion metrics (FA, MD, MSD, RTAP, RTOP, RTPP, ODI, ICVF and ISOVF), by applying a voxel-based technique, the TBSS. TBSS provides a powerful and objective method to perform multi-subject comparison, based on voxel-wise statistics of diffusion metrics but simultaneous aiming to minimize the effects of misalignment using a conventional voxel-based analysis method (Smith *et al.*, 2006) [154].

Shown in **Figure 6.3**, the results from this study indicate that the TLE patients, when compared to healthy controls, exhibited significantly reduced FA in widespread WM regions, which suggests that TLE is a disease that affects the brain globally, with same change pattern being showed by RTAP, RTOP, RTPP and ICVF. However, increase of MD and MSD was observed, with increases of MSD being exhibited significantly in the temporal lobe of left hemisphere. Furthermore, no significant changes of ODI and ISOVF were found in the TLE group.

This additional study also demonstrated that TLE was involved in diffusion changes of WM regions corresponded to a widespread network of WM tracts, including intrahemispheric fibre tracts, temporooccipital connections, frontotemporal connections or motor projection tracts, which is consistent with the findings of previous TBSS studies ((Zhenyin *et al.*, 2014) [159]; (Riley *et al.*, 2010) [160]; (Schoene-Bake *et al.*, 2009) [161]; (Focke *et al.*, 2008) [162]).

In particular, focusing this study just on the diffusion alterations along the arcuate fasciculus, corticospinal tract and corpus callosum, the following conclusions could be addressed. FA and ICVF showed to significantly decrease on the left arcuate fasciculus, genu and splenium of corpus callosum, and sporadically along the left and right corticospinal tract. The results of RTAP and RTOP skeletons revealed the same decreasing pattern, which was visible along left and right arcuate fasciculus, genu and splenium of corpus callosum, and along the left and right corticospinal tract. An occasional decrease of RTPP was also observed on the left and right corticospinal tract. On the other hand, the spatial profile assumed by the increase of MD was evident along all the WM pathways of interest in both hemispheres, while the increasing spatial profile of MSD was observed having a special focus along left arcuate fasciculus and, occasionally, along left corticospinal tract and splenium of corpus callosum.

These microstructural changes might reflect a combination of axon and myelin loss, therefore leading to lower membrane density and higher extracellular volume (Sen & Basser, 2005) [163]. However, it is important to note that the splenium of the corpus callosum showed decreased FA without significant changes in MD, which may reflect subtle WM fibre incoherence, such as minor fibre loss, as was previously mentioned by Riley *et al.* (2010) [160].

To the best of our knowledge, a study examining the WM changes in MSD, RTAP, RTOP, RTPP, ODI, ICVF and ISOVF in TLE patients compared to healthy controls has not been performed in humans so far. However, multiple studies have investigated human axonal and myelin degeneration in TLE patients based on the alterations observed in FA and MD, which allow us to justify the results achieved with this study in all microstructural metrics, since they are related to each other in some way through the diffusion alterations that arise from their increase or reduction comparing to the values assumed by healthy controls. With this in mind, we attempt to ensure which processes are exactly captured by the different metrics, so that we can choose the ones that best fit a specific pathology or, on the other hand, to tell us what extra analysis should be done, if we do not know the type of pathology. For example, by comparing TLE patients and healthy subjects, Arfanakis *et al.* (2002) [164] detected a significantly lower FA and higher MD in several WM structures of the TLE patients that were not located in the temporal lobes. In another study, Gross *et al.* (2006) [165] investigated the abnormalities of water diffusion in extra-temporal WM of patients with TLE. Results demonstrated reduced FA of the genu of the corpus callosum and external capsule and elevated MD of the genu, splenium, and external

capsule. Additionally, Petersen (2004) [166] identified a reduction of FA and elevation of MD on the hippocampus, temporal lobe, inferior frontal area, and arcuate fasciculus in TLE.

Besides the interesting results that were obtained with this additional analysis, it is important to note that these findings should be interpreted within the context of the following limitations.

First, Keihaninejad *et al.* (2012) [167] demonstrated the dependence of specificity and sensitivity of TBSS results on the registration target. Additionally, Van Hecke *et al.* (2010) [168] discussed potential pitfalls and limitations of TBSS, such as the assumption that the effect of interest occurs in voxels where the local FA is highest, since due to the skeletonization process, only the voxels with maximum FA values are included in the final skeletonization process. Consequently, TBSS is only able to tell about the statistical difference in voxels with highest FA at any given location without any specificity regarding specific part of that region on that plane.

Second, with an averaging of values across all the subjects, any extreme outlier can substantially affect the group level result. With this in mind, it is clear that further studies are required in order to elucidate the relationship between axonal changes and TBSS findings in TLE patients.

Finally, there was not any information available regarding the subjects' exposure to anti-seizure medications, but knowing that the use of the majority of these drugs has been associated with cerebellar atrophy, their impact on cerebral WM was not taken into account. However, the use of such medications could help to justify some of the results obtained in this study.

Notwithstanding these limitations, the results from this study indicate that TLE is characterized by a combination of axon and myelin loss, which was proved based on the various WM change patterns showed by FA, MD, MSD, RTAP, RTOP, RTPP, ODI, ICVF and ISOVF, when compared to healthy controls.

7 Fixel-Based Analysis (FBA)

FBA [117, 169] defines fixel as a single fibre population within a voxel. This novel quantitative framework aims to study WM by discriminating between alterations in WM (see **Figure 7.1**) due to microstructural abnormalities (alterations in fixel-specific fibre density, FD) and morphological changes (alterations in fibre cross-section, FC), and combined microstructural and morphological changes (alterations in fibre density and cross-section, FDC).

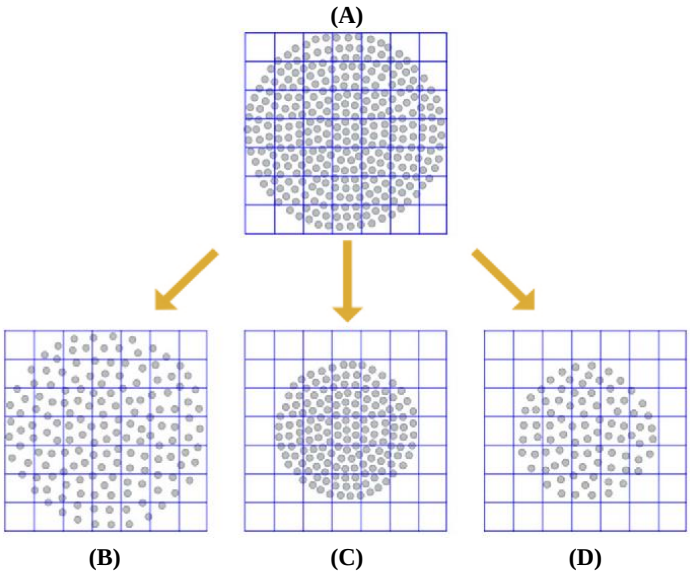

Figure 7.1 | (A) Schematic representation of a fibre bundle cross-section (grey circles represent axons, while the grid represents imaging voxels). A change to the intra-axonal volume (and therefore 'ability to relay information') may manifest as: **(B)** changes in tissue microstructure that result in a change in within-voxel fibre density; **(C)** a macroscopic difference in a fibre bundle's cross-section; or **(D)** a combination of both fibre density and bundle cross-sectional area. Adapted from [169].

Our aim with this additional analysis was to establish the utility of FBA in TLE patients, which may provide unique complementary information based on the metrics generated and associated to this framework, highlighting potential differences between TLE patients and healthy controls.

7.1 Methods

With the aim to demonstrate how a comprehensive FBA of FD, FC and FDC may provide unique yet complementary information to this study, a FBA was done comparing TLE patients to healthy controls. However, note that for this specific analysis and as an example of its results, the focus were patients with a diagnosis TLE with left epileptic focus (9 patients, 5 male, mean age 12 years, range 5 – 19 years), which were selected from our initial population in study, and compared to healthy controls (9 subjects, 5 male, mean age 12 years, range age 8 – 18 years).

The FBA [169] starts by generating a group average response function using the response functions computed per subject on the first analysis. By using the same response function when estimating FOD images for all subjects, we could ensure that there are not differences in the intra-axonal volume (and therefore diffusion-weighted signal) across subjects that can be detected as differences in the FOD amplitude (the Apparent Fibre Density, AFD).

This step was followed by the upsampling of the dMRI data and correspondents brain masks calculated before (using the *mrresize* command of MRtrix) to a voxel size of 2.00 *mm*, with the purpose of increase the anatomical contrast and improve the downstream spatial normalisation and statistics.

Using the group average response functions, CSD was performed, by running the *dwi2fod* command, to estimate the FOD per subject.

After this, the *mtnormalise* command was applied with the aim of scaling all tissue types with a spatially smoothly varying normalisation field, which allows to achieve the global intensity normalisation in the log-domain, but also to further correct the (residual) intensity inhomogeneities.

The next step of FBA consists of generating an unbiased FOD template by running the *population_template* script. Starting with a rough alignment via the centre of mass of the images as initial template, *population_template* registers and transforms all subjects to this current best estimate of a population template. This template is iteratively updated with the transformed and averaged images, which build the basis for the next template iteration. With increasing iteration count, the degree of freedom of the transformation (rigid, affine, nonlinear) and the spatial and angular resolution are increased (see **Figure 7.2**). [117]

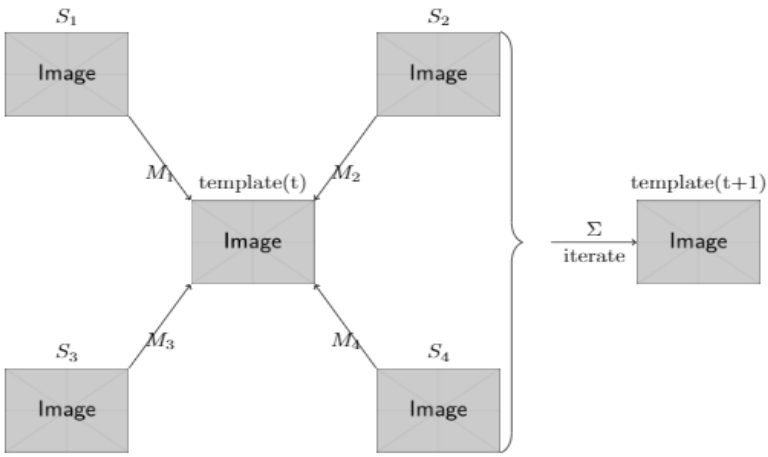

Figure 7.2 | Representation of the iteration process implemented by the *population_template* script in order to generate a population template from individually subjects' images. The image of each subject is symbolic represented by S_1, S_2, S_3 and S_4; the initial template image generated from a rough alignment via the centre of mass of the images is represented by *template(t)*, which will be consequently generated by registering and transforming (M_1, M_2, M_3 and M_4) all subjects to this estimated template *template(t)*; by iteratively updating this template using transformed and averaged images, which build the basis for the next template iteration, the final template *template*$(t+1)$ is calculated. Permission kindly provided by Maximilian Pietsch.

The next step consisted of register all the FOD images in the population template (by running the *mrregister* command), creating a two-way warp between the FOD template and each subject's FOD image.

Having in mind that different subjects will have subtly different brain coverage; to ensure subsequent analysis was performed in voxels that contained data from all subjects, all subject masks were warped into template space, using *mrtransform* command and, since the input and output were binary data, nearest neighbour interpolation was used. Therefore, the mask intersection was computed using the *mrmath* command.

To complete this analysis is imperative to compute a WM analysis voxel and a fixel mask, which were generated using the *mrconvert* command with *–coord* option to retain data from the input image only at the first coordinate along the *z*-axis, followed by the *mrthreshold* command.

Next all fixels from each FOD in the template image were segmented using *fod2fixel* command.

After warping the subjects' FOD images to the template space without FOD reorientation through the *mrtransform* command, each FOD image was segmented to estimate fixels and their FD as the FOD lobe integral. So, using the *fod2fixel* command it was possible to segment each FOD lobe in order to identify the number and orientation of fixels in each voxel.

Based on the Jacobian matrix (local affine transformation) the direction of all fixels at each voxel in the warp were reoriented with the *fixelreorient* command.

With spatial correspondence between subject and template and with the corrected fixel orientations, subject fixels were assigned to the template fixels using the *fixelcorrespondence* command. For each fixel in the template fixel analysis mask, the corresponding fixel in each voxel of the subject image was identified and the FD value of the subject fixel was then assigned to the corresponding fixel in template space.

However, it is well known that FD, and other related measures that are influenced by the quantity of restricted water, only permit the investigation of group differences in the number of axons that manifest as a change to within-voxel density. Depending on the disease type and stage, changes to the number of axons may also manifest as macroscopic differences in brain morphology. Due to this, a fixel-based metric related to morphological differences in fibre cross-section was calculated. The use of the *warp2metric* command allowed us to derive the information, which was needed to compute the FC metric, entirely from the warps generated during registration.

Aiming to perform group statistical analysis of FC, the log(FC) was calculated (using the *mrcalc* command with the *–log* option) to ensure data were centred about zero and normally distributed.

To account for changes to both within-voxel fibre density and macroscopic atrophy, fibre density and fibre cross-section were combined, which allowed to achieve a more complete picture of group differences in WM. This combined measure was called FDC, and it was generated by 'modulating' the FD by FC (FDC = FD × FC) using the *mrcalc* command.

From the FOD template a whole-brain tractogram was generated using probabilistic fibre tractography.

Statistical analysis (completed by running the *fixelcfestats* command) of FD, FC, and FDC was performed using connectivity-based fixel enhancement (CFE) [170] enhanced t-statistics (5000 permutations) using 1.5 million streamlines (after applying SIFT to reduce biases associated with particular tractography algorithms or seeding strategies, through the *tcksift* command) and defaults parameters. We assigned family-wise error corrected *p-values* to each fixel using permutation testing of the CFE. Significant fixels ($p < 0.05$) were displayed using MRtrix.

7.2 Results

Based on the whole-brain template-derived tractogram (**Figure 7.3 (A)**) and having in mind that each fixel was rendered by MRtrix as a line drawn along the fibre orientation considering the statistical value of the *p-value*, streamline points were "cropped" if they corresponded to fixels that did not reach significance ($p\text{-value} > 0.05$) and the remaining points coloured by streamline orientation (left-right: red, inferior-superior: blue, anterior-posterior: green) (**Figure 7.3 (B)**), or fixel value of interest as the *p-value* (**Figure 7.3 (C)**).

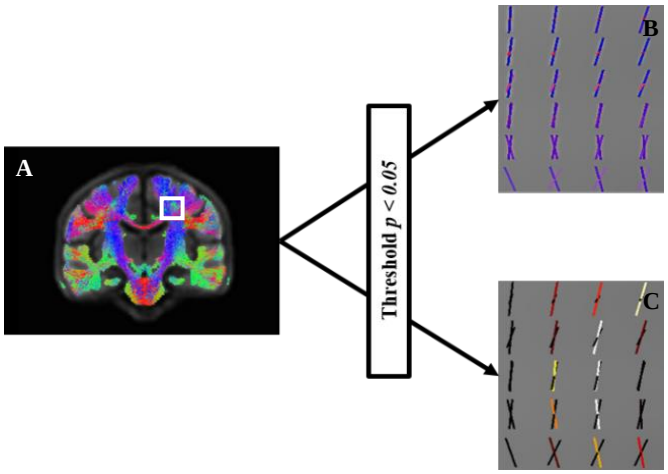

Figure 7.3 | Coronal view of the whole-brain tractogram **(A)** using the study-specific template, from where a 2D slice of fixels (zoomed out from the white square in (A) and threshold at *p-value* < *0.05*) was rendered as lines along the fibre orientation and coloured by streamline orientation **(B)** and *p-value* **(C).**

Shown in **Figure 7.4** are fixels with a significant reduction in FD, FC and FDC (especially along the left corticospinal tract) in TLE compared to controls. However, the fact that it was not obtained a significant result for FDC as expected could mean that there was genuinely no difference in this parameter, or the variance was too high, so the study was underpowered to detect it. For each view (axial, coronal and sagittal), a single 2D slice of fixels is shown, coloured by family-wise error corrected *p-value* and overlaid on the population FOD template image. By assigning an individual *p-value* to each fixel, rather than to each voxel, fibre tract-specific inference was achieved.

Results suggest that TLE patients have a decrease in the number of axons that manifests as a change in both within-voxel FD and FC (**Figure 7.4**, left and middle), and as expected, group differences were maximal on the lesioned side. The combination of information from FD and FC is shown by the FDC result (**Figure 7.4**, right).

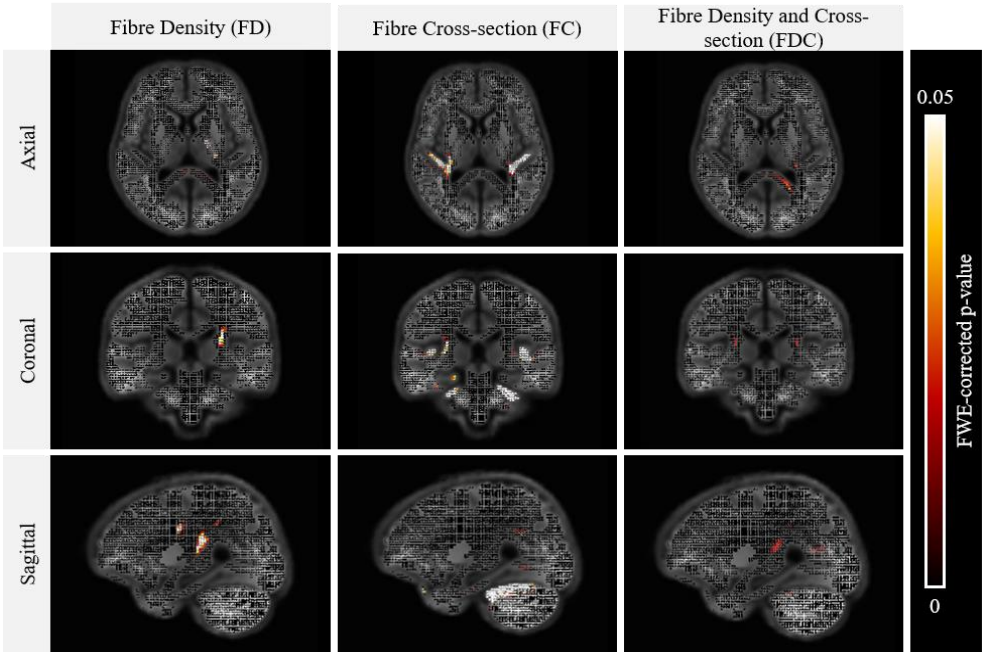

Figure 7.4 | Fixels with ($p < 0.05$) decrease in fibre density (FD), fibre cross-section (FC), and fibre density and cross-section (FDC). Fixels are colour-coded by family-wise error (FWE) corrected by *p-values* and overlaid on the population FOD template image.

To investigate the relative effect sizes of FD and FC, and how they combine to give a larger effect size in the FDC analysis, the effect size (group difference) was expressed relative to the control group and the result displayed as colour-coded streamlines. **Figure 7.5** shows the streamlines that correspond to all WM fixels with a significant decrease in FD, FC, and FDC.

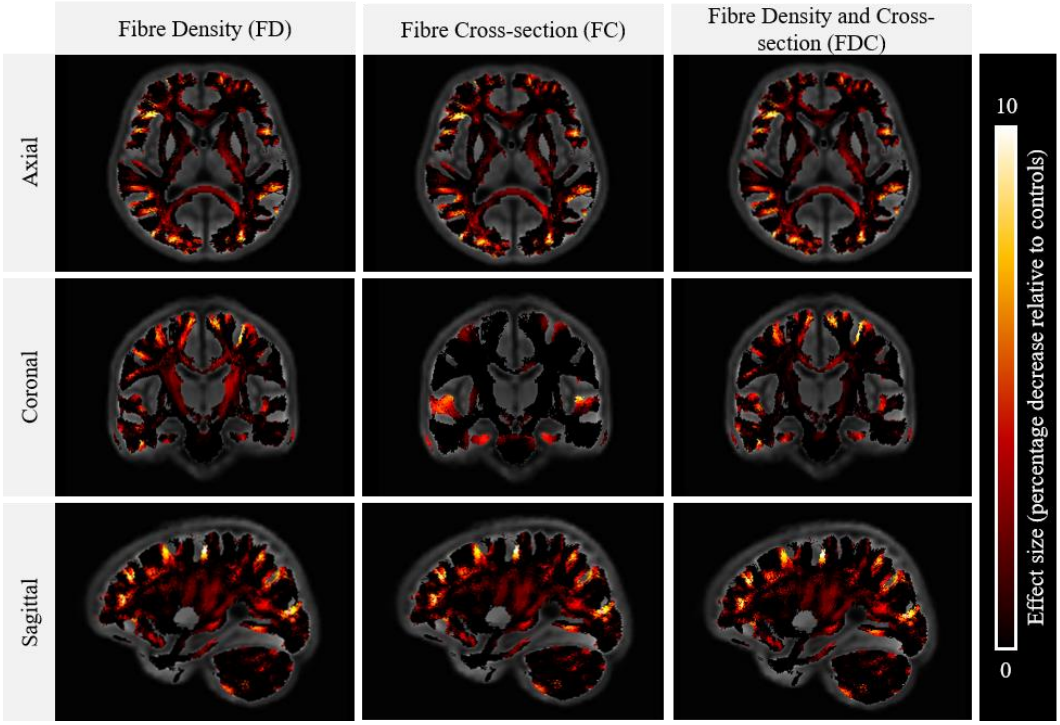

Figure 7.5 | Effect sizes across fibre density (FD), fibre cross-section (FC), and fibre density and cross-section (FDC) expressed as percentage decrease relative to the control group (ranging from 0 % to 10 %).

Many of the fibre pathways that connect to the affected temporal lobe show a significant decrease in FD and FDC. These include the WM pathways in study, as the arcuate fasciculus, left and right corticospinal tract, and (genu and splenium of) corpus callosum. The results also suggest that the main area of atrophy is located in the temporal lobe, which was shown evidently by the FC results.

As shown, when compared to healthy controls, TLE patients have a greater general reduction in FD than in FC (easily seen through the coronal view at **Figure 8.5**) along the WM pathways in study. This result is of interest, since changes in FC suggest a difference in the number of axons, while differences in the length of fibres should be ignored.

When FD is modulated by FC the effect size is very similar to the result obtained for the effect size generated by FD in all pathways shown, which proved to go against the expectations and fail in obtain the largest spatial extent of significant difference between the patient and control groups through this FDC modulation, as was mentioned by Raffelt *et al.* (2017) [169].

7.3 Discussion

The majority of diffusion MRI analysis methods and clinical studies have focused on measures related to within-voxel microstructure only. In this additionally study, a novel approach to WM morphology using diffusion MRI was used, known as FBA, allowing a comprehensive statistical analysis of WM quantitative measures in order to have access to changes that may result within WM tracts in the presence of TLE. Rather than computing some scalar metrics from the diffusion model in

each image voxel as the voxel-wise approaches; with this analysis framework, scalar quantitative (microstructural or macrostructural) measures are represented within fixels (specific fibre populations within voxels), enabling inference of fibre-specific properties in the WM The commonly investigated metrics within this framework are: FD that reflects changes in tissue microstructure, being a marker of the intra-axonal restricted compartment of a fibre bundle; FC that refers to the cross-sectional area that is occupied by a fibre bundle, and measures changes in local tissue macrostructure; and, combined measure FDC that allows to have access to both tissue microstructure and macrostructure changes.

Our aim with this additionally analysis was to establish the utility of FBA in TLE patients (with left epileptic focus), which may provide unique complementary information based on the metrics generated and associated to this framework, and highlight potential differences between TLE patients and healthy controls.

The results illustrated by **Figure 7.4** and **Figure 7.5** suggest that a significantly reduced FD, FC and FDC was verified in pathways that are concordant with the seizure foci. According to Raffelt *et al.* (2016) [169], this results could be justified by the degeneration process that affects WM structures with the loss of axons in the presence of a neuropathological condition as TLE. Additionally, **Figure 7.5** based on the effect size (group difference) expressed relative to the control group, allow us to conclude that the microstructural and/or macrostructural reductions in WM tracts of the TLE patients were not just confined to the temporal region of the left hemisphere (in this particularly case of study), with these changes being observed in large-scale brain networks, involving temporal and extratemporal regions of both hemispheres, which is in concordance with the previous achievements defended by Fahoum *et al.* (2012) [130] and Laufs (2012) [131].

It is also important to say that the FDC analysis was computed in order to detect additional significant fixels based on an increase in sensitivity that could be achieved by combining FD and FC. However, as it was possible to conclude and previously mentioned by Raffelt *et al.* (2016) [169], the combined FDC analysis may not always be more sensitive if the effect of interest is predominantly in either FD or FC, since combining FD and FC also combines the variance from each source, which allows us to say that FD and FC should still be investigated separately, since they may offer further insight to better characterise the effects under study.

Moving beyond the tensor model that has inherently voxel-averaged comparisons, FBA is able to perform fixel-based comparisons that provide more directly interpretable measures of structural connectivity, which account for the differing ways in which changes to intra-axonal volume may manifest. Indeed, in a disease like TLE, in which substantial WM loss occurs, partial volume effects could contribute to significant findings in voxel-based analyses of WM microstructure. As such, it is important to consider both microstructural and morphological differences that might reflect axonal loss as Raffelt *et al.* (2016) [169] made reference.

8 Conclusion

In the field of neuroimaging, diffusion weighted imaging remains one of the few techniques that allows researchers and clinicians to evaluate the microstructure of both healthy and pathological brain, *in vivo* and non-invasively. Over the years, diffusion imaging has played a very important clinical role by providing quantitative parameters relate to WM microstructure (Tournier *et al.*, 2011) [41].

Furthermore, with the advent of DTI and the techniques that have followed, it has provided the only current means to investigate connectional anatomy *in-vivo*. In turn, this enabled to explore the connectivity of different brain regions, providing the anatomical substrate for complex brain functional networks, which emerge from the interaction of multiple integrative centres that process and transmit information across brain regions. Following on from DTI, it became clear that a simple tensor model is unable to fully characterize the complexity of microstructural arrangements that is found in the brain: there are numerous examples of kissing, crossing and fanning fibres, which are configurations that are indistinguishable with DTI.

Whilst DTI still remains a very useful technique clinically, providing maps of parameters related to microstructural organization such as FA, the exploration of this complexity led to a plethora of methods dedicated to recovering microstructural features of the diffusion signal as accurately as possible.

Parametric diffusion models such as NODDI rely on *a priori* assumptions about the tissue microstructure and can therefore be very powerful tools for characterizing tissue regions where the microstructure is known and the parametric model is rich enough to embody it. Specifically, NODDI was introduced by Zhang *et al.* (2012) [97] as a practical diffusion MRI technique for estimating the microstructural complexity of dendrites and axons *in vivo* on clinical MRI scanners.

In contrast, the non-parametric framework of MAP-MRI defined by Özarslan *et al.* (2013) [91], aims to quantify diffusion in arbitrary tissue environments, and therefore may be more amenable to detecting and studying pathology or brain tissue changes at the whole-brain level, based on an analytical reconstruction of associated metrics that recover microstructural information by exploring restriction of water molecules.

With this in mind, rather than use a "tract-averaged" approach to analysis by averaging the scalar values into a single point-spread estimate for each WM tract, I proposed a complete workflow to conduct an along-tract analysis of WM pathways in the human brain and integrate not only DTI derived measures, but also more advanced parameters from NODDI and MAP-MRI, taking into account the potentially rich anatomical variation in diffusion imaging metrics along the tracts.

In this study, the tractography technique was performed in order to reconstruct the arcuate fasciculus, corticospinal tract and corpus callosum, in a subjects' population concerned by TLE patients and healthy controls. Then, after some specific markers of microstructural complexity were obtained for each WM tract, such as MD and FA as derived tensor measures; MSD, RTAP, RTOP and RTPP from the MAP-MRI framework; ODI, ICVF and ISOVF mapped using NODDI; the along-tract analysis was computed.

First, this analysis was performed along each WM tract of interest and then, in order to show that this technique allows a more detailed analysis of small ROIs extracted, it was also applied to check the along-tract streamline distribution from a complex fibre geometry with multiple fibres populations as the centrum semiovale (a region with crossing fibres from the arcuate fasciculus, corticospinal tract and corpus callosum). As a result, the microstructure signature of each WM tract was delineated based on the within variation of each scalar map previously estimated, taking into account the normal anatomy of each tract and the possible changes that could occur associated to the diagnosis of this neuropathological condition, due to an increased diffusivity and reduced diffusion anisotropy, suggesting a loss of structural organization and expansion of the extracellular space. Having in mind the

values previously registered for the variation of each microstructural parameter along each WM pathway of interest and along a small ROI extracted from each one aiming to avoid fibres from the WM tracts in the neighbourhood, this along-tract technique of analysis also demonstrated to be able to characterize the centrum semiovale with its complex WM configuration.

Second, the technique was easily extended to between-group analysis, by conducting an along-tract analysis of differences in multiple microstructural parameters between 9 TLE patients with left epileptic focus and 9 healthy controls.

This along-tract analysis of multiple microstructural metrics showed differences with statistical relevance, both locally and in extratemporal tracts despite the left epileptic focus, between the two groups, which agrees with the concept that epilepsy is a network disorder. The results suggest lower FA at the arcuate fasciculus in TLE patients. Regarding the corticospinal tract, lower FA was detected in the brainstem and close to the motor cortex, with a brief decrease being also verified near the mid-sagittal plane of the corpus callosum. Higher MD was observed within all tracts in TLE patients, which were also characterized by higher MSD. RTAP and RTOP were lower along the tracts of TLE patients. Despite RTPP assume lower values along the arcuate fasciculus and corticospinal tract of TLE patients, a smaller variation was displayed across the corpus callosum between the two groups, with no statistically significance being observed. Nevertheless, the MAP-MRI reveals to be a technique that subsumes DTI while is also able to provide several novel and quantifiable parameters that capture previously obscured intrinsic features of tissue microstructure. In particular, we showed that the arcuate fasciculus is microstructurally abnormal bilaterally despite the unilateral TLE diagnosed in these patients. And, the spatial profile assumed by RTAP and RTOP showed an increased difference within the corpus callosum between the two groups compared to the along-tract behaviour drawn by the FA profile, which highlights the biologically specificity of these tissue markers in pathologies characterized by neuronal reduction as TLE. Regarding the NODDI derived measures and focusing on the results assumed by ODI and ISOVF, major differences with statistical relevance between the two groups were not detected, expect along the left arcuate fasciculus for both microstructural parameters, and along the left/right corticospinal tract for the ISOVF metric. The results also reveal that the TLE patients showed significant lower values of ICVF when compared to healthy controls.

On the other hand, focused on the within-tract variability of the multiple microstructural parameters that exists along the tracts in study, these two studies based on an along-tract approach also highlighted the feasibility and potential benefits for clinical purposes with increased pathophysiological specificity obtained through this kind of analysis.

In addition, as a validation method of the microstructural changes that were concluded using the along-tract analysis when TLE patients were compared with healthy controls, but also as a technique capable of investigate WM change patterns across the whole brain, a TBSS method was applied to our dataset. As a fully automated whole-brain analysis technique that uses voxel-wise statistics on diffusion metrics but simultaneous minimizes the effects of misalignment using a conventional voxel-based analysis method, with TBSS we aimed to be able to describe the WM change patterns across the whole brain in TLE patients, and explore multiple diffusion metrics (FA, MD, MSD, RTAP, RTOP, RTPP, ODI, ICVF and ISOVF) alteration related to this neuropathological condition.

Based on this, with this study a global map of the WM changes in TLE patients by means of TBSS method was generated. Compared with healthy controls, the TLE patients showed significantly reduced FA, RTAP, RTOP, RTPP and ICVF, and increased MD and MSD in distributed WM regions, including the WM tracts studied using the along-tract analysis (between-groups study). No significant differences were achieved for ODI and ISOVF between the two groups along any of the tracts.

The diffusion changes and clinical correlations illustrated by the microstructural change patterns of each metric obtained with this leading technique for voxel-wise analysis were important since these findings are well documented through several studies over the last years, which allow us to assume it as a valid tool to investigate the robustness and clinical feasibility of the results derived from the along-

tract analysis, as well as the pathophysiological specificity regarding the diffusion changes that occur associated to TLE.

Nevertheless, one of the crucial steps of the TBSS analysis is the creation of the mean FA skeleton which represents the centres of all tracts common to the group, in order to project each subject's aligned FA data onto this skeleton. In addition TBSS assumes that the measurements are calculated by taking a weighted average of the microstructural parameters of each individual fibre at the node (so called “fibre core”) to combine measures throughout the length of the fibres across different subjects. This allow us to conclude that the workflow comprised by the along-tract analysis also shows increased specificity, compared to this voxelwise analysis, by displaying the values of each microstructural parameter on multiple points that were equidistantly distributed along each fibre across the whole thickness of each WM tract, which also reveals to be a major and extremely useful advantage of this technique in order to see and explore the extent of within-tract variability of each scalar map along the tracts.

Finally, an additional study was also performed based on the FBA in order to support the conclusions derived from the along-tract analysis between TLE patients and healthy controls. FBA allows a comprehensive statistical analysis of WM quantitative measures in order to detect changes in intra-axonal volume that may manifest as differences in within-voxel fibre density and/or macroscopic fibre bundle morphology in the presence of TLE (with left epileptic focus).

The FBA started with the generation of a population-specific FOD template, followed by the registration of all FOD images to that template. To identify WM differences between TLE patients and controls, three factors were quantified in all WM fixels: FD, FC and FDC.

Reductions in FD, FC and FDC were identified in TLE patients compared to controls, which is in line with the microstructural changes that result from the degeneration process that affects WM structures with the loss of axons in the presence of a neuropathological condition as TLE. Results that were also in concordance with the previous results obtained through the between-groups analysis performed using an along-tract approach, highlighting the fact that those changes are not necessarily restricted to the temporal lobe but might extend to other brain regions as well.

9 Future Directions

Future directions naturally emerge from the conclusions of this dissertation. First of all, it is clear that nowadays the whole diffusion imaging community is converging towards the use of multi-shell techniques and that for these to have clinical research value, it is essential that new methodologies, both at hardware and reconstruction level are practical and effective. Regarding the diffusion propagator reconstruction performed with SHORE or MAP-MRI, taken as a feasible and viable novel technique for clinical applications, future studies focusing on quantitative assessment, biophysical validation and clinical performance are needed. MAP-MRI subsumes DTI and provides a more comprehensive microstructural tissue characterization with complementary scalar indices that potentially could be more specifically related to features of tissue morphology (e.g., compartment size, cellularity, restriction). Consequently, the next step in investigating such approach would require optimisation of this methodology not only in terms of ability to reconstruct microstructural indices, which were explored in this dissertation as biologically specific tissue markers, but also in terms of angular features of the diffusion signal, for purposes of structural connectivity studies.

This will be crucial for tractography purposes where Spherical Deconvolution remains one of the best techniques to recover the directionality of diffusion displacements throughout the brain. The combination of diffusion propagator metrics in the computation of the orientation distribution function, tailored for the natural diffusivities of axons, can potentially improve angular resolutions. Furthermore, as tractography becomes more and more ubiquitous in the research community and clinical practise, the mapping of these metrics as well as others provided by DTI and NODDI, for example, along tracts, as explored in this dissertation, may help to better characterize differences between control and patient groups. However, knowing that this technique of analysis may help introduce a new way of comparing data which can portray differences in a more informative way, we can conclude from the results provided by the along-tract approach presented and used on the current study, that further studies are still needed focusing on the technical methodologies associated to the presented approach, since the standard deviation associated to each sample point of the diffusion metrics along the tracts was significant, which somehow may have influenced our results and consequently the conclusions drawn from them.

Despite all this, the along-tract analysis will be certainly useful not only to quantify microstructure, but also to infer structural connectivity, as current methodologies remain to be an open challenge in terms of diagnostic potential. Furthermore, while new methods of validating diffusion imaging are being developed, and as this fields gets close to the limit of what is possible without any assumptions on what is being imaged, the integration between model free and model-based approaches is certainly an avenue worth pursuing.

With this in mind and regarding the interesting results provided by the present along-tract approach, the aim of a future study could be to demonstrate that the architectural configuration of WM pathways reconstructed with tractography can be improved by informing the algorithm about the underlying microstructural characteristics, which play a key role by quantitative describing the diffusion process, even in the presence of crossing / kissing / fanning fibres, or a neurological disorder, such as epilepsy. As an example, we can performe an analysis showing that we could see better differences using WM tracts that had been "filtered" by the signature that was generated by an along-tract analysis, compared to “unfiltered” tractography.

Additionally and regarding the FBA, we propose to apply this framework to other dMRI models that aim to estimate a fixel-specific measure related to the intra-axonal volume (e.g. NODDI).

Given that FBA is a relatively new framework, there will naturally be a number of interesting follow-up experiments that can be conducted within a cross-sectional and longitudinal FBA setting. For example, adding the information regarding the subjects’ exposure to anti-seizure medications, which is known to be associated with cerebellar atrophy, may be a useful information to better define and characterize the degeneration process that was observed in this study across the TLE patients when compared to healthy controls. Incorporating this and other related variables in a follow-up analysis would be interesting and warranted. On the other hand, although FBA enables a more comprehensive

insight into WM changes, as illustrated by recent application in other disease states ((Raffelt *et al*., 2016) [169]; (Genc *et al*., 2017) [171]; (Vaughan *et al*., 2017) [172]; (Wright *et al*., 2017) [173]; (Gajamange *et al*., 2018) [174]), future studies including FBA, in conjunction with other neuroimaging methods, could enable much more fibre tract-specific insight than has previously been possible.

10 References

1. Megiddo I, Colson A, Chisholm D, Dua T, Nandi A, Laxminarayan R (2016). *Health and economic benefits of public financing of epilepsy treatment in India: An agent-based simulation model.* Epilepsia, 57(3): pp. 464-474.

2. Website: *https://www.epilepsy.com/learn/about-epilepsy-basics/what-epilepsy.* Accessed July 8, 2018.

3. Website: *https://www.epilepsysociety.org.uk/what-epilepsy#.WgMUV62cZBx.* Accessed July 8, 2018.

4. Gross DW (2011). *Diffusion tensor imaging in temporal lobe epilepsy.* Epilepsia, 52: pp. 32-34.

5. Rugg-Gunn FJ (2007). *Diffusion imaging in epilepsy.* Expert Review of Neurotherapeutics, 7(8): pp. 1043-1054.

6. Seeley R, Tate P, Stephens T (2007). *Anatomy and Physiology*, 6th edition. Boston, McGraw-Hill, pp. 374-381, 412-415.

7. Standring S (2016). *Gray's Anatomy : The Anatomical Basis of Clinical Practice*, 41st edition. London, Elsevier Health Sciences, pp. 227-237.

8. Feldman HM, Yeatman JD, Lee ES, Barde LH, Gaman-Bean S (2010). *Diffusion tensor imaging: a review for pediatric researchers and clinicians.* Journal of developmental and behavioral pediatrics, 31(4): 346.

9. Dubois J, Dehaene-Lambertz G, Kulikova S, Poupon C, *et al.* (2014). T*he early development of brain white matter: a review of imaging studies in fetuses, newborns and infants.* Neuroscience, 276: pp. 48-71.

10. Liégeois FJ, Mahony K, Connelly A, Pigdon L, Tournier JD, Morgan AT (2013). *Pediatric traumatic brain injury: language outcomes and their relationship to the arcuate fasciculus.* Brain and language, 127(3): pp. 388-398.

11. Moseley RL, Correia MM, Baron-Cohen S, Shtyrov Y, Pulvermüller F, Mohr B (2016). *Reduced volume of the arcuate fasciculus in adults with high-functioning autism spectrum conditions.* Frontiers in human neuroscience, 10: 214.

12. Catani M, Jones DK (2005). *Perisylvian language networks of the human brain.* Annals of neurology, 57(1): pp. 8-16.

13. Catani M, De Schotten MT (2008). *A diffusion tensor imaging tractography atlas for virtual in vivo dissections*. Cortex, 44(8): pp. 1105-1132.

14. Catani M, Allin MP, Husain M, Pugliese L, Mesulam MM, *et al.* (2007). *Symmetries in human brain language pathways correlate with verbal recall.* Proceedings of the National Academy of Sciences, 104(43): pp. 17163-17168.

15. Lebel C, Beaulieu C (2009). *Lateralization of the arcuate fasciculus from childhood to adulthood and its relation to cognitive abilities in children.* Human brain mapping, 30(11): pp. 3563-3573.

16. Vernooij MW, Smits M, Wielopolski PA, *et al.* (2007). *Fiber density asymmetry of the arcuate fasciculus in relation to functional hemispheric language lateralization in both right-and left-handed healthy subjects: a combined fMRI and DTI study.* Neuroimage, 35(3): pp. 1064-1076.

17. Propper RE, O'Donnell LJ, Whalen S, Tie Y, Norton IH, *et al.* (2010). *A combined fMRI and DTI examination of functional language lateralization and arcuate fasciculus structure: effects of degree versus direction of hand preference.* Brain and cognition, 73(2): pp. 85-92.

18. López-Barroso D, Catani M, Ripollés P, Dell'Acqua F, *et al.* (2013). *Word learning is mediated by the left arcuate fasciculus*. Proceedings of the National Academy of Sciences, 110(32): pp. 13168-13173.

19. Yeatman JD, Dougherty RF, Rykhlevskaia E, *et al.* (2011). *Anatomical properties of the arcuate fasciculus predict phonological and reading skills in children.* Journal of cognitive neuroscience, 23(11): pp. 3304-3317.

20. Catani M, Mesulam M (2008). *The arcuate fasciculus and the disconnection theme in language and aphasia: history and current state.* Cortex, 44(8): pp. 953-961.

21. Heilman KM, Watson RT (2008). *The disconnection apraxias*. Cortex, 44(8): pp. 975-982.

22. Doricchi F, de Schotten MT, Tomaiuolo F, Bartolomeo P (2008). *White matter (dis) connections and gray matter (dys) functions in visual neglect: gaining insights into the brain networks of spatial awareness.* Cortex, 44(8): pp. 983-995.

23. Yeo SS, Jang SH, Son SM (2014). *The different maturation of the corticospinal tract and corticoreticular pathway in normal brain development: diffusion tensor imaging study.* Frontiers in human neuroscience, 8: 573.

24. Website: *http://library.open.oregonstate.edu/aandp/chapter/14-5-sensory-and-motor-pathways/*. Accessed July 9, 2018.

25. Welniarz Q, Dusart I, Roze E (2017). *The corticospinal tract: Evolution, development, and human disorders.* Developmental neurobiology, 77(7): pp. 810-829.

26. Assaf Y, Johansen-Berg H, Thiebaut de Schotten M (2017). *The role of diffusion MRI in neuroscience.* NMR in Biomedicine, e3762.

27. Williams PT, Jiang YQ, Martin JH (2017). *Motor system plasticity after unilateral injury in the developing brain.* Developmental Medicine & Child Neurology, 59(12): pp. 1224-1229.

28. Yu Q, Yang W, Liu Y, Wang H, Chen Z, Yan J (2018). *Changes in the corpus callosum during the recovery of aphasia: A case report.* Medicine, 97(24): e11155.

29. Hinkley LB, Marco EJ, Findlay AM, Honma S, *et al.* (2012). *The role of corpus callosum development in functional connectivity and cognitive processing.* PLoS One, 7(8): e39804.

30. Goldstein A, Mesfin FB (2018). *Neuroanatomy, Corpus Callosum*. StatPearls Publishing.

31. Catani M, Thiebaut de Schotten M (2012). *Atlas of Human Brain Connections*, 1st edition. Oxford, Oxford University Press, pp. 37-54, 75-238, 343-438.

32. Rigucci S, Marques TR, Di Forti M, Taylor H, Dell'Acqua F, *et al.* (2016). *Effect of high-potency cannabis on corpus callosum microstructure.* Psychological medicine, 46(4): pp. 841-854.

33. Cover GS, Herrera WG, Bento MP, Appenzeller S, Rittner L (2018). *Computational methods for corpus callosum segmentation on MRI: A systematic literature review.* Computer methods and programs in biomedicine, 154: pp. 25-35.

34. Li Y, Mandal M, Ahmed SN (2013). *Fully automated segmentation of corpus callosum in midsagittal brain MRIs.* Engineering in Medicine and Biology Society (EMBS), 35th Annual International Conference of the IEEE (pp. 5111-5114).

35. Gold BT, Johnson NF, Powell DK, Smith CD (2012). *White matter integrity and vulnerability to Alzheimer's disease: preliminary findings and future directions.* Biochimica et Biophysica Acta (BBA) - Molecular Basis of Disease, 1822(3): pp. 416-422.

36. Garg N, Reddel SW, Miller DH, Chataway J, Riminton DS, *et al.* (2015). *The corpus callosum in the diagnosis of multiple sclerosis and other CNS demyelinating and inflammatory diseases.* Journal of Neurology, Neurosurgery, and Psychiatry, 86(12): pp. 1374-1382.

37. O'Dwyer R, Wehner T, LaPresto E, Ping L, Tkach J, Noachtar S, Diehl B (2010). *Differences in corpus callosum volume and diffusivity between temporal and frontal lobe epilepsy*. Epilepsy & Behavior, 19(3): pp. 376-382.

38. Hardan AY, Minshew NJ, Keshavan MS (2000). *Corpus callosum size in autism*. Neurology, 55(7): pp. 1033-1036.

39. Fernandez-Miranda JC, Pathak S, Engh J, Jarbo K, *et al.* (2012). *High-definition fiber tractography of the human brain: neuroanatomical validation and neurosurgical applications.* Neurosurgery, 71(2): pp. 430-453.

40. Website: *https://radiopaedia.org/articles/centrum-semiovale-1*. Accessed August 15, 2018.

41. Tournier JD, Mori S, Leemans A (2011). *Diffusion tensor imaging and beyond*. Magnetic resonance in medicine, 65(6): pp. 1532-1556.

42. Fernández-Miranda JC, Rhoton Jr AL, Álvarez-Linera J, Kakizawa Y, *et al.* (2008). *Three-dimensional microsurgical and tractographic anatomy of the white matter of the human brain*. Neurosurgery, 62(3): SHC989-SHC1028.

43. Wedeen VJ, Wang RP, Schmahmann JD, Benner T, *et al.* (2008). *Diffusion spectrum magnetic resonance imaging (DSI) tractography of crossing fibers.* Neuroimage, 41(4): pp. 1267-1277.

44. Hinshaw WS, Lent AH (1983). *An introduction to NMR imaging: From the Bloch equation to the imaging equation.* Proceedings of the IEEE, 71(3): pp. 338-350.

45. Pope JA (1999). *Medical physics: Imaging*, 1st edition. Oxford, Heinemann, pp. 72-95.

46. McRobbie DW, Moore EA, Graves MJ, Prince MR (2006). *MRI from Picture to Proton*, 2nd edition. Cambridge, Cambridge university press, pp. 11-200, 346-373.

47. Hashemi RH, Bradley WG, Lisanti CJ (2012). *MRI: The Basics*, 3rd edition. Philadelphia (USA), Lippincott Williams & Wilkins, pp. 1-175, 233-283.

48. Plewes DB, Kucharczyk W (2012). *Physics of MRI: a primer.* Journal of Magnetic Resonance Imaging, 35(5): pp. 1038-1054.

49. Lauterbur PC (1973). *Image formation by induced local interactions: examples employing nuclear magnetic resonance.* Nature, 242: pp. 190-191.

50. Larkman DJ, Nunes RG (2007). *Parallel magnetic resonance imaging.* Physics in Medicine & Biology, 52(7): R15.

51. Twieg DB (1983). *The k-trajectory formulation of the NMR imaging process with applications in analysis and synthesis of imaging methods.* Medical physics, 10(5): pp. 610-621.

52. Mansfield P (1984). *Real-time echo-planar imaging by NMR.* British medical bulletin, 40(2): pp. 187-190.

53. Turner R, Le Bihan D, Maier J, Vavrek R, Hedges LK, Pekar J (1990). *Echo-planar imaging of intravoxel incoherent motion.* Radiology, 177(2): pp. 407-414.

54. Poustchi-Amin M, Mirowitz SA, Brown JJ, *et al.* (2001). *Principles and applications of echo-planar imaging: a review for the general radiologist.* Radiographics, 21(3): pp. 767-779.

55. Jesmanowicz A, Bandettini PA, Hyde JS (1998). *Single-shot half k-space high-resolution gradient-recalled EPI for fMRI at 3 Tesla.* Magnetic Resonance in Medicine, 40(5): pp. 754-762.

56. Basser PJ, Jones DK (2002). *Diffusion-tensor MRI: theory, experimental design and data analysis–a technical review.* NMR in Biomedicine, 15(7-8): pp. 456-467.

57. Fick A (1855). *Ueber Diffusion.* Annalen der Physik und Chemie, 170(1), pp. 59–86.

58. Price WS (1997). *Pulsed-field gradient nuclear magnetic resonance as a tool for studying translational diffusion: Part 1 - Basic theory.* Concepts in Magnetic Resonance, 9(5): pp. 299-336.

59. Bihan DL (1995). *Molecular diffusion, tissue microdynamics and microstructure.* NMR in Biomedicine, 8(7): pp. 375-386.

60. Philibert J (2005). *One and a half century of diffusion: Fick, Einstein, before and beyond.* Diffusion Fundamentals, 2(1): pp. 1-10.

61. Moseley ME, Cohen Y, Kucharczyk J, *et al.* (1990). *Diffusion-weighted MR imaging of anisotropic water diffusion in cat central nervous system.* Radiology, 176(2): pp. 439-445.

62. Mori S, Barker PB. (1999). *Diffusion magnetic resonance imaging: its principle and applications.* The Anatomical Record, 257(3): pp. 102-109.

63. Alexander DC (2006). *An introduction to computational diffusion MRI: the diffusion tensor and beyond*. Visualization and processing of tensor fields (Springer, Berlin, Heidelberg), pp. 83-106.

64. Beaulieu C (2002). *The basis of anisotropic water diffusion in the nervous system–a technical review.* NMR in Biomedicine, 15(7-8): pp. 435-455.

65. Callaghan PT (1991). *Principles of nuclear magnetic resonance microscopy*, 1st edition. Oxford, Clarendon Press, pp. 371-399.

66. Campbell JSW (2004). *Diffusion imaging of white matter fibre tracts* (Doctoral dissertation). McGill University, Montreal, Canada.

67. Le Bihan D, Breton E, Lallemand D, *et al.* (1986). *MR imaging of intravoxel incoherent motions: application to diffusion and perfusion in neurologic disorders.* Radiology, 161(2): pp. 401-407.

68. Pipe J (2014). *Pulse sequences for diffusion-weighted MRI*, in *Diffusion MRI: From Quantitative Measurement to In vivo Neuroanatomy*, 2nd edition. London, Academic Press, pp. 11-34.

69. Stejskal EO, Tanner JE (1965). *Spin diffusion measurements: spin echoes in the presence of a time-dependent field gradient.* The journal of chemical physics, 42(1): pp. 288-292.

70. Mukherjee P, Berman JI, Chung SW, *et al.* (2008). *Diffusion tensor MR imaging and fiber tractography: theoretic underpinnings.* American journal of neuroradiology, 29(4): pp. 632-641.

71. Chang YS, Owen JP, Pojman NJ, Thieu T, *et al.* (2015). *White matter changes of neurite density and fiber orientation dispersion during human brain maturation.* PloS One, 10(6): e0123656.

72. Taylor DG, Bushell MC (1985). *The spatial mapping of translational diffusion coefficients by the NMR imaging technique*. Physics in Medicine & Biology, 30(4): 345.

73. Hess CP, Mukherjee P (2007). *Visualizing white matter pathways in the living human brain: diffusion tensor imaging and beyond.* Neuroimaging Clinics of North America, 17(4): pp. 407-426.

74. Jones DK (2009). *Gaussian modeling of the diffusion signal*, in *Diffusion MRI: From Quantitative Measurement to In vivo Neuroanatomy*, 2nd edition. London, Academic Press, pp. 37-54.

75. Basser PJ, Mattiello J, LeBihan D (1994). *MR diffusion tensor spectroscopy and imaging*. Biophysical journal, 66(1): pp. 259-267.

76. Soares J, Marques P, Alves V, Sousa N (2013). *A hitchhiker's guide to diffusion tensor imaging.* Frontiers in neuroscience, 7: 31.

77. Basser PJ (1995). *Inferring microstructural features and the physiological state of tissues from diffusion-weighted images.* NMR in Biomedicine, 8(7): pp. 333-344.

78. Pannek K, Scheck SM, Colditz PB, Boyd RN, Rose SE (2014). *Magnetic resonance diffusion tractography of the preterm infant brain: a systematic review.* Developmental Medicine & Child Neurology, 56(2): pp. 113-124.

79. Yoshida S, Oishi K, Faria AV, Mori S (2013). *Diffusion tensor imaging of normal brain development.* Pediatric radiology, 43(1): pp.15-27.

80. Callaghan PT, MacGowan D, Packer KJ, Zelaya FO (1990). *High-resolution q-space imaging in porous structures.* Journal of Magnetic Resonance, 90(1): pp. 177-182.

81. Basser PJ (2002). *Relationships between diffusion tensor and q-space MRI.* Magnetic resonance in medicine, 47(2): pp. 392-397.

82. Frank LR (2001). *Anisotropy in high angular resolution diffusion-weighted MRI.* Magnetic Resonance in Medicine, 45(6): pp. 935-939.

83. Tuch DS (2002). *Diffusion MRI of complex tissue structure* (Doctoral dissertation). Massachusetts Institute of Technology, Cambridge, Massachusetts, USA.

84. Tuch DS, Reese TG, Wiegell MR, Makris N, Belliveau JW, Wedeen VJ (2002). *High angular resolution diffusion imaging reveals intravoxel white matter fiber heterogeneity.* Magnetic Resonance in Medicine, 48(4): pp. 577-582.

85. Le Bihan D, Mangin JF, Poupon C, Clark CA, Pappata S, *et al.* (2001). *Diffusion tensor imaging: concepts and applications.* Journal of Magnetic Resonance Imaging, 13(4): pp. 534-546.

86. Callaghan PT, Eccles CD, Xia Y (1988). *NMR microscopy of dynamic displacements: k-space and q-space imaging.* Journal of Physics E: Scientific Instruments, 21(8): 820.

87. Merlet S, Caruyer E, Deriche R (2011). *Impact of radial and angular sampling on multiple shells acquisition in diffusion MRI.* International Conference on Medical Image Computing and Computer-Assisted Intervention (Springer, Berlin, Heidelberg), pp. 116-123.

88. Frank LR (2002). *Characterization of anisotropy in high angular resolution diffusion-weighted MRI.* Magnetic Resonance in Medicine, 47(6): pp. 1083-1099.

89. Assemlal HE, Tschumperlé D, Brun L (2009). *Efficient and robust computation of PDF features from diffusion MR signal.* Medical image analysis, 13(5): pp. 715-729.

90. Özarslan E, Koay CG, Basser PJ (2008). *Simple harmonic oscillator based estimation and reconstruction for one-dimensional q-space MR.* Presented at International Society for Magnetic Resonance in Medicine (ISMRM).

91. Özarslan E, Koay CG, Shepherd TM, *et al.* (2013). *Mean apparent propagator (MAP) MRI: a novel diffusion imaging method for mapping tissue microstructure.* NeuroImage, 78: pp. 16-32.

92. Avram AV, Sarlls JE, Barnett AS, Özarslan E, Thomas C, *et al.* (2016). *Clinical feasibility of using mean apparent propagator (MAP) MRI to characterize brain tissue microstructure.* NeuroImage, 127: pp. 422-434.

93. Fick RHJ, Pizzolato M, Wassermann D, Zucchelli M, *et al.* (2016). *A sensitivity analysis of q-space indices with respect to changes in axonal diameter, dispersion and tissue composition*. Presented at IEEE 13th International Symposium on Biomedical Imaging (pp. 1241-1244).

94. Fick RHJ, Wassermann D, Sanguinetti G, Deriche R (2015). *Laplacian-regularized MAP-MRI: improving axonal caliber estimation.* Presented at IEEE 12th International Symposium on Biomedical Imaging (pp. 1184-1187).

95. Ferizi U, Schneider T, Witzel T, Wald LL, Zhang H, *et al.* (2015). *White matter compartment models for in vivo diffusion MRI at 300mT/m.* NeuroImage, 118: pp. 468-483.

96. Yablonskiy DA, Sukstanskii AL (2010). *Theoretical models of the diffusion weighted MR signal*. NMR in Biomedicine, 23(7): pp. 661-681.

97. Zhang H, Schneider T, Wheeler-Kingshott CA, Alexander DC (2012). *NODDI: practical in vivo neurite orientation dispersion and density imaging of the human brain*. Neuroimage, 61(4): pp. 1000-1016.

98. Tournier JD, Calamante F, Gadian DG, Connelly A (2004). *Direct estimation of the fiber orientation density function from diffusion-weighted MRI data using spherical deconvolution.* NeuroImage, 23(3): pp. 1176-1185.

99. Dell'Acqua F, Rizzo G, Scifo P, Clarke RA, Scotti G, Fazio F (2007). *A model-based deconvolution approach to solve fiber crossing in diffusion-weighted MR imaging.* IEEE Transactions on Biomedical Engineering, 54(3): pp. 462-472.

100. Tournier JD, Calamante F, Connelly A (2007). *Robust determination of the fibre orientation distribution in diffusion MRI: non-negativity constrained super-resolved spherical deconvolution.* Neuroimage, 35(4): pp. 1459-1472.

101. Tariq M, Schneider T, Alexander DC, *et al.* (2016). *Bingham–NODDI: mapping anisotropic orientation dispersion of neurites using diffusion MRI*. Neuroimage, 133: pp. 207-223.

102. Daducci A, Canales-Rodríguez EJ, Zhang H, *et al.* (2015). *Accelerated microstructure imaging via convex optimization (AMICO) from diffusion MRI data*. NeuroImage, 105: pp. 32-44.

103. Mori S, Crain BJ, Chacko VP, Van Zijl PC (1999). *Three-dimensional tracking of axonal projections in the brain by magnetic resonance imaging.* Annals of Neurology, 45(2): pp. 265-269.

104. Jeurissen B, Descoteaux M, Mori S, Leemans A (2017). *Diffusion MRI fiber tractography of the brain*. NMR in Biomedicine, e3785.

105. Jones DK (2008). *Studying connections in the living human brain with diffusion MRI.* Cortex, 44(8): pp. 936-952.

106. Shi Y, Toga AW (2017). *Connectome imaging for mapping human brain pathways.* Molecular psychiatry, 22(9): 1230.

107. Rodrigues N, Mithani K, Meng Y, *et al.* (2018). *The Emerging Role of Tractography in Deep Brain Stimulation: Basic Principles and Current Applications.* Brain sciences, 8(2): 23.

108. Christiaens D, Reisert M, Dhollander T, Sunaert S, *et al.* (2015). *Global tractography of multi-shell diffusion-weighted imaging data using a multi-tissue model.* Neuroimage, 123: pp. 89-101.

109. Dell'Acqua F, Catani M (2012). *Structural human brain networks: hot topics in diffusion tractography.* Current opinion in neurology, 25(4): pp. 375-383.

110. Jbabdi S, Johansen-Berg H (2011). *Tractography: where do we go from here?*. Brain connectivity, 1(3): pp. 169-183.

111. Setsompop K, Gagoski BA, Polimeni JR, Witzel T, *et al.* (2012). *Blipped-controlled aliasing in parallel imaging for simultaneous multislice echo planar imaging with reduced g-factor penalty.* Magnetic resonance in medicine, 67(5): pp. 1210-1224.

112. Setsompop K, Cohen-Adad J, Gagoski BA, Raij T, Yendiki A, *et al.* (2012). *Improving diffusion MRI using simultaneous multi-slice echo planar imaging.* Neuroimage, 63(1): pp. 569-580.

113. Tournier JD, Calamante F, Connelly A (2012). *MRtrix: diffusion tractography in crossing fiber regions.* International Journal of Imaging Systems and Technology, 22(1): pp. 53-66.

114. Website: *https://fsl.fmrib.ox.ac.uk/fsl/fslwiki.* Accessed August 22, 2018.

115. Website: *https://surfer.nmr.mgh.harvard.edu/fswiki/FsTutorial/AnatomicalROI/FreeSurferColorLUT*. Accessed August 22, 2018.

116. Fischl B (2012). *FreeSurfer.* Neuroimage, 62(2): pp. 774-781.

117. Website: *https://media.readthedocs.org/pdf/mrtrix/latest/mrtrix.pdf.* Accessed August 22, 2018.

118. Galantucci S, Tartaglia MC, Wilson SM, *et al.* (2011). *White matter damage in primary progressive aphasias: a diffusion tensor tractography study.* Brain, 134(10): pp. 3011-3029.

119. Zhang Y, Li H, Lang X, Zhuo C, Qin W, Zhang Q (2015). *Abnormality of the corpus callosum in coalmine gas explosion-related posttraumatic stress disorder.* PloS One, 10(3): e0121095.

120. Smith RE, Tournier JD, Calamante F, Connelly A (2012). *Anatomically-constrained tractography: improved diffusion MRI streamlines tractography through effective use of anatomical information.* Neuroimage, 62(3): pp. 1924-1938.

121. Smith RE, Tournier JD, Calamante F, Connelly A (2013). *SIFT: spherical-deconvolution informed filtering of tractograms.* Neuroimage, 67: pp. 298-312.

122. Garyfallidis E, Brett M, Amirbekian B, Rokem A, Van Der Walt S, *et al.* (2014). *Dipy, a library for the analysis of diffusion MRI data.* Frontiers in neuroinformatics, 8: 8.

123. Schmithorst VJ, Yuan W (2010). *White matter development during adolescence as shown by diffusion MRI.* Brain and cognition, 72(1): pp. 16-25.

124. Wozniak JR, Lim KO (2006). *Advances in white matter imaging: a review of in vivo magnetic resonance methodologies and their applicability to the study of development and aging.* Neuroscience & Biobehavioral Reviews, 30(6): pp. 762-774.

125. Concha L, Livy DJ, Beaulieu C, Wheatley BM, Gross DW (2010). *In vivo diffusion tensor imaging and histopathology of the fimbria-fornix in temporal lobe epilepsy.* Journal of Neuroscience, 30(3): pp. 996-1002.

126. Davis SW, Dennis NA, Buchler NG, White LE, *et al.* (2009). *Assessing the effects of age on long white matter tracts using diffusion tensor tractography.* Neuroimage, 46(2): pp. 530-541.

127. Sullivan EV, Pfefferbaum A (2006). *Diffusion tensor imaging and aging.* Neuroscience & Biobehavioral Reviews, 30(6): pp. 749-761.

128. Xue R, Van Zijl PC, Crain BJ, Solaiyappan M, Mori S (1999). *In vivo three-dimensional reconstruction of rat brain axonal projections by diffusion tensor imaging.* Magnetic Resonance in Medicine, 42(6): pp. 1123-1127.

129. Yushkevich PA, Zhang H, Simon TJ, Gee JC (2009). *Structure-specific statistical mapping of white matter tracts.* Visualization and Processing of Tensor Fields (Springer, Berlin, Heidelberg), pp. 83-112.

130. Fahoum F, Lopes R, Pittau F, Dubeau F, Gotman J (2012). *Widespread epileptic networks in focal epilepsies: EEG-fMRI study*. Epilepsia, 53(9): pp. 1618-1627.

131. Laufs H (2012). *Functional imaging of seizures and epilepsy: evolution from zones to networks.* Current opinion in neurology, 25(2): pp. 194-200.

132. Ahmadi ME, Hagler DJ, McDonald CR, Tecoma ES, Iragui VJ, Dale AM, Halgren E (2009). *Side matters: diffusion tensor imaging tractography in left and right temporal lobe epilepsy*. American journal of neuroradiology, 30(9): pp. 1740-1747.

133. Otte WM, van Eijsden P, Sander JW, *et al.* (2012). *A meta-analysis of white matter changes in temporal lobe epilepsy as studied with diffusion tensor imaging.* Epilepsia, 53(4): pp. 659-667.

134. Concha L, Kim H, Bernasconi A, Bernhardt BC, Bernasconi N (2012). *Spatial patterns of water diffusion along white matter tracts in temporal lobe epilepsy.* Neurology, 79(5): pp. 455-462.

135. Pasternak O, Westin CF, Bouix S, Seidman LJ, Goldstein JM, *et al.* (2012). *Excessive extracellular volume reveals a neurodegenerative pattern in schizophrenia onset.* Journal of Neuroscience, 32(48): pp. 17365-17372.

136. McDonald CR, White NS, Farid N, Lai G, Kuperman JM, *et al.* (2013). *Recovery of white matter tracts in regions of peritumoral FLAIR hyperintensity with use of restriction spectrum imaging.* American Journal of Neuroradiology, 34(6), pp. 1157-1163.

137. French JA (2016). *Imaging brain inflammation: if we can see it, maybe we can treat it*. Epilepsy currents, 16(1): pp. 24-26.

138. Loi RQ, Leyden KM, Balachandra A, Uttarwar V, Hagler Jr DJ, *et al.* (2016). *Restriction spectrum imaging reveals decreased neurite density in patients with temporal lobe epilepsy.* Epilepsia, 57(11): pp. 1897-1906.

139. Hüppi PS, Dubois J (2006). *Diffusion tensor imaging of brain development.* Seminars in Fetal and Neonatal Medicine, 11(6): pp. 489-497.

140. Jones DK, Travis AR, Eden G, Pierpaoli C, Basser PJ (2005). *PASTA: pointwise assessment of streamline tractography attributes.* Magnetic Resonance in Medicine, 53(6): pp. 1462-1467.

141. Jones DK. (2010). *Diffusion MRI: theory, methods, and applications.*Oxford Medicine Online (website: *http://oxfordmedicine.com/view/10.1093/med/9780195369779.001.0001/med-9780195369779*; accessed September 2, 2018).

142. Wheeler-Kingshott CA, Cercignani M (2009). *About "axial" and "radial" diffusivities.* Magnetic Resonance in Medicine, 61(5): pp. 1255-1260.

143. Grinberg LT, Anghinah R, Nascimento CF, Amaro Jr E, *et al.* (2016). *Chronic traumatic encephalopathy presenting as Alzheimer's disease in a retired soccer player*. Journal of Alzheimer's disease, 54(1): pp. 169-174.

144. Groeschel S, Tournier JD, Northam GB, Baldeweg T, Wyatt J, *et al.* (2014). *Identification and interpretation of microstructural abnormalities in motor pathways in adolescents born preterm.* NeuroImage, 87: pp. 209-219.

145. Hervé PY, Cox EF, Lotfipour AK, Mougin OE, Bowtell RW, *et al.* (2011). *Structural properties of the corticospinal tract in the human brain: a magnetic resonance imaging study at 7 Tesla.* Brain Structure and Function, 216(3): pp. 255-262.

146. Reich DS, Smith SA, Jones CK, Zackowski KM, *et al.* (2006). *Quantitative characterization of the corticospinal tract at 3T.* American Journal of Neuroradiology, 27(10): pp. 2168-2178.

147. Sepehrband F, Clark KA, Ullmann JF, Kurniawan ND, Leanage G, *et al.* (2015). *Brain tissue compartment density estimated using diffusion-weighted MRI yields tissue parameters consistent with histology.* Human brain mapping, 36(9): pp. 3687-3702.

148. Wieshmann UC, Clark CA, Symms MR, Franconi F, *et al.* (1999). *Reduced anisotropy of water diffusion in structural cerebral abnormalities demonstrated with diffusion tensor imaging.* Magnetic resonance imaging, 17(9): pp. 1269-1274.

149. Campbell JS, Pike GB (2014). *Potential and limitations of diffusion MRI tractography for the study of language.* Brain and language, 131: pp. 65-73.

150. Ciccarelli O, Catani M, Johansen-Berg H, Clark C, Thompson A (2008). *Diffusion-based tractography in neurological disorders: concepts, applications, and future developments.* The Lancet Neurology, 7(8): pp. 715-727.

151. Johansen-Berg H, Behrens TE (2006). *Just pretty pictures? What diffusion tractography can add in clinical neuroscience.* Current opinion in neurology, 19(4): 379.

152. Lazar M, Alexander AL (2003). *An error analysis of white matter tractography methods: synthetic diffusion tensor field simulations.* Neuroimage, 20(2): pp. 1140-1153.

153. 2012. Tariq M, Schneider T, Alexander DC, Wheeler-Kingshot C, Zhang H (2012). *Scan-rescan reproducibility of neurite microstructure estimates using NODDI.* The British Machine Vision Association and Society for Pattern Recognition.

154. Smith SM, Jenkinson M, Johansen-Berg H, Rueckert D, *et al.* (2006). *Tract-based spatial statistics: voxelwise analysis of multi-subject diffusion data*. Neuroimage, 31(4): pp. 1487-1505.

155. Bach M, Laun FB, Leemans A, Tax CM, Biessels GJ, *et al.* (2014). *Methodological considerations on tract-based spatial statistics (TBSS).* Neuroimage, 100: pp. 358-369.

156. Website: *https://fsl.fmrib.ox.ac.uk/fsl/fslwiki/TBSS/UserGuide*. Accessed September 10, 2018.

157. Website: *https://fsl.fmrib.ox.ac.uk/fsl/fslwiki/Randomise/UserGuide.* Accessed September 12, 2018.

158. Smith SM, Nichols TE (2009). *Threshold-free cluster enhancement: addressing problems of smoothing, threshold dependence and localisation in cluster inference*. Neuroimage, 44(1): pp. 83-98.

159. Liu Z, Xu Y, An J, Wang J, Yin X, Huang R, *et al.* (2015). *Altered brain white matter integrity in temporal lobe epilepsy: a TBSS study.* Journal of Neuroimaging, 25(3): pp. 460-464.

160. Riley JD, Franklin DL, Choi V, Kim RC, *et al.* (2010). *Altered white matter integrity in temporal lobe epilepsy: association with cognitive and clinical profiles.* Epilepsia, 51(4): pp. 536-545.

161. Schoene-Bake JC, Faber J, Trautner P, Kaaden S, *et al.* (2009). *Widespread affections of large fiber tracts in postoperative temporal lobe epilepsy.* Neuroimage, 46(3): pp. 569-576.

162. Focke NK, Yogarajah M, Bonelli SB, Bartlett PA, Symms MR, Duncan JS (2008). *Voxel-based diffusion tensor imaging in patients with mesial temporal lobe epilepsy and hippocampal sclerosis.* Neuroimage, 40(2): pp. 728-737.

163. Sen PN, Basser PJ (2005). *A model for diffusion in white matter in the brain*. Biophysical journal, 89(5): pp. 2927-2938.

164. Arfanakis K, Hermann BP, Rogers BP, Carew JD, *et al.* (2002). *Diffusion tensor MRI in temporal lobe epilepsy.* Magnetic resonance imaging, 20(7): pp. 511-519.

165. Gross DW, Concha L, Beaulieu C (2006). *Extratemporal white matter abnormalities in mesial temporal lobe epilepsy demonstrated with diffusion tensor imaging.* Epilepsia, 47(8): pp. 1360-1363.

166. Petersen RC (2004). *Mild cognitive impairment as a diagnostic entity.* Journal of internal medicine, 256(3): pp. 183-194.

167. Keihaninejad S, Ryan NS, Malone IB, Modat M, Cash D, *et al.* (2012). *The importance of group-wise registration in tract based spatial statistics study of neurodegeneration: a simulation study in Alzheimer's disease.* PloS One, 7(11): e45996.

168. Van Hecke W, Leemans A, De Backer S, Jeurissen B, *et al.* (2010). *Comparing isotropic and anisotropic smoothing for voxel-based DTI analyses: A simulation study.* Human brain mapping, 31(1): pp. 98-114.

169. Raffelt DA, Tournier JD, Smith RE, Vaughan DN, Jackson G, *et al.* (2017). *Investigating white matter fibre density and morphology using fixel-based analysis.* Neuroimage, 144: pp. 58-73.

170. Raffelt DA, Smith RE, Ridgway GR, Tournier JD, Vaughan DN, *et al.* (2015). *Connectivity-based fixel enhancement: Whole-brain statistical analysis of diffusion MRI measures in the presence of crossing fibres.* Neuroimage, 117: pp. 40-55.

171. Genc S, Seal ML, Dhollander T, Malpas CB, Hazell P, Silk TJ (2017). *White matter alterations at pubertal onset.* Neuroimage, 156: pp. 286-292.

172. Vaughan DN, Raffelt D, Curwood E, Tsai MH, Tournier JD, *et al.* (2017). *Tract-specific atrophy in focal epilepsy: Disease, genetics, or seizures?.* Annals of neurology, 81(2): pp. 240-250.

173. Wright DK, Johnston LA, Kershaw J, Ordidge R, O'Brien TJ, Shultz SR (2017). *Changes in apparent fiber density and track-weighted imaging metrics in white matter following experimental traumatic brain injury.* Journal of neurotrauma, 34(13): pp. 2109-2118.

174. Gajamange S, Raffelt D, Dhollander T, Lui E, van der Walt A, *et al.* (2018). *Fibre-specific white matter changes in multiple sclerosis patients with optic neuritis*. NeuroImage Clinical, 17: pp. 60-68.

11 Appendices

The current chapter comprises the appendices referring to the project that was developed. According to the University College London Research Ethics Committee, the identification of the subjects' IDs is consider a breach of the ethical permission. So, in the next scripts the subjects' ID was written instead of the light-blue rectangle during the study.

11.1 Auxiliary MATLAB function

This appendix presents the auxiliary MATLAB function which was developed to extract the ROIs that correspond to the postcentral and precentral brain regions, which in turn allowed to obtain the homologous connection between motor cortices of the corpus callosum.

```
function [] = getting_rois(image,textfile,outputdir,outputname)


% ## eg
%
% # Left_CC.txt:
% # 1022    ctx-lh-postcentral
% # 1024    ctx-lh-precentral
%
% # getting_rois('aparc.nii','Left_CC.txt',pwd,'left_CC.nii')


% Load text file
fid=fopen(textfile);
lop=textscan(fid,'%s%s','Delimiter','\t');
fclose(fid);
labels=lop{1}(:,1);
labels = cellfun(@str2num,labels);

regions=lop{2}(:,1);

% Load Freesurfer parcellation
orig_nii = load_untouch_nii(image);
temp_nii = orig_nii;
orig_img = orig_nii.img;

% Save a roi with the regions we want (even if there are more in the text
% file)
indices = arrayfun (@(x) find(orig_img==x),labels,'UniformOutput',0);
total_indices = unique(cell2mat(indices));

temp_nii.img=zeros(size(orig_nii.img));
temp_nii.img(total_indices) = 1;
save_untouch_nii(temp_nii,fullfile(outputdir,outputname));

end
```

11.2 DTI derived metrics protocol

This appendix presents the script which was developed using the facilities of DIPY to return FA and MD values for a subject as example.

```
## Calculate FA and MD scalar maps

fdwi = '/Users/joana/Desktop/DWI_data_5tt/      /      _crop.nii.gz'
fbval = '/Users/joana/Desktop/DWI_data_5tt/      /      _dwi_corrected_TOP_1_1.bval'
fbvec = '/Users/joana/Desktop/DWI_data_5tt/      /      _dwi_corrected_TOP_1_1.bvec'

from dipy.io.image import load_nifti, save_nifti
from dipy.io import read_bvals_bvecs
from dipy.core.gradients import gradient_table
from dipy.reconst.dti import TensorModel, fractional_anisotropy, mean_diffusivity
import nibabel as nib
import numpy as np


data, affine = load_nifti(fdwi)
bvals, bvecs = read_bvals_bvecs(fbval, fbvec)
gtab = gradient_table(bvals, bvecs)


tenmodel = TensorModel(gtab)
tenfit = tenmodel.fit(data)

FA1 = fractional_anisotropy(tenfit.evals)
MD1 = mean_diffusivity(tenfit.evals)

FA2 = tenfit.color_fa
MD2 = tenfit.md

save_nifti('/Users/joana/Desktop/DWI_data_5tt/      /Metrics/      _color_fa.nii.gz', FA1, affine)
save_nifti('/Users/joana/Desktop/DWI_data_5tt/      /Metrics/      _fa_map.nii.gz', FA2, affine)
save_nifti('/Users/joana/Desktop/DWI_data_5tt/      /Metrics/      _color_md.nii.gz', MD1, affine)


from matplotlib import pyplot as plt
import numpy as np


FA_convert = FA1.flat
FA3 = list(FA_convert)
MD_convert = MD1.flat
MD3 = list(MD_convert)

print ('Length of FA array: ')
print (len(FA3))
print ('Length of MD array: ')
print (len(MD3))
```

11.3 MAP-MRI derived metrics protocol

This appendix presents the script which was developed using the facilities of DIPY to return MSD, RTOP, RTAP and RTPP values for a subject as example.

```
# Subject inf
fdwi = '/Users/joana/Desktop/DWI_data_5tt/      /      _crop.nii.gz'
fbval = '/Users/joana/Desktop/DWI_data_5tt/      /      _dwi_corrected_TOP_1_1.bval'
fbvec = '/Users/joana/Desktop/DWI_data_5tt/      /      _dwi_corrected_TOP_1_1.bvec'

# Libraries
import nibabel as nib
import numpy as np
import matplotlib.pyplot as plt
from mpl_toolkits.axes_grid1 import make_axes_locatable
from dipy.io.image import load_nifti, save_nifti
from dipy.io import read_bvals_bvecs
from dipy.core.gradients import gradient_table
from dipy.reconst.shore import ShoreModel
from dipy.reconst.mapmri import MapmriModel


data, affine = load_nifti(fdwi)
bvals, bvecs = read_bvals_bvecs(fbval, fbvec)
gtab = gradient_table(bvals, bvecs)
img = nib.load(fdwi)


print ('Information about the acquisition parameters:')
print (gtab.info)


S0s = data[:, :, :, gtab.b0s_mask]
# b0s_mask --> ((N,) ndarray) Boolean array indicating which gradients have no diffusion weighting, ie b-value is close to 0
S0s_shape = S0s.shape
print('Dimensions of S0s: (%d, %d, %d, %d)' % S0s_shape)


data_shape = data.shape
print ('Length of data_shape: %d' % len(data_shape))
print ('Shape of data (data_shape): (%d, %d, %d, %d)' % data_shape)


# Check the dimensions of each voxel
print('Dimensions of each voxel:(%d, %d, %d)' % img.header.get_zooms()[:3])


# All slices from the data
data_volume = data[:, :, :]

# Only one slice from the data
data_slice = data[:, :, data.shape[2]//2]


# Apply the model to the data
asm = ShoreModel(gtab)
mapmri = MapmriModel(gtab) #for RTPP


# Fit the signal with the model and calculate the SHORE / MAP MRI coefficients
asmfit_1 = asm.fit(data_volume)
mapfit_1 = mapmri.fit(data_volume)

asmfit_2 = asm.fit(data_slice)
mapfit_2 = mapmri.fit(data_slice)


# Calculate the analytical rtop on the signal that corresponds to the integral of the signal
print('Calculating rtop_signal')
rtop_signal_1 = asmfit_1.rtop_signal()
rtop_signal_2 = asmfit_2.rtop_signal()
rtop_signal_3 = (rtop_signal_2)**(1/3)  # Correct dimension


# Calculate the analytical rtop on the propagator, that corresponds to its central value
print('Calculating rtop_pdf')
rtop_pdf_1 = asmfit_1.rtop_pdf()
rtop_pdf_2 = asmfit_2.rtop_pdf()
rtop_pdf_3 = (rtop_pdf_2)**(1/2)  # Correct dimension


# Calculate the analytical rtpp that quantifies the probability of a proton be on the plane perpendicular to the main eigenvector of a
diffusion tensor during both gradient pulses
print('Calculating rtpp')
rtpp_1 = mapfit_1.rtpp()
rtpp_2 = mapfit_2.rtpp()

# Calculate the analytical mean square displacement on the propagator
print('Calculating msd')
msd_1 = asmfit_1.msd()
msd_2 = asmfit_2.msd()


# Save RTOP-RTAP-RTPP-MSD as four individual volumes in Nifti format
#nib.save(nib.Nifti1Image(S0s, img.affine), '/Users/joana/Desktop/DWI_data_5tt/      /Metrics/      _S0.nii.gz')
nib.save(nib.Nifti1Image(rtop_signal_1, img.affine), '/Users/joana/Desktop/DWI_data_5tt/      /Metrics/      _RTOP.nii.gz')
nib.save(nib.Nifti1Image(rtop_pdf_1, img.affine), '/Users/joana/Desktop/DWI_data_5tt/      /Metrics/      _RTAP.nii.gz')
nib.save(nib.Nifti1Image(rtpp_1, img.affine), '/Users/joana/Desktop/DWI_data_5tt/      /Metrics/      _RTPP.nii.gz')
nib.save(nib.Nifti1Image(msd_1, img.affine), '/Users/joana/Desktop/DWI_data_5tt/      /Metrics/      _MSD.nii.gz')
```

11.4 NODDI derived metrics protocol

This appendix presents the script which was developed using the facilities of AMICO to return ODI, ICVF and ISOVF values for a subject as example.

```
# NODDI parameters

import os.path as op
import numpy as np
import nibabel as nib
import dipy.data as dpd
from dipy.data import fetcher
import amico
amico.core.setup()

# Load the data
ae = amico.Evaluation("/home/joana/Desktop/DWI_data_5tt/    ","/home/joana/Desktop/DWI_data_5tt/    ")

amico.util.fsl2scheme('/home/joana/Desktop/DWI_data_5tt/    /    _dwi_corrected_TOP_1_1.bval', '/home/joana/Desktop/DWI_data_5tt/    /
    _dwi_corrected_TOP_1_1.bvec')

ae.load_data(dwi_filename = '    _dwi_corrected_TOP_1_1.nii.gz', scheme_filename = '    _dwi_corrected_TOP_1_1.scheme', mask_filename = '/
home/joana/Desktop/DWI_data_5tt/    /    _bet_mask.nii.gz', b0_thr = 0)

# Compute the response functions
ae.set_model("NODDI")
ae.generate_kernels(regenerate = True)
ae.load_kernels()

# Model fit
ae.fit()

# Save results at "/home/joana/Desktop/DWI_data_5tt/subject/AMICO/NODDI/*"
ae.save_results()
```

11.5 Design matrix and contrasts file

This appendix presents the design matrix and the contrasts file, both used on the FBA and TBSS analysis.

Design matrix

```
/NumWaves       4
/NumPoints      18
/PPheights              1.000000e+00    1.000000e+00    1.800000e+01    1.000000e+00

/Matrix
1.000000e+00    0.000000e+00    1.400000e+01    1.000000e+00
1.000000e+00    0.000000e+00    1.800000e+01    1.000000e+00
1.000000e+00    0.000000e+00    6.000000e+00    0.000000e+00
1.000000e+00    0.000000e+00    1.500000e+01    0.000000e+00
1.000000e+00    0.000000e+00    7.000000e+00    1.000000e+00
1.000000e+00    0.000000e+00    5.000000e+00    1.000000e+00
1.000000e+00    0.000000e+00    1.800000e+01    0.000000e+00
1.000000e+00    0.000000e+00    6.000000e+00    0.000000e+00
1.000000e+00    0.000000e+00    1.700000e+01    0.000000e+00
0.000000e+00    1.000000e+00    1.800000e+01    0.000000e+00
0.000000e+00    1.000000e+00    1.700000e+01    0.000000e+00
0.000000e+00    1.000000e+00    1.400000e+01    1.000000e+00
0.000000e+00    1.000000e+00    1.700000e+01    0.000000e+00
0.000000e+00    1.000000e+00    1.500000e+01    1.000000e+00
0.000000e+00    1.000000e+00    8.000000e+00    0.000000e+00
0.000000e+00    1.000000e+00    8.000000e+00    0.000000e+00
0.000000e+00    1.000000e+00    1.000000e+01    1.000000e+00
0.000000e+00    1.000000e+00    1.400000e+01    1.000000e+00
```

Contrasts files

```
/ContrastName1  P>C
/ContrastName2  P<C
/NumWaves       4
/NumContrasts   2
/PPheights              1.364900e+00    1.364900e+00
/RequiredEffect         3.699   3.699

/Matrix
1.000000e+00 -1.000000e+00 0.000000e+00 0.000000e+00
-1.000000e+00 1.000000e+00 0.000000e+00 0.000000e+00
```

11.6 Along-tract analysis: single-subject

This appendix presents the results regarding the along-tract analysis of a single-subject.

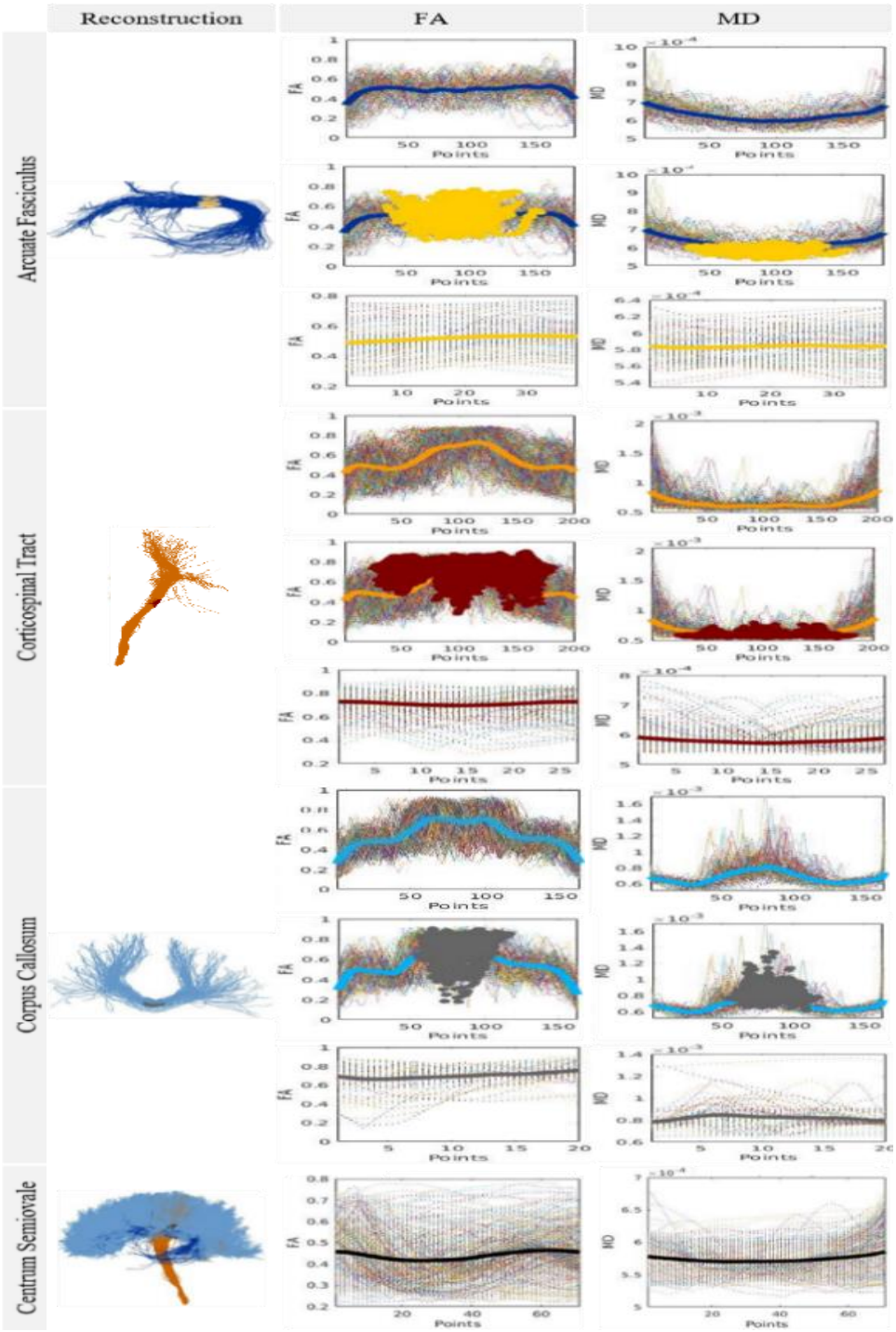

Figure 11.1 | Along-tract analysis of the left arcuate fasciculus (AF), left corticospinal tract (CST), corpus callosum (CC) - homologous connection between motor cortices, and left centrum semiovale (from top to bottom) based on their tractograms, from which it was possible to generate the reconstructions via MATLAB (first column). The following columns are divided in groups of three rows. The first row illustrate the variation of fractional anisotropy (FA) and mean diffusivity (MD) along each WM tract of interest. In the second row, it was highlighted, from all the streamlines, the value of each diffusion metric assumed by each resampled point that is part of the extracted ROI from each WM pathway. The respective average variation of each scalar map along the extracted ROI is represented in the third row of graphs. The reconstruction of left AF was coloured by blue, the left CST by orange, and the CC by light-blue, from which the extracted ROIs were coloured by yellow, red and grey, respectively. The centrum semiovale (left hemisphere) was coloured by black after merging the left AF (blue), left CST (orange) and CC (light-blue). The units of MD are mm^2/s.

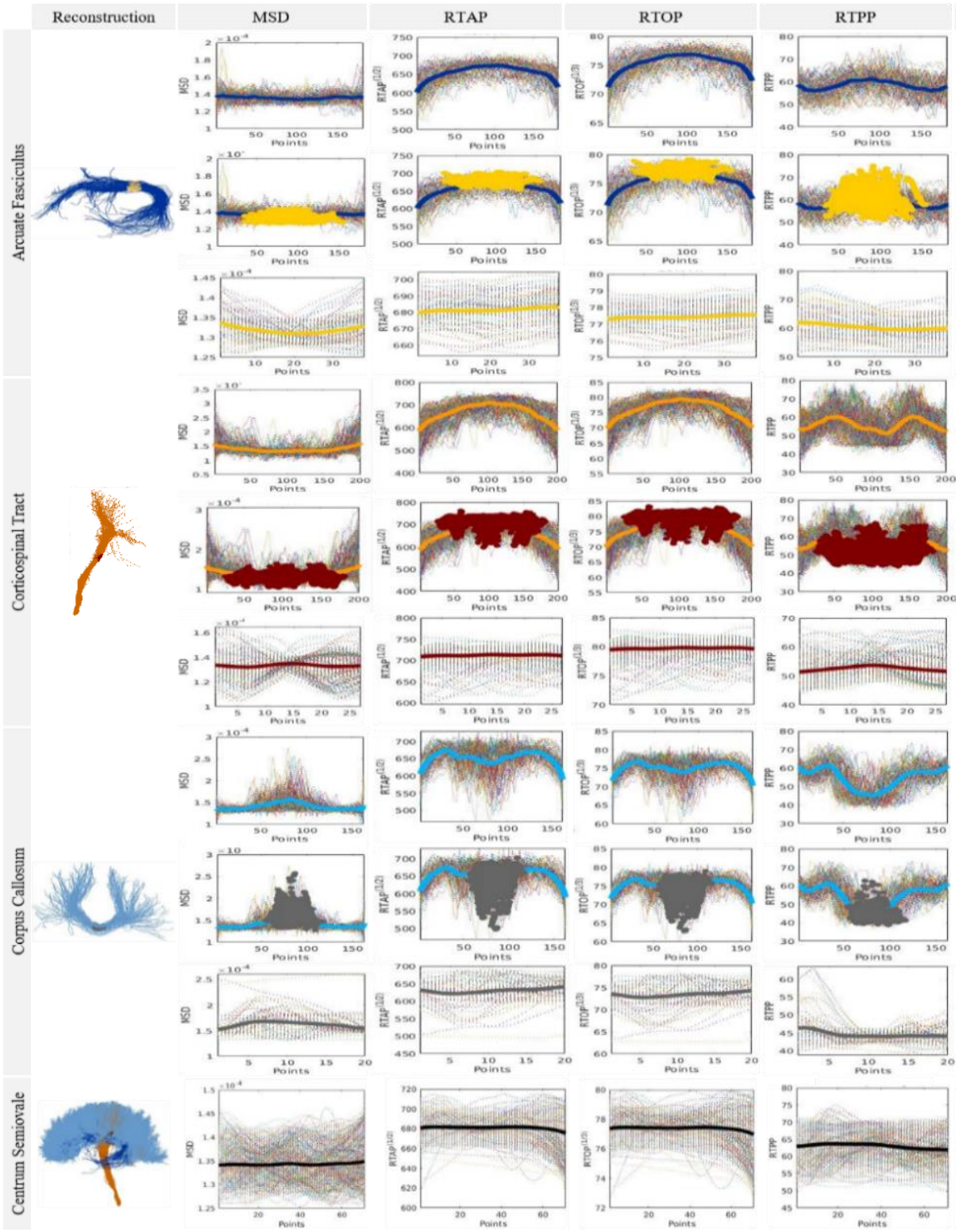

Figure 11.2 | Along-tract analysis of the left arcuate fasciculus (AF), left corticospinal tract (CST), corpus callosum (CC) - homologous connection between motor cortices, and left centrum semiovale (from top to bottom) based on their tractograms, from which it was possible to generate the reconstructions via MATLAB (first column). The following columns are divided in groups of three rows. The first row illustrate the variation of mean square displacement (MSD), (square-root of) return to axis probability (RTAP), (cube-root of) return to origin probability (RTOP) and return to plane probability (RTPP) along each WM tract of interest. In the second row, it was highlighted, from all the streamlines, the value of each diffusion metric assumed by each resampled point that is part of the extracted ROI from each WM pathway. The respective average variation of each scalar map along the extracted ROI is represented in the third row of graphs. The reconstruction of left AF was coloured by blue, the left CST by orange, and the CC by light-blue, from which the extracted ROIs were coloured by yellow, red and grey, respectively. The centrum semiovale (left hemisphere) was coloured by black after merging the left AF (blue), left CST (orange) and CC (light-blue). The units of MSD are mm^2/s, and RTAP, RTOP and RTPP are given by mm^{-1}.

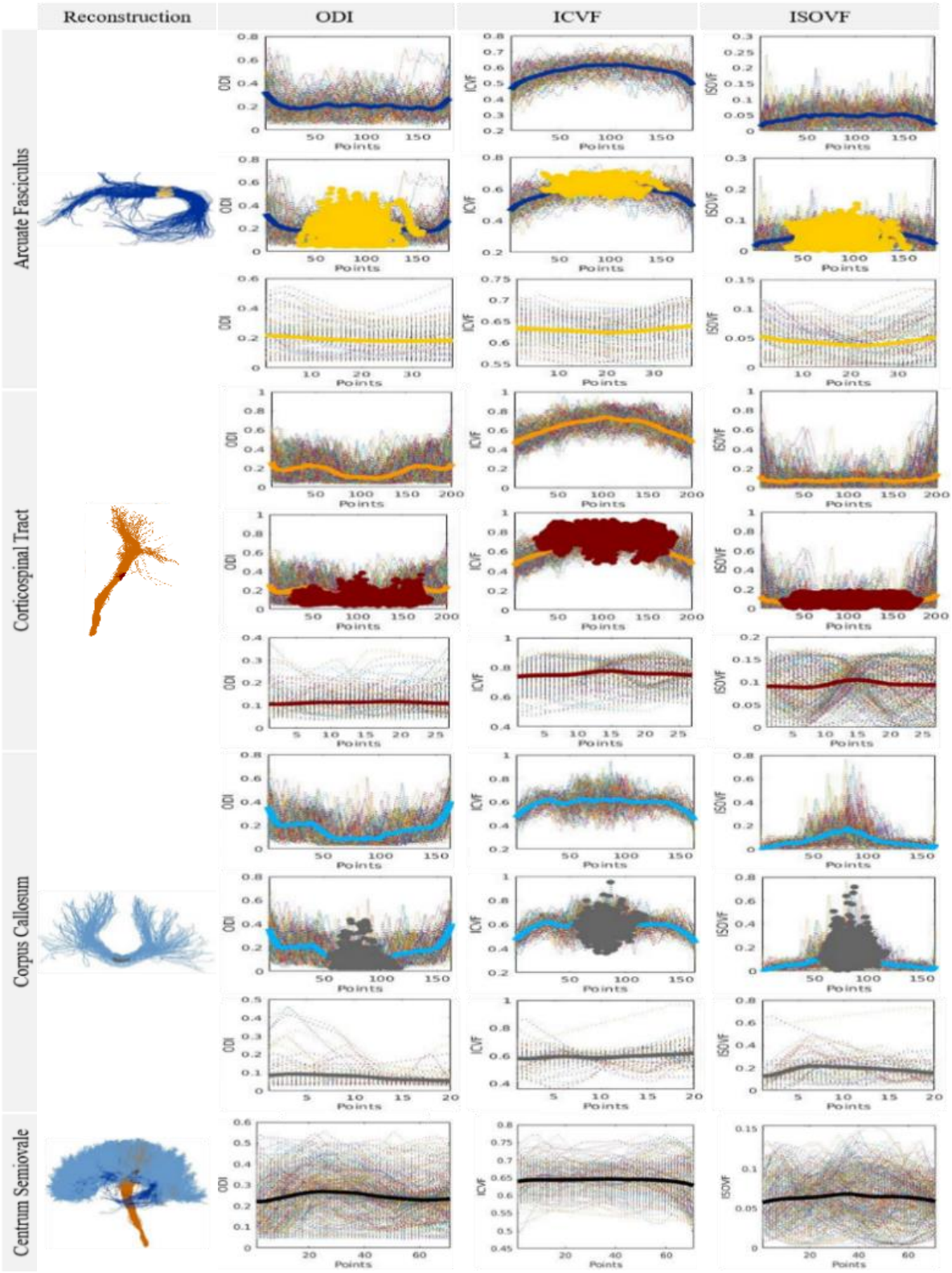

Figure 11.3 | Along-tract analysis of the left arcuate fasciculus (AF), left corticospinal tract (CST), corpus callosum (CC) - homologous connection between motor cortices, and left centrum semiovale (from top to bottom) based on their tractograms, from which it was possible to generate the reconstructions via MATLAB (first column). The following columns are divided in groups of three rows. The first row illustrate the variation of orientation dispersion index (ODI), intracellular volume fraction (ICVF) and isotropic volume fraction (ISOVF) along each WM tract of interest. In the second row, it was highlighted, from all the streamlines, the value of each diffusion metric assumed by each resampled point that is part of the extracted ROI from each WM pathway. The respective average variation of each scalar map along the extracted ROI is represented in the third row of graphs. The reconstruction of left AF was coloured by blue, the left CST by orange, and the CC by light-blue, from which the extracted ROIs were coloured by yellow, red and grey, respectively. The centrum semiovale (left hemisphere) was coloured by black after merging the left AF (blue), left CST (orange) and CC (light-blue).

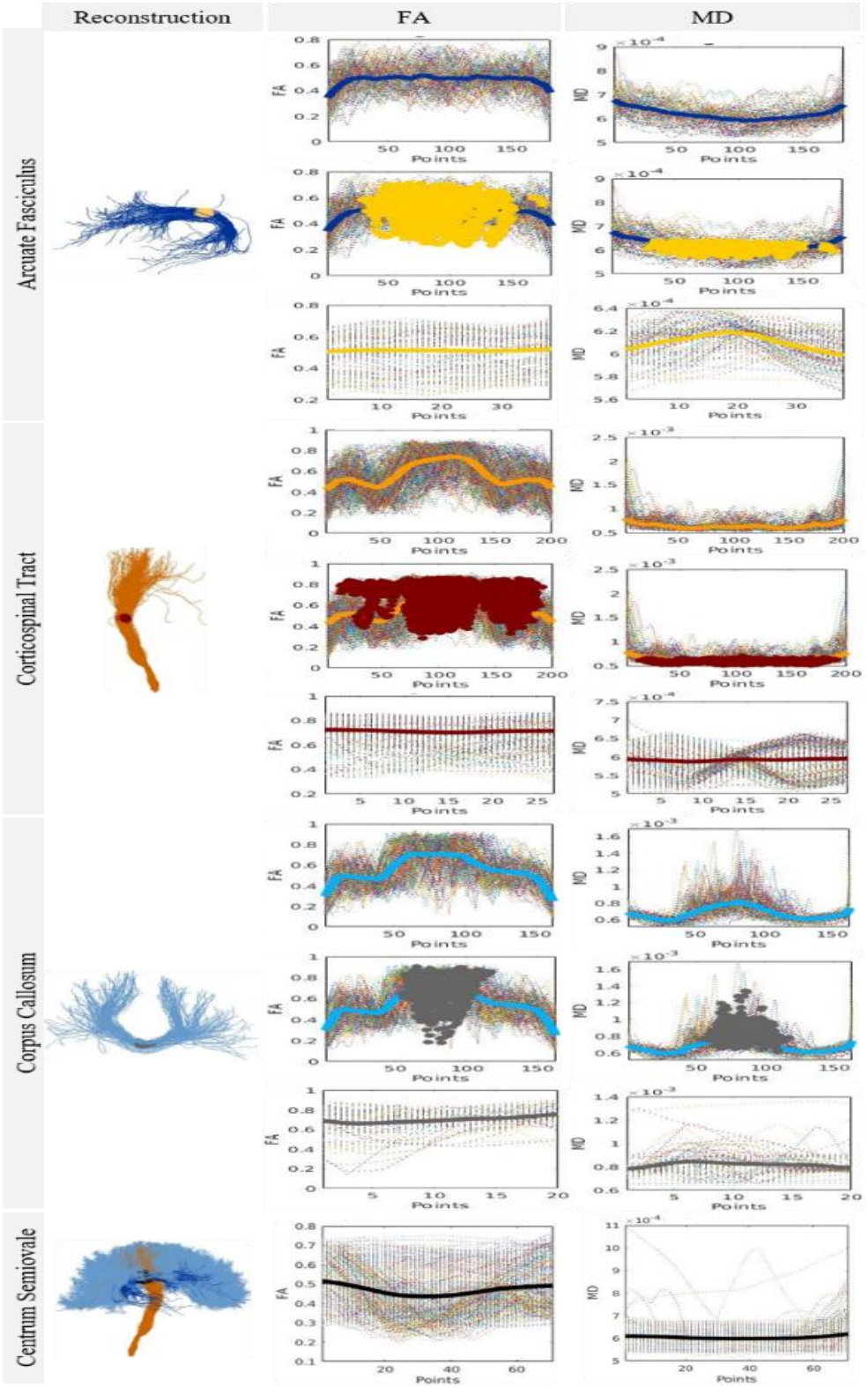

Figure 11.4 | Along-tract analysis of the right arcuate fasciculus (AF), right corticospinal tract (CST), corpus callosum (CC) - homologous connection between motor cortices, and right centrum semiovale (from top to bottom) based on their tractograms, from which it was possible to generate the reconstructions via MATLAB (first column). The following columns are divided in groups of three rows. The first row illustrate the variation of fractional anisotropy (FA) and mean diffusivity (MD) along each WM tract of interest. In the second row, it was highlighted, from all the streamlines, the value of each diffusion metric assumed by each resampled point that is part of the extracted ROI from each WM pathway. The respective average variation of each scalar map along the extracted ROI is represented in the third row of graphs. The reconstruction of right AF was coloured by blue, the right CST by orange, and the CC by light-blue, from which the extracted ROIs were coloured by yellow, red and grey, respectively. The centrum semiovale (right hemisphere) was coloured by black after merging the right AF (blue), right CST (orange) and CC (light-blue). The units of MD are mm^2/s.

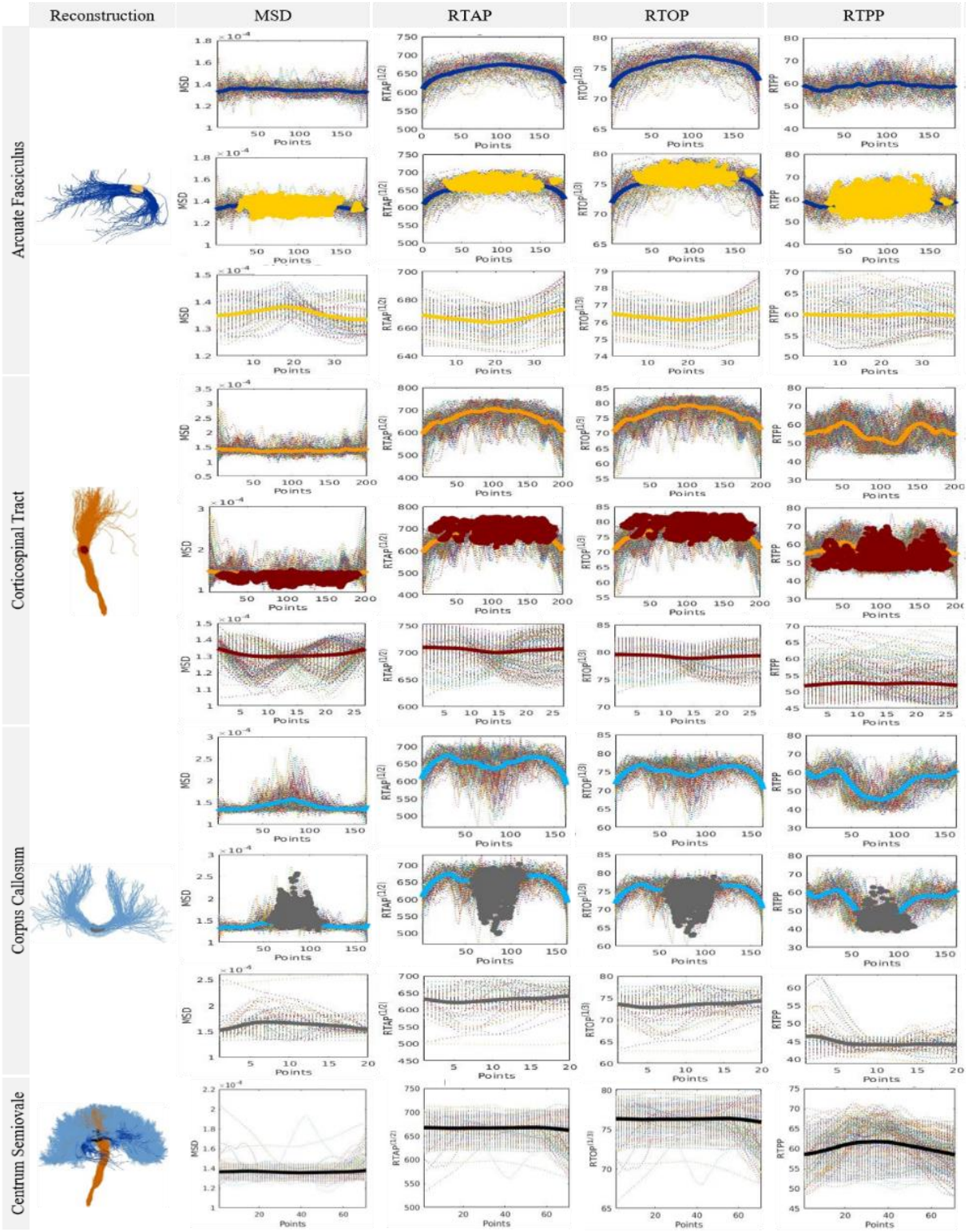

Figure 11.5 | Along-tract analysis of the right arcuate fasciculus (AF), right corticospinal tract (CST), corpus callosum (CC) - homologous connection between motor cortices, and right centrum semiovale (from top to bottom) based on their tractograms, from which it was possible to generate the reconstructions via MATLAB (first column). The following columns are divided in groups of three rows. The first row illustrate the variation of mean square displacement (MSD), (square-root of) return to axis probability (RTAP), (cube-root of) return to origin probability (RTOP) and return to plane probability (RTPP) along each WM tract of interest. In the second row, it was highlighted, from all the streamlines, the value of each diffusion metric assumed by each resampled point that is part of the extracted ROI from each WM pathway. The respective average variation of each scalar map along the extracted ROI is represented in the third row of graphs. The reconstruction of left AF was coloured by blue, the left CST by orange, and the CC by light-blue, from which the extracted ROIs were coloured by yellow, red and grey, respectively. The centrum semiovale (right hemisphere) was coloured by black after merging the right AF (blue), right CST (orange) and CC (light-blue). The units of MSD are mm^2/s, and RTAP, RTOP and RTPP are given by mm^{-1}.

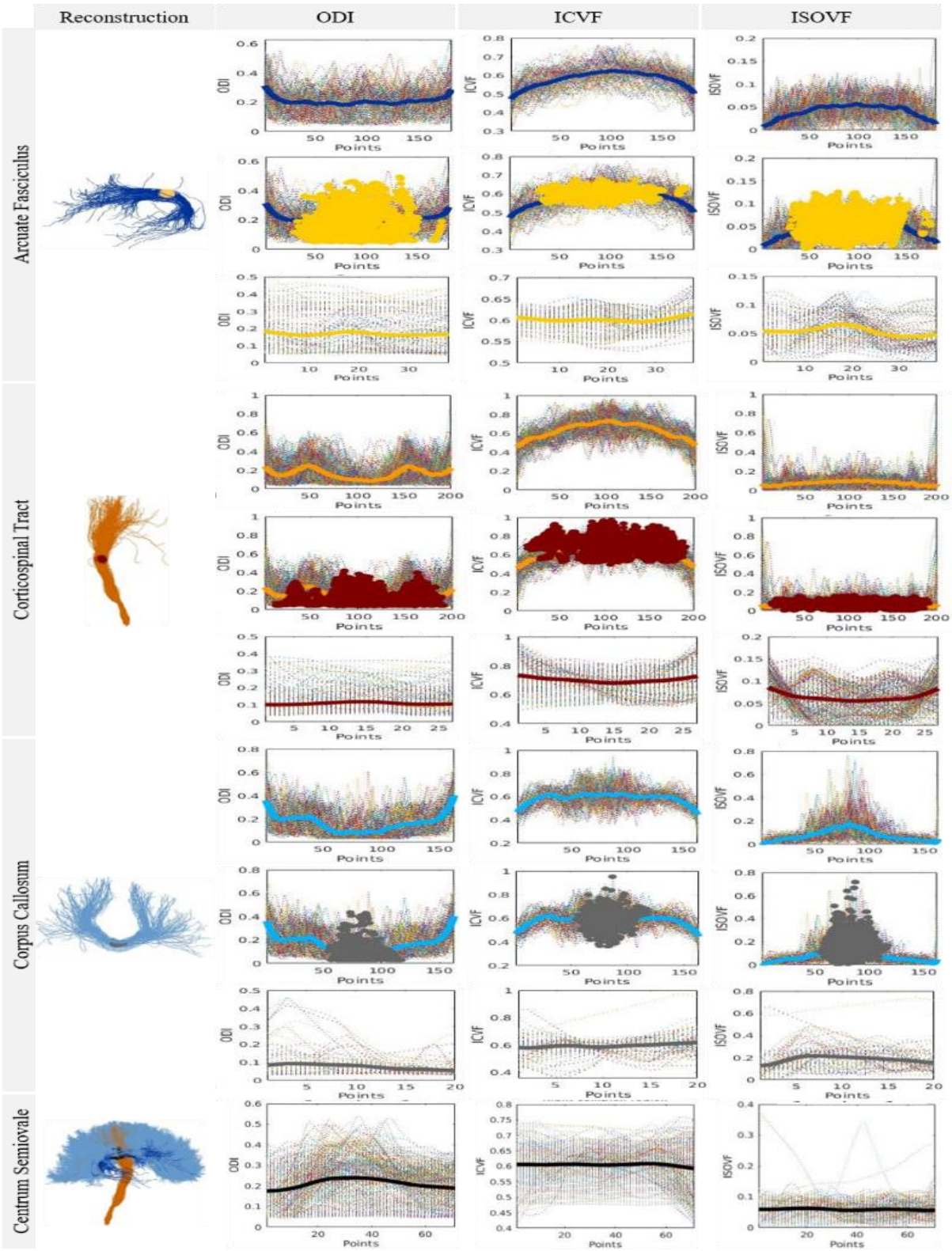

Figure 11.6 | Along-tract analysis of the right arcuate fasciculus (AF), right corticospinal tract (CST), corpus callosum (CC) - homologous connection between motor cortices, and right centrum semiovale (from top to bottom) based on their tractograms, from which it was possible to generate the reconstructions via MATLAB (first column). The following columns are divided in groups of three rows. The first row illustrate the variation of orientation dispersion index (ODI), intracellular volume fraction (ICVF) and isotropic volume fraction (ISOVF) along each WM tract of interest. In the second row, it was highlighted, from all the streamlines, the value of each diffusion metric assumed by each resampled point that is part of the extracted ROI from each WM pathway. The respective average variation of each scalar map along the extracted ROI is represented in the third row of graphs. The reconstruction of left AF was coloured by blue, the left CST by orange, and the CC by light-blue, from which the extracted ROIs were coloured by yellow, red and grey, respectively. The centrum semiovale (right hemisphere) was coloured by black after merging the right AF (blue), right CST (orange) and CC (light-blue).

12 Publications

Joana Guido, Luis Lacerda, Alexandre Andrade, Hugo Ferreira, Chris Clark. "Integration of multi-shell diffusion imaging derived metrics in tractography reconstructions in clinical data", submitted for the VII AEICBAS Biomedical Congress (Porto, Portugal).

Integration of multi-shell diffusion imaging derived metrics in tractography reconstructions of clinical data

Joana Guido[1,2], Luis Lacerda[2], Alexandre Andrade[1], Hugo Ferreira[1], Chris Clark[2]

[1] Institute of Biomedical Engineering and Biophysics (IBEB), Faculty of Sciences, University of Lisbon, Portugal; [2] Developmental Imaging and Biophysics Section, UCL Great Ormond Street Institute of Child Health, London, United Kingdom

KEYWORDS

Along-tract analysis; Diffusion Tensor Imaging (DTI); Mean Apparent Propagator - Magnetic Resonance Imaging (MAP-MRI); Temporal Lobe Epilepsy (TLE).

INTRODUCTION & OBJECTIVES

Traditional tractography studies rely on averaging diffusion metrics along reconstructed pathways to identify microstructural changes between groups. A workflow to conduct along-tract analysis of white matter tracts and integrate not only DTI derived measures, but also more advanced parameters from MAP-MRI, was developed to investigate differences between controls and patients with TLE, taking into account the potentially rich anatomical variation in diffusion metrics along the tracts.

METHODS

9 Patients with left TLE and 9 controls (***Table 1***) were studied. Images were previously acquired and pre-processed. Tractography of arcuate fasciculus (AF), corticospinal tract (CST) and corpus callosum (CC) – homologous connection between motor cortices, and along-tract analysis, with integration of diffusion metrics, were performed (complete pipeline in ***Figure 1***). A Kruskal-Wallis test was executed to verify that the groups are statistically different, taking into account three sections of each tract with equivalent number of resampled points. A 1% significance value was considered.

Table 1 *– Controls and patients with Temporal Lobe Epilepsy (TLE) characterisation according to gender. Age is given in years old (y.o.) with mean ± standard deviation (SD) and with the respective range.*

	Controls	**Patients with TLE**
N	**9**	**9**
Gender	**5 M / 4 F**	**5 M / 4 F**
Age (y.o.) by gender	**[13 ± 5] / [11 ± 3]** **[8 - 18] / [8 - 15]**	**[13 ± 6] / [11 ± 6]** **[6 - 19] / [5 - 19]**
Age (y.o.) group total	**12 ± 4** **[8 – 18]**	**12 ± 5** **[5 – 19]**

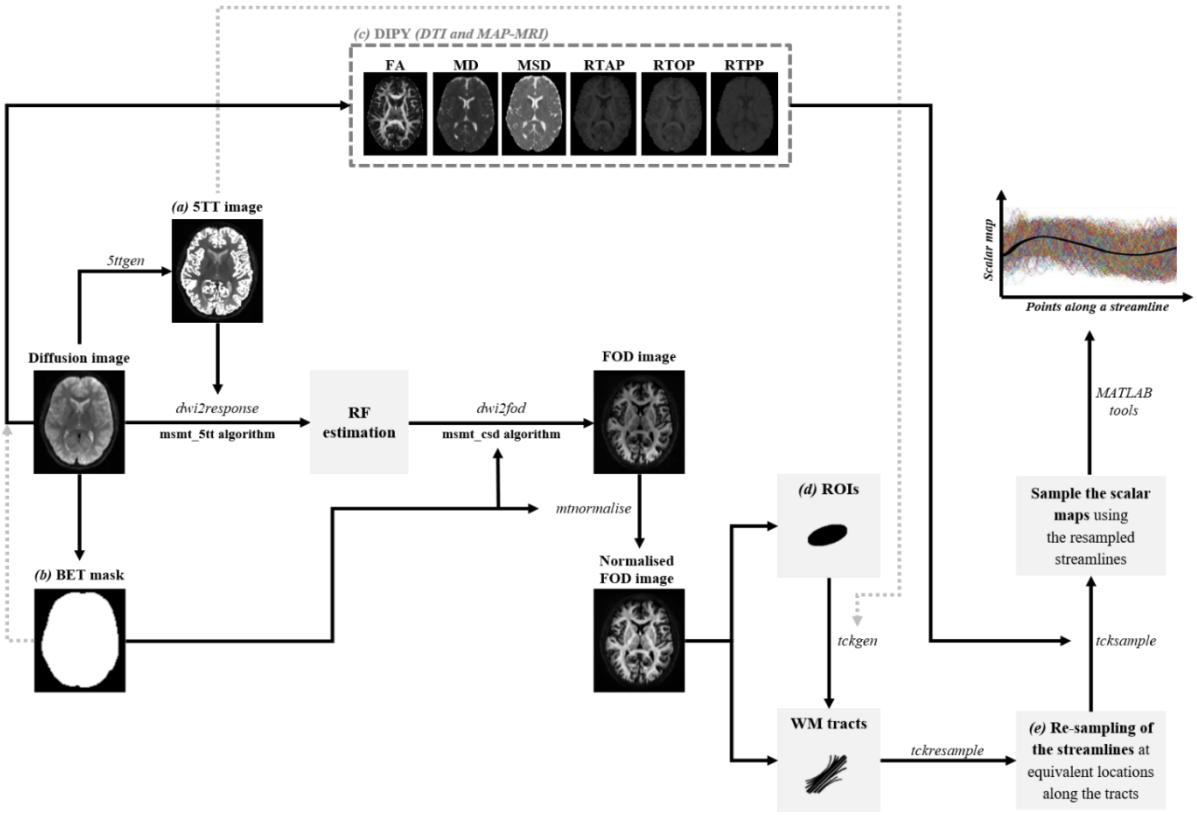

Figure 1 *- Pipeline of the along-tract analysis. From the diffusion images were generated: (a) five-tissue-type (5TT) segmented tissue images which were used as inputs on the estimation of the response-functions (RFs); (b) BET (Brain Extraction Tool) masks used to compute the fibre orientation distributions (FOD) images and their normalised images; and, (c) microstructural scalar maps using DIPY as framework. (d) The inclusion regions-of-interest (ROIs) were drawn to compute the tracts, using the 5TT image to delineate the propagation and termination of streamlines. (e) Using MRtrix, every streamline from each tract was resampled to a fixed number of points which were distributed equidistantly, in order to ensure that each streamline had the same number of points, and used to sample the scalar maps. Using MATLAB tools the microstructural averaged values were plotted along the tracts.*

RESULTS

Along-tract analysis of multiple microstructural metrics showed differences with statistical relevance between the groups (***Figure 2***). The results suggest a more detailed tissue characterization based on MAP-MRI parameters, reflecting the greater neuroanatomical specificity of these microstructural features along the tracts. We show that AF is microstructurally abnormal bilaterally despite the unilateral TLE diagnosed in these patients. Additionally, RTAP and RTOP showed an increased difference within CC between the groups compared to the along-tract behaviour drawn by FA, which highlights the biologically specificity of these markers in pathologies characterized by neuronal reduction as TLE.

CONCLUSION

Increased diffusivity and reduced anisotropy were observed, suggesting a loss of structural organization and expansion of the extracellular space, both locally and in extratemporal tracts, despite the left epileptic focus, which agrees with the concept that epilepsy is a network disorder. MAP-MRI parameters also show significant microstructural brain tissue changes, being a useful adjunct to conventional DTI parameters.

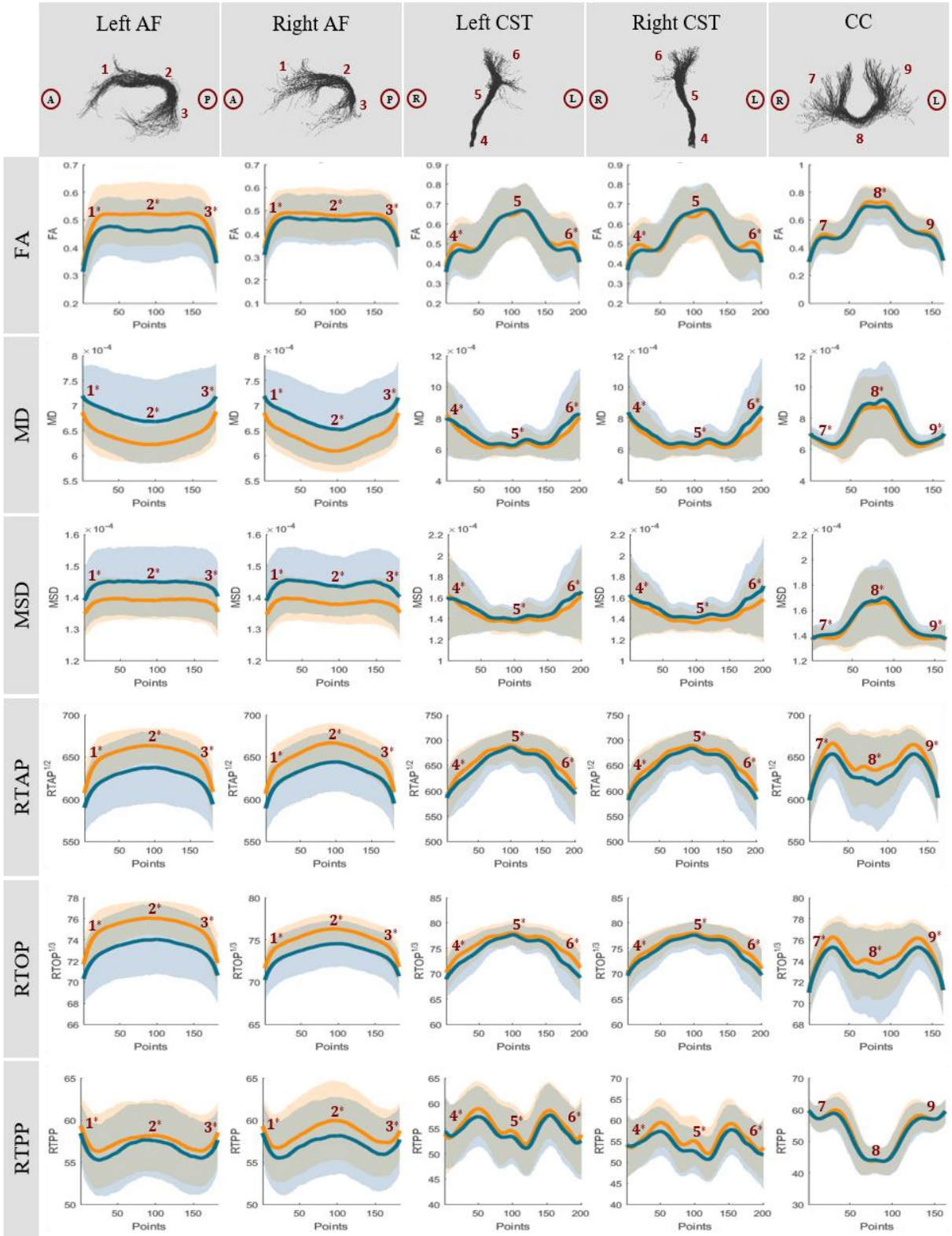

Figure 2 - *Along-tract analysis of the fractional anisotropy (FA), mean diffusivity (MD), mean square displacement (MSD), square-root of return-to-the-axis probability (RTAP), cube-root of return-to-the-origin probability (RTOP), and return-to-the plane probability (RTPP) along (from left to right) the left / right arcuate fasciculus (AF), where* ***(1)*** *represents the Broca's area,* ***(2)*** *the Geschwind's area and* ***(3)*** *the Wernicke's area; the left / right corticospinal tract (CST), where* ***(4)*** *represents the region near the brainstem,* ***(5)*** *the region at the level of the internal capsule and* ***(6)*** *the region near the motor cortex; and the corpus callosum (CC) - homologous connection between motor cortices, where* ***(7)*** *represents the connections to right motor cortex,* ***(8)*** *the colossal fibres near the mid-sagittal plane and* ***(9)*** *the connections to left motor cortex. The level of significance is represented by one star (*) where the p-value is lower than 0.01 (i.e. difference between groups with statistical relevance). The average variation of each microstructural parameter across the TLE patients is represented by the blue line and the associated standard deviation coloured by light-blue; and, the average variation of each microstructural parameter across the healthy controls is represented by the orange line and the associated standard deviation coloured by light-orange. The units of MD and MSD are* mm^2/s*, and RTAP, RTOP and RTPP are given by* mm^{-1}*. Abbreviations: A – anterior; P – posterior; L – left; R – right.*

Joana Guido, Luis Lacerda, Alexandre Andrade, Hugo Ferreira, Chris Clark. "Integration of multi-shell diffusion imaging derived metrics in tractography reconstructions", submitted for the Organization for Human Brain Mapping (OHBM) 2019 Annual Meeting (Rome, Italy).

Integration of multi-shell diffusion imaging derived metrics in tractography reconstructions

Joana Guido[1,2], Luis Lacerda[2], Alexandre Andrade[1], Hugo Ferreira[1], Chris Clark[2]

[1] Institute of Biomedical Engineering and Biophysics (IBEB), Faculty of Sciences, University of Lisbon, Portugal; [2] Developmental Imaging and Biophysics Section, UCL Great Ormond Street Institute of Child Health, London, United Kingdom

INTRODUCTION

Traditional tractography studies rely on averaging diffusion metrics along reconstructed pathways to identify microstructural changes between groups. Here, we developed a workflow to conduct along-tract analysis of white matter (WM) tracts and integrate not only *Diffusion Tensor Imaging* (DTI)[1] derived measures, but also more advanced parameters from *Mean Apparent Propagator-Magnetic Resonance Imaging* (MAP-MRI)[2,3], to investigate differences between controls and patients with Temporal Lobe Epilepsy (TLE) taking into account the potentially rich anatomical variation in diffusion metrics along the WM tracts.

METHODS

Data acquisition and pre-processing: 9 Patients with left TLE (5 males, mean age 12 years, age range 5–19 years) and 9 controls (5 males, mean age 12 years, age range 8–18 years) were studied. Data were collected on a Siemens Prisma 3.0T clinical system using a multi-band diffusion weighted single-shot spin echo - echo planar imaging sequence, with an acceleration factor of 2. Two sets of 60 non-collinear directions, using a weighting factor of $1000 s/mm^2$ and $2200 s/mm^2$, were acquired along with 13 additional T_2-weighted (b=0) volumes. 66 axial slices of thickness $2.0 mm$ were imaged, using a FOV=$220\times220 mm^2$ and 110×110 voxel acquisition matrix, for a final image resolution of $2.0\times2.0\times2.0 mm^3$; TE=$60 ms$ and TR=$3050 ms$. Images were denoised using MRtrix (Veraart's method[4,5]), with TOPUP and EDDY being used to correct susceptibility distortions, motion and eddy current.

Data processing: Tractography of arcuate fasciculus (AF), corticospinal tract (CST) and corpus callosum (CC) – homologous connection between motor cortices, and along-tract analysis, with integration of diffusion metrics computed using DIPY[6], were performed (complete pipeline in ***Figure 1***). A Kruskal-Wallis test was also executed in order to verify that the groups are statistically different, taking into account three sections (start, middle, end) of each tract with equivalent number of resampled points. A 1% significance value was considered.

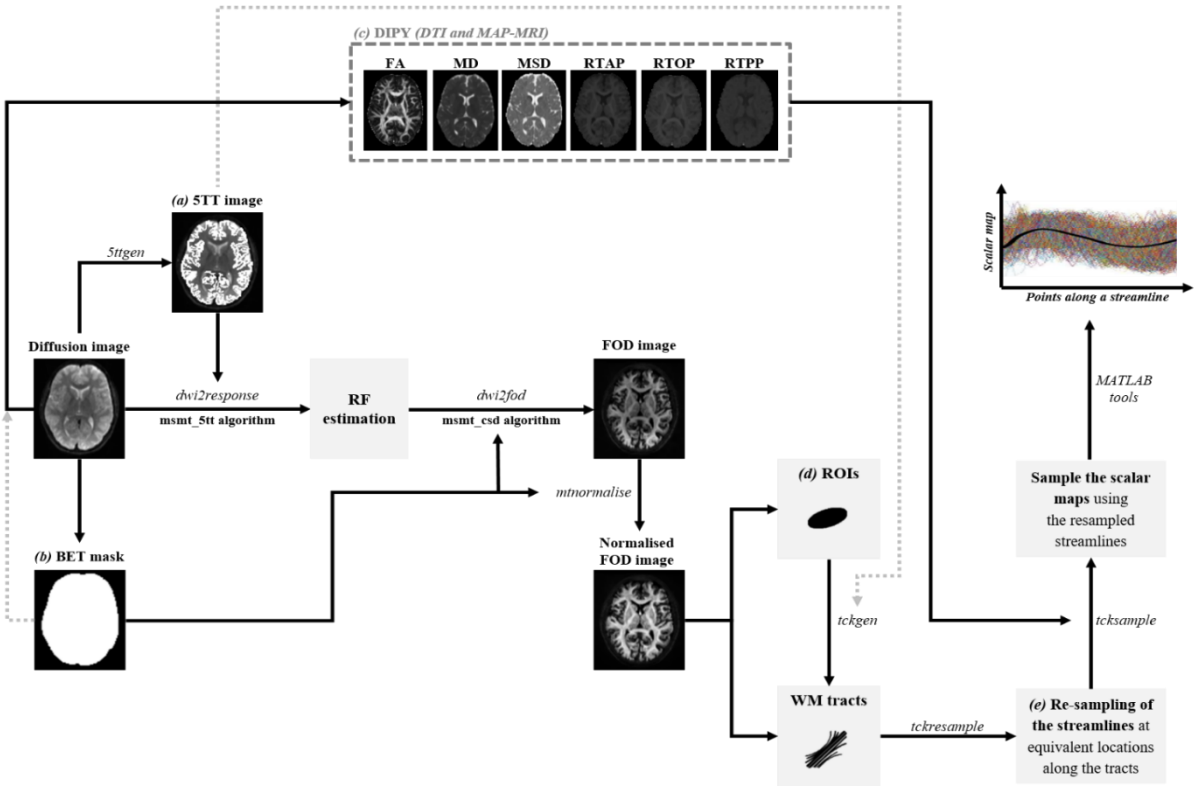

Figure 1 *- Pipeline of the along-tract analysis. From the diffusion images were generated: (a) five-tissue-type (5TT) segmented tissue images which were used as inputs on the estimation of the response-functions (RFs); (b) BET (Brain Extraction Tool) masks used to compute the fibre orientation distributions (FOD) images and their normalised images; and, (c) microstructural scalar maps using DIPY as framework. (d) The inclusion regions-of-interest (ROIs) were drawn to compute the tracts, using the 5TT image to delineate the propagation and termination of streamlines. (e) Using MRtrix, every streamline from each tract was resampled to a fixed number of points which were distributed equidistantly, in order to ensure that each streamline had the same number of points, and used to sample the scalar maps. Using MATLAB tools the microstructural averaged values were plotted along the tracts.*

RESULTS

Along-tract analysis of multiple microstructural metrics showed differences with statistical relevance between the two groups (***Figure 2***). The results suggest lower FA (fractional anisotropy) at AF in TLE patients. Regarding the CST, lower FA was detected in the brainstem and close to the motor cortex, with a brief decrease being also verified near the mid-sagittal plane of the CC. Higher MD (mean diffusivity) was observed within all tracts in TLE patients, which were also characterized by higher MSD (mean squared displacement). RTAP (return to axis probability) and RTOP (return to origin probability) were lower along the tracts of TLE patients. Despite RTPP (return to plane probability) assume lower values along the AF and CST of TLE patients, a smaller variation was displayed across the CC between the two groups, with no statistically significance being observed. Nevertheless, a more detailed tissue characterization based on MAP-MRI parameters was obtained, reflecting the physically meaningfulness of these microstructural features with greater neuroanatomical specificity along the tracts. For example, we show that the AF is microstructurally abnormal bilaterally despite the unilateral TLE diagnosed in these patients. And, RTAP and RTOP showed an increased difference within the CC between the two groups compared to the along-tract behaviour drawn by the FA profile, which highlights the biologically specificity of these tissue markers in pathologies characterized by neuronal reduction as TLE.

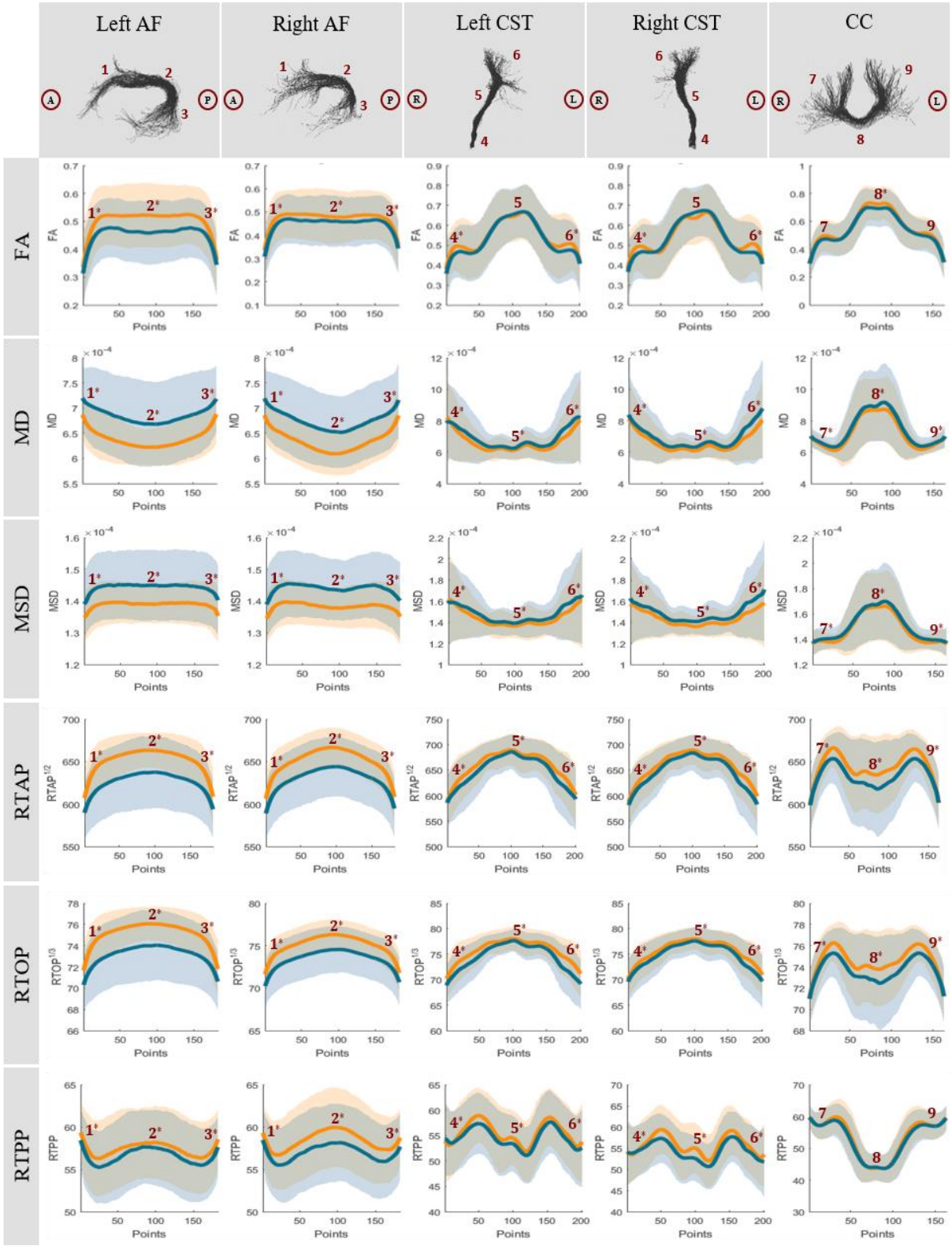

Figure 2 *- Along-tract analysis of the fractional anisotropy (FA), mean diffusivity (MD), mean square displacement (MSD), (square-root of) return-to-the-axis probability (RTAP), (cube-root of) return-to-the-origin probability (RTOP), and return-to-the plane probability (RTPP) along (from left to right) the left / right arcuate fasciculus (AF), where* ***(1)*** *represents the Broca's area,* ***(2)*** *the Geschwind's area and* ***(3)*** *the Wernicke's area; the left / right corticospinal tract (CST), where* ***(4)*** *represents the region near the brainstem,* ***(5)*** *the region at the level of the internal capsule and* ***(6)*** *the region near the motor cortex; and the corpus callosum (CC) - homologous connection between motor cortices, where* ***(7)*** *represents the connections to right motor cortex,* ***(8)*** *the colossal fibres near the mid-sagittal plane and* ***(9)*** *the connections to left motor cortex. The level of significance is represented by one star (*) where the p-value is lower than 0.01 (i.e. difference between groups with statistical relevance). The average variation of each microstructural parameter across the TLE patients is represented by the blue line and the associated standard deviation coloured by light-blue; and, the average variation of each microstructural parameter across the healthy controls is represented by the orange line and the associated standard deviation coloured by light-orange. The units of MD and MSD are* mm^2/s*, and RTAP, RTOP and RTPP are given by* mm^{-1}*. Abbreviations: A – anterior; P – posterior; L – left; R – right.*

CONCLUSION

The results showed increased diffusivity and reduced anisotropy, suggesting a loss of structural organization and expansion of the extracellular space with TLE, both locally and in extratemporal tracts despite the left epileptic focus, which agrees with the concept that epilepsy is a network disorder. In addition MAP-MRI parameters also show significant microstructural brain tissue changes and are a useful adjunct to conventional DTI parameters.

REFERENCES

1. Basser PJ, Mattiello J, LeBihan D (1994). *MR diffusion tensor spectroscopy and imaging*. Biophysical journal, 66(1): 259-267.
2. Özarslan E, Koay CG, Shepherd TM, *et al.* (2013). *Mean apparent propagator (MAP) MRI: A novel diffusion imaging method for mapping tissue microstructure*. NeuroImage, 78: 16-32.
3. Avram AV, Sarlls JE, Barnett AS, *et al.* (2016). *Clinical feasibility of using mean apparent propagator (MAP) MRI to characterize brain tissue microstructure.* NeuroImage, 127: 422-434.
4. Veraart J, Fieremans E, Novikov DS (2016). *Diffusion MRI noise mapping using random matrix theory*. Magnetic resonance in medicine, 76(5): 1582-1593.
5. Veraart J, Novikov DS, Christiaens D, Ades-Aron B, Sijbers J, Fieremans E (2016). *Denoising of diffusion MRI using random matrix theory.* NeuroImage, 142: 394-406.
6. Garyfallidis E, Brett M, Amirbekian B, *et al.* (2014). *Dipy, a library for the analysis of diffusion MRI data.* Frontiers in neuroinformatics, 8(8).